Dynamics of the Intertropical Convergence Zone

Thesis by
Tobias Bischoff

In Partial Fulfillment of the Requirements for the
Degree of
Doctor of Philosophy

CALIFORNIA INSTITUTE OF TECHNOLOGY
Pasadena, California

2017
Defended June 9, 2016

Tobias Bischoff
ORCID: 0000-0003-3930-2762

To my parents

"For the greatest enemy of truth is very often not the lie – deliberate, contrived and dishonest – but the myth – persistent, persuasive, and unrealistic. Too often we hold fast to the clichés of our forebears. We subject all facts to a prefabricated set of interpretations. We enjoy the comfort of opinion without the discomfort of thought."

John F. Kennedy
Commencement Address at Yale University, June 11, 1962

ACKNOWLEDGEMENTS

This thesis would not have been possible without a long list of friends, my colleagues and mentors, and my family.

I thank my brother, Felix Bischoff, and my parents, Matthias and Manuela Bischoff, for their constant support throughout these years.

I thank my adviser and mentor, Tapio Schneider, for his guidance, continuing support, his humanity and friendship. I also thank my thesis committee members, Andrew Thompson, Simona Bordoni, and Jess Adkins, for stimulating discussions and their help, especially when the times were the toughest. A special thanks goes to Bruno Eckhardt and Horst Fischer who ultimately led me to Caltech.

I thank my colleagues and friends, Xavier Levine, Farid Ait Chaalal, Andrew and Usha Stewart, Momme Hell, Ori Adam, Anne Laraia, and Adam Subhas, for good conversations, amazing parties, road trips, and adventures. I thank all my other friends, first and foremost my roommates, Bryan Riel and Chris Rollins (you are the best), Miki Nakajima (arigatou gozaimashita) for her strong support over the past years, Felix and Michaela Schmidt for hosting me every time I was in Germany, Benedikt Hamich and Deborah Gruner for crazy nights in Berlin, and Sara Teixeira for Ferrero Rocher and for exploring Dresden with me.

I also thank the people who started this program with me, Becky Schwantes, Alex Teng, Hank Yu, Jinqiang Chen, Hao Zhang, and Robert Wills. I am indebted to each and every one of you for your patience, support, and friendship. You made me a more complete scientist. Caltech has been an amazing place for me to learn and explore. I had the privilege to meet many incredibly gifted people and I will be forever grateful for this.

In the context of this thesis, I thank Gerald Haug, Nele Meckler, Andrew Stewart, Simona Bordoni, Robb Wills, and Ori Adam for stimulating discussions on drafts of the chapters of this thesis. The work presented here was supported by NSF Grants AGS-1019211, AGS-1049201, AGS-1003614, and OCE-1235488. The idealized GCM simulations were performed on Caltech's Division of Geological and Planetary Science CITerra computing cluster and on ETH Zurich's EULER computing clusters. I acknowledge the World Climate Research Programme's Working Group on Coupled Modelling, which is responsible for CMIP, and I thank the climate modeling groups for producing and making available their model output. I also thank John Fasullo

and Kevin Trenberth from the National Center for Atmospheric Research for providing the energy flux data (retrieved from https://climatedataguide.ucar.edu/climate-data/era-interim-derived-components) I used in some of the estimates in the text.

ABSTRACT

Previous studies have shown that the latitude of the Intertropical Convergence Zone (ITCZ) is negatively correlated with cross-equatorial atmospheric energy transport and that the ITCZ shifts southward as the northern hemisphere cools and the northward cross-equatorial energy transport strengthens. However, it has remained unclear what controls the sensitivity of the ITCZ position to cross-equatorial energy transport, and what other factors may lead to shifts of the ITCZ position. In this thesis, it is shown how an energetic perspective using the vertically-integrated moist static energy balance of the atmosphere can be used to address this question. Climate states with a double-ITCZ around the equator also occur, for example, seasonally over the eastern Pacific, and frequently in climate models. Here it is shown how the ITCZ position is connected to the energy balance near the equator under a wide range of circumstances, including states with single and double ITCZs and using a Taylor expansion of the meridional energy transport around the equator quantitative estimates for the ITCZ location are derived. Simulations with an idealized aquaplanet general circulation model (GCM) confirm the quantitative adequacy of these relations. Using these ideas, an idealized precipitation model for the tropics is presented that is able to capture variations of paleoclimatological precipitation records on orbital time scales. The results provide a framework for assessing and understanding causes of common climate model biases and for interpreting tropical precipitation changes, such as those evident in records of climates of the past.

PUBLISHED CONTENT AND CONTRIBUTIONS

1. Bischoff, T. & Schneider, T. Energetic constraints on the position of the intertropical convergence zone. *J. Climate* **27.** doi:10.1175/JCLI-D-13-00650.1 (2014).
   Both authors conceived the study and wrote the paper, Tobias designed the simulations and performed the data analysis.

2. Bischoff, T. & Thompson, A. F. Configuration of a Southern Ocean storm track. *J. Phys. Oceangr.* **44.** doi:10.1175/JPO-D-14-0062.1 (2014).
   Both authors conceived the study and wrote the paper, Tobias designed the simulations and performed the data analysis.

3. Bischoff, T. & Schneider, T. The equatorial energy balance, ITCZ position, and double ITCZ bifurcations. *J. Climate* **29.** doi:10.1175/JCLI-D-15-0328.1 (2016).
   Both authors conceived the study and wrote the paper. Tobias designed the simulations and performed the data analysis.

TABLE OF CONTENTS

LIST OF ILLUSTRATIONS

Number *Page*

LIST OF TABLES

Chapter 1

INTRODUCTION

1.1 Overview of the ITCZ

The tropical climate on Earth is dominated by wet and dry seasons caused by the seasonal migrations of the tropical rain belt, usually referred to as the Intertropical Convergence Zone (ITCZ), located on average near the center of Earth's Hadley cells at about 6° N [e.g, 1]. The ITCZ coincides with the regions of strongest rainfall on the planet because converging low-level winds bring water vapor from all tropical latitudes that drive moisture flux convergence at the ITCZ. Rising saturated air through convection then fuels condensation that ultimately makes it to the surface as rain.

Seasonally, the ITCZ, and with it the location of maximum rainfall, migrates from the southern hemisphere into the northern hemisphere and back, thereby inducing dry and wet seasons in many tropical regions in South and Central America, Africa, India, or Indonesia. Consequently, understanding the dynamics of the ITCZ and how it behaves under different climatic boundary conditions is of importance for climate predictions, the related policy decisions, and for the interpretation of past climate records from the tropics. For example, any shift in the average location of the ITCZ is accompanied by a drastic reduction in rainfall in some regions and a strong increase in others, potentially resulting in drought or flooding conditions.

Developing a theory of ITCZ dynamics can be divided into two parts, one that deals with the location of the ITCZ, and another one that deals with how much rain actually falls where the ITCZ is located at any given time. In this thesis, we are mostly concerned with the former. Despite the importance of understanding the dynamics of the ITCZ, few quantitative theories of its location have been developed. At the same time, the response of the ITCZ location to increased greenhouse gases in comprehensive climate models is not consistent across models in either direction or magnitude [e.g., 2]. What is understood, is that there is a general tendency for the ITCZ to shift towards the differentially warmed hemisphere under a wide range of climate changes [e.g., 2–8]. Any theory for the location of the ITCZ then, under certain assumptions, must make predictions as to why the ITCZ shifts under different climate scenarios, and at least provide a reasonable estimate for

the magnitude of any potential shift. It must also explain other features of the ITCZ, for example the fact that in springtime two ITCZs appear in the eastern equatorial Pacific. This phenomenon is commonly referred to as a double-ITCZ, meaning that two strong maxima in tropical rainfall occur, one to each side of the equator. Besides the theoretical importance of understanding this phenomenon, comprehensive climate models of all kinds are currently unable to correctly simulate the strength and location of the Pacific double-ITCZ. In the literature this is referred to as the double-ITCZ bias [e.g., 9, 10].

Understanding the dynamics of the ITCZ is also of importance for the interpretation of tropical paleoclimatological precipitation records. This is because both, shifts in the ITCZ location and changes in the overall precipitation amount, contribute to the rainfall signal measured in these records. Such records include anything that could potentially measure the amount of rainfall, i.e., sediment core records, stalagmites, or lake level records [e.g. 11–18]. Without a dynamically consistent theory of what sets the two factors, location of ITCZ and amount of rainfall, interpreting records will remain challenging, especially because simulations from comprehensive climate models for past climates are only available on suborbital or shorter time scales.

1.2 Theoretical approaches

In this thesis, we will adopt a zonal-mean perspective but many ideas carry over to the zonally-varying perspective as well [19]. How to develop a theory for the zonal-mean location of the ITCZ, or approximations to this quantity, is currently not fully understood due to the complex interplay between the angular momentum balance and the energy balance of the tropical atmosphere. From an angular momentum and mass flux balance perspective, the ITCZ is approximately located where the first meridional derivative of the mean low-level streamfunction is maximal. Thus, mathematically speaking, an estimate for the ITCZ location can be derived by solving the following equation:

$$\partial_{yy}\Psi(y_{\mathrm{ITCZ}}, p_{\mathrm{low}}) = 0, \tag{1.1}$$

where $y = a\phi$ is the meridional distance from the equator, Ψ is the mean meridional streamfunction, y_{ITCZ} is the zonal-mean ITCZ location, and p_{low} is a low-level pressure level. The problem with equation (1.1) lies in the fact that having a closed-form solution or even an analytic approximation appears to be difficult if not impossible.

In order to make progress, we will sacrifice some accuracy in our approximations

and trade it for the ability to derive analytic estimates for the zonal-mean ITCZ location that can be investigated mathematically. Therefore, instead of working with (1.1) we choose to introduce the approximation that the location where the first meridional derivative of the low-level streamfunction is maximal, is approximately co-located with the vertical zero contour of the mean meridional streamfunction. Using further approximations outlined in Chapers 2 and 3, one can then show that the ITCZ location is approximately determined by the relationship

$$F(y_{\mathrm{ITCZ}}) = 0, \tag{1.2}$$

where F is the zonally-averaged and vertically-integrated moist static energy transport of the atmosphere. We show that the notion of equation (1.2) is consistent with previous work [e.g., 2, 5, 6, 8, 20] and that it provides a consistent mathematical framework in which ITCZ shifts can be understood. We also provide insights into how this approach can be generalized to understand the double-ITCZ and associated biases.

1.3 Thesis outline

In order to develop a theory for the location of the ITCZ, we use the energetic approach outlined above. Using this theory, we build a conceptual precipitation model that uses top-of-atmosphere insolation as input only to understand tropical paleoclimatological precipitation records. Chapter 2 of this thesis introduces the concepts used in the energetic framework and demonstrates its usefulness in understanding a wide range of ITCZ shifts in the zonal mean using an idealized general circulation model under tropical and global warming scenarios. We also provide insights into how the simple energetic argument from equation (1.2) can be extended using closure approximations for midlatitude macrotubulent transport processes to relate the location of the ITCZ to near-surface temperatures. In Chapter 3, we extend the ideas from Chapter 2 to the case of double-ITCZs and show under what circumstances they can arise, using the same idealized model as in Chapter 2. In Chapter 4 we use the insights from Chapters 2 and 3 to construct a conceptual precipitation model that can be analyzed analytically. One major difference compared to Chapters 2 and 3 is that in order to build a complete precipitation model, we also introduce a parameterization for rainfall amount in the tropics. Chapter 5 is unrelated to the main topic of this thesis and deals with oceanic storm tracks. Chapter 6 contains the overall conclusions and open questions from this line of research.

Chapter 2

ENERGETIC CONSTRAINTS ON THE POSITION OF THE INTERTROPICAL CONVERGENCE ZONE

1. Bischoff, T. & Schneider, T. Energetic constraints on the position of the intertropical convergence zone. *J. Climate* **27.** doi:10.1175/JCLI-D-13-00650.1 (2014).

2.1 Abstract

The Intertropical Convergence Zone (ITCZ) can shift meridionally on seasonal and longer timescales. Previous studies have shown that the latitude of the ITCZ is negatively correlated with cross-equatorial atmospheric energy transport. For example, the ITCZ shifts southward as the northern hemisphere cools and the northward cross-equatorial energy transport strengthens in response. But it has remained unclear what controls the sensitivity of the ITCZ position to cross-equatorial energy transport, and what other factors may lead to shifts of the ITCZ position. Here it is shown that the sensitivity of the ITCZ position to cross-equatorial energy transport depends on the net energy input to the equatorial atmosphere: the net radiative energy input minus any energy uptake by the oceans. Changes in this energy input can also lead to ITCZ shifts. The cross-equatorial energy transport is related through a series of approximations to interhemispheric asymmetries in the near-surface temperature distribution. The resulting theory of the ITCZ position is tested in idealized general circulation model simulations with a slab ocean as lower boundary condition. In the simulations, cross-equatorial energy transport increases under global warming (primarily because extratropical latent energy fluxes strengthen), and this shifts the ITCZ poleward. The ITCZ shifts equatorward if primarily the tropics warm in response to an increased net energy input to the equatorial atmosphere. The results have implications for explaining the varied response of the ITCZ to global or primarily tropical changes in the atmospheric energy balance, such as occur under global warming or El Niño.

2.2 Introduction

The ITCZ is a band of deep convective clouds in the tropics that marks the region of maximum precipitation on Earth. It is located around 6°N latitude in the annual

and zonal mean but migrates seasonally between a more northern position in boreal summer and a more southern position in austral summer [21–23]. Additionally, the annual-mean position of the ITCZ has shifted on geological timescales [e.g., 24, 25], mimicking its seasonal migration insofar as it tends to shift toward a differentially warming and away from a differentially cooling hemisphere [e.g., 7, 26]. Modeling studies with general circulation models (GCMs) have demonstrated that remote extratropical factors, such as the presence or absence of polar ice cover or high-latitude temperature variations caused by the Atlantic meridional overturning circulation, can lead to shifts of the ITCZ, generally away from a cooling and toward a warming hemisphere [e.g., 3, 4, 27–29].

Recent studies have focused on the role of the cross-equatorial energy transport and the atmospheric energy budget in controlling the ITCZ position. They have demonstrated that the ITCZ tends to shift southward as the northward atmospheric energy transport across the equator strengthens, for example, in response to a northern high-latitude cooling [e.g., 2, 5, 6, 8, 20]. As the atmospheric energy transport generally strengthens in the direction of a cooling hemisphere, to partially compensate the cooling, the recent studies focusing on the atmospheric energy transport are broadly consistent with studies that emphasize surface temperature changes [e.g., 3, 28, 30]

However, the ITCZ also shifts southward during El Niño [e.g., 23, 31]—an observation not easily related to changes in cross-equatorial energy transport. A quantitative understanding of the factors controlling the ITCZ position, including the sensitivity of the ITCZ to changes in cross-equatorial energy transport, has remained elusive. That other factors than those hitherto considered must influence the ITCZ position is evident already for dimensional reasons: For example, it is empirically clear that the ITCZ position, which has units of length (e.g., displacement from the equator), is sensitive to the cross-equatorial atmospheric energy transport, which has units of power when integrated over latitude circles. To relate these two physical quantities, another quantity with units of power per unit length must enter any relation between ITCZ position and cross-equatorial energy transport.

Here we derive a quantitative relation between the cross-equatorial energy transport and the position of the ITCZ from the atmospheric energy balance. We show that the net energy input to the equatorial atmosphere is the natural quantity of units power per unit length to relate the ITCZ position to the cross-equatorial energy transport. We use an idealized GCM to demonstrate that the theoretically derived relation accurately captures the factors controlling the ITCZ position under both global and

primarily tropical warming. The global and primarily tropical warming represent in an idealized manner aspects of what occurs under global warming associated with increased greenhouse gas concentrations, and under more local tropical warming associated with changes in the tropical energy budget, such as occur during El Niño. We find that the ITCZ generally shifts away from the equator under global warming and toward the equator under primarily tropical warming.

However, other factors not taken into account in our simulations, such as differential changes in aerosol loading between the hemispheres [e.g., 32, 33], likely would modulate the results we obtain in an idealized setting.

2.3 Theory

Atmospheric energy balance and energy transport

Neglecting the relatively small kinetic energy of atmospheric motions and energy storage in the atmosphere and on land surfaces, the zonal-mean energy balance integrated over atmospheric columns is [34]

$$\mathcal{S} - \mathcal{L} - \mathcal{O} = \partial_y \langle \overline{v\, h} \rangle. \tag{2.1}$$

The left-hand side represents the net energy input to the atmosphere: the net incoming shortwave radiation $\mathcal{S}$ minus the outgoing longwave radiation $\mathcal{L}$ and any net energy uptake $\mathcal{O}$ by the oceans (or more generally the surface), associated with uptake/release of stored energy and/or ocean energy flux divergence. The right-hand side represents the divergence of the meridional flux (meridional velocity v) of moist static energy h in the atmosphere.[1] To simplify notation, we have adopted local Cartesian coordinates for small displacements $y = a\phi$ from the equator (Earth's radius a and latitude ϕ), suppressing $\cos(\phi)$ factors in the divergence; however, we perform all actual calculations in spherical coordinates. Angle brackets $\langle \cdot \rangle$ represent a mass-weighted integral over an atmospheric column, and overbars denote a time and zonal mean. Eq. (2.1) states that any net energy input into the atmosphere must be balanced by a dynamic atmospheric energy transport from latitudes of net energy input (tropics) to latitudes of net energy deficit (extratropics).

At the ITCZ, low-level winds converge and upper-level winds diverge. To the extent that the latitude at which the mean meridional winds change sign does not vary strongly with altitude, and that eddy fluxes across this latitude are negligible, the

[1] The moist static energy $h = s + l$ is defined as the sum of dry static energy $s = c_p T + gz$ and latent energy $l = L_v q$, where L_v is the latent heat of vaporization, q is the specific humidity, and other symbols have their usual meanings.

zonal-mean ITCZ is located close to the latitude δ at which the atmospheric energy flux $\langle\overline{v\,h}\rangle_\delta$ changes sign [e.g., 5, 6]. The location of the zonal mean precipitation maximum and the location where the atmospheric energy flux changes sign may not exactly coincide, and their separation may change with climate or seasons [2]. But we assume that the responses in both quantities are correlated at least as long as the ITCZ remains close to the equator, and we focus on inferring the latitude where the atmospheric energy flux changes sign given the cross-equatorial energy transport and the net energy input to the tropical atmosphere. Expanding the atmospheric energy flux at a low latitude δ around the cross-equatorial flux, we obtain to first order in δ,

$$0 \approx \langle\overline{v\,h}\rangle_\delta = \langle\overline{v\,h}\rangle_0 + a\partial_y\langle\overline{v\,h}\rangle_0\,\delta, \tag{2.2}$$

where the subscript 0 denotes quantities evaluated at the equator. Solving for δ and substituting for the atmospheric energy flux divergence (2.1) at the equator gives the ITCZ position

$$\delta \approx -\frac{1}{a}\,\frac{\langle\overline{v\,h}\rangle_0}{\mathcal{S}_0 - \mathcal{L}_0 - \mathcal{O}_0}. \tag{2.3}$$

This shows that the ITCZ position, to first order in δ, is proportional to the negative of the atmospheric energy flux across the equator, $\langle\overline{v\,h}\rangle_0$, with the sensitivity of this dependence (the proportionality 'constant', which need not be constant) determined by the net energy input to the equatorial atmosphere, $\mathcal{S}_0 - \mathcal{L}_0 - \mathcal{O}_0$.[2] For Earth's annual- and zonal-mean equatorial net energy input of about 10–20 $\mathrm{W\,m^{-2}}$ [35], it implies that the ITCZ shifts approximately 1°–2° southward for every 0.1 PW increase in northward cross-equatorial atmospheric energy transport, holding the net energy input fixed.

The relation (2.3) provides a first-order quantitative basis for understanding the anticorrelation between cross-equatorial energy transport and ITCZ position seen in GCM simulations [e.g., 2, 5, 6, 20]. Additionally, it explains how and by how much the ITCZ can shift in response to equatorial changes that may not have a signature in cross-equatorial energy transport: If the net energy input to the equatorial atmosphere in the denominator of Eq. (2.3) changes, the sensitivity of the ITCZ position to cross-equatorial energy transport changes, and that alone can shift the ITCZ (see Fig. 2.1 for an illustration). For example, the increased net energy input to the equatorial atmosphere during El Niño by itself (apart from any

[2] A slightly more accurate relation is obtained if the net energy input in the denominator is not evaluated at the equator but is averaged between the equator and the ITCZ; however, given the uncertainties in the inferred net energy input, this makes little difference in Earth's atmosphere.

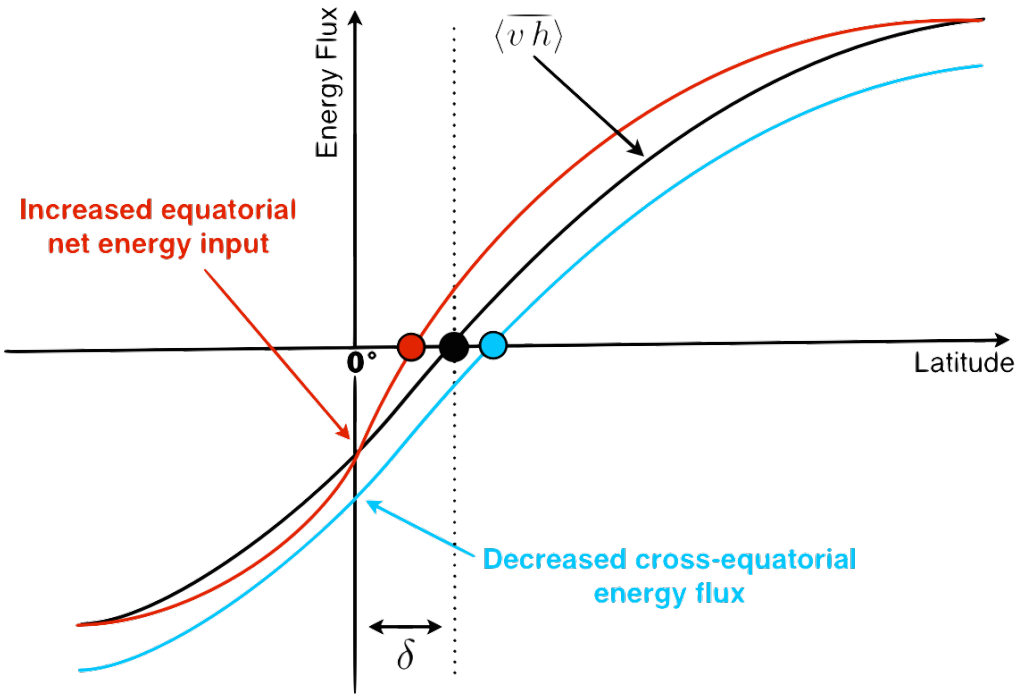

Figure 2.1: Qualitative behavior of the ITCZ position (large dots) as the northward cross-equatorial atmospheric energy flux $\langle \overline{v\,h} \rangle_0$ decreases (blue line) and as the net energy input to the equatorial atmosphere $\mathcal{S}_0 - \mathcal{L}_0 - \mathcal{O}_0 = \partial_y \langle \overline{v\,h} \rangle_0$ increases (red line). Decreased northward energy flux at the equator shifts the zero of the energy flux and hence the ITCZ poleward. Increased energy input increases the divergence (slope) of the energy flux and shifts its zero and hence the ITCZ equatorward.

change in cross-equatorial energy transport) implies an equatorward shift of the ITCZ according to relation (2.3), as is in fact observed [e.g., 23, 31]. Changes in the net energy input to the equatorial atmosphere may also explain why the ITCZ shifts as tropical cloud parameterizations are varied in GCMs [5, 6].

The linear approximation implicit in relation (2.3) gives the exact position of the zero of the atmospheric energy flux if the energy flux varies linearly with latitude in the vicinity of the equator (as illustrated in Fig. 2.1). Where this is inaccurate—that is, where the energy flux varies more strongly with latitude near the equator, as it does regionally—higher-order terms in the expansion, involving higher derivatives of the atmospheric energy flux near the equator, may be needed to improve the approximation. However, in the zonal and annual mean, Eq. (2.3) approximates the zero of the atmospheric energy flux to within $1^\circ - 2^\circ$ accuracy, according to the data provided by Fasullo & Trenberth [35].

To connect the cross-equatorial energy transport to interhemispheric asymmetries, we integrate the energy balance (2.1) separately from the equator to the latitudes ϕ_N and ϕ_S near the northern and southern edges of the Hadley circulation where the mean meridional energy flux $\langle \overline{v}\,\overline{h} \rangle$ vanishes, and the total flux $\langle \overline{vh} \rangle = \langle \overline{v}\,\overline{h} \rangle + \langle \overline{v'h'} \rangle$ approximately reduces to the eddy flux $\langle \overline{v'h'} \rangle$. In the present climate, this occurs near $\phi_{N,S} \approx \pm 35^\circ$. The two integrations yield two expressions that can be combined to give the cross-equatorial atmospheric energy flux in terms of interhemispheric asymmetries in eddy energy fluxes at ϕ_S and ϕ_N and in the net atmospheric energy input between ϕ_S and ϕ_N,

$$\langle \overline{v\,h} \rangle_0 \approx \left\{ \langle \overline{v'h'} \rangle \right\}_S^N - \left\{ \int_0^y (\mathcal{S} - \mathcal{L} - \mathcal{O})\, dy \right\}_S^N . \tag{2.4}$$

Here, the braces $\{\cdot\}_S^N$ denote the arithmetic mean of $(\cdot)$ evaluated at ϕ_N and ϕ_S. This relation is diagnostic in the sense that the location where the mean meridional energy flux vanishes is not a constant but may change with climate. For a hemispherically symmetric planet, the eddy energy flux and input integral on the right-hand side of Eq. (2.4) are hemispherically antisymmetric; their arithmetic means at ϕ_N and ϕ_S are zero, and so is the cross-equatorial atmospheric energy flux. Any nonzero cross-equatorial atmospheric energy flux arises from asymmetries in the eddy energy flux at $\phi_{N,S}$, and from asymmetries in the energy input to the atmosphere within the tropical latitude belt between ϕ_S and ϕ_N, for example, by asymmetries in ocean energy flux divergence. On Earth currently, the eddy flux $\langle \overline{v'h'} \rangle$ approximately exports 0.5 PW more at the southern edge of the tropics than at the northern, giving a hemispherically asymmetric contribution [first term on the right-hand side of Eq. (2.4)] of about −0.25 PW [36]. By contrast, the interhemispheric asymmetry in the net energy input to the tropical belt (second term) amounts to about 0.1 PW and so is comparatively small [35]. From this perspective, an annual- and zonal-mean ITCZ in the northern hemisphere arises primarily because eddies transport more energy poleward in the southern than in the northern extratropics [cf. 5, 6], at least in part because the oceanic meridional overturning circulation cools the southern and warms the northern high latitudes [36–38]. This leads to weaker pole-equator temperature gradients and weaker eddy energy fluxes in the northern hemisphere, and ultimately to a northward displaced ITCZ. However, these inferences are uncertain, because both oceanic and atmospheric energy fluxes and the net energy input to the atmosphere within the tropical belt are uncertain, with standard errors in meridional energy fluxes of at least ±0.2 PW [39, 40].

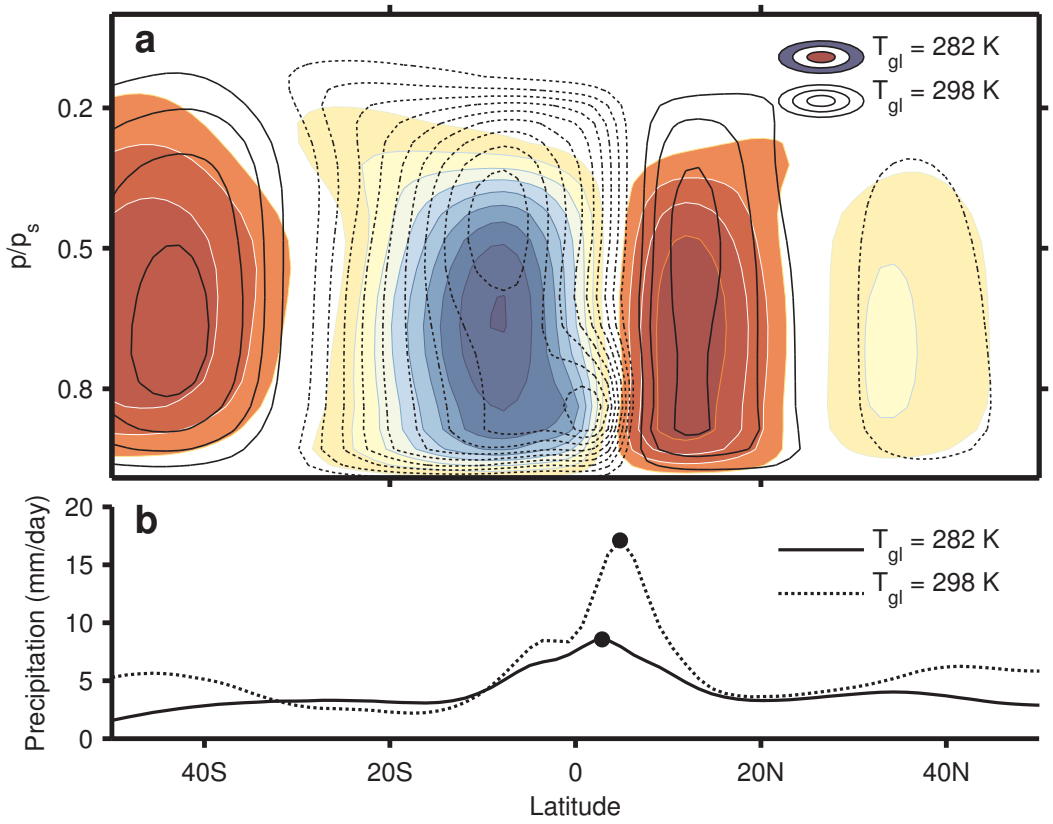

Figure 2.2: (a) Mass flux streamfunction and (b) precipitation for global-mean surface temperatures $T_{\rm gl} = 282$ K and $T_{\rm gl} = 298$ K in the global warming scenario. The contour interval in (a) is 1.6×10^{10} kg s^{-1}. Red/solid contours show northward mass transport, and blue/dashed contours show southward mass transport. The maximum and minimum values of the streamfunctions are 7.8×10^{10} kg s^{-1} and -14.5×10^{10} kg s^{-1} at $T_{\rm gl} = 282$ K, and 7.1×10^{10} kg s^{-1} and -15.8×10^{10} kg s^{-1} at $T_{\rm gl} = 298$ K. The black dots in (b) mark the precipitation maximum. The ITCZ generally is farther poleward in warmer climates, and the maximum precipitation is strengthened. In addition, the Hadley cells expand and the tropopause height increases. The zero of the mass flux streamfunction moves poleward with global-mean surface temperature but remains poleward of the precipitation maximum.

Before relating interhemispheric asymmetries in energy fluxes to those in surface temperatures through a series of closure approximations, we illustrate and test the energetic constraints on the ITCZ position with GCM simulations.

2.4 GCM simulations

We use an idealized moist GCM to be able to test the validity of the theoretical expressions (2.3) and (2.4) over a wider range of climates than those of Earth's

recent past and proximate future. This allows us to delineate the range of validity of the expressions more clearly than would be possible by analyzing observations or simulating climate changes with a comprehensive GCM. With the idealized GCM, we can investigate separately the effects of tropical energy input changes and cross-equatorial energy flux changes—effects that usually occur together during ENSO or global warming. Our GCM is that of O'Gorman & Schneider [41], which is similar to that used in Frierson *et al.* [42] and Frierson [43]. The GCM uses a two-stream radiation scheme without clouds or aerosols, and the lower boundary consists of a slab ocean. We explore two different energy budget perturbations, one global and one tropical: (i) We vary the longwave optical depth of the atmosphere globally, leading to global temperature changes, with global-mean surface temperatures spanning the large range from 275 to 315 K; (ii) we vary an imposed ocean energy flux convergence in a thin band around the equator, leading to primarily tropical temperature changes, with tropical surface temperatures spanning 303 to 308 K. (We have verified that this zonally symmetric surface heating has the same effect in the zonal mean as a zonally more localized surface heating with the same zonal mean, which would be more representative of El Niño.) For the atmospheric circulation to be hemispherically asymmetric, we also impose a hemispherically antisymmetric ocean energy uptake/release O outside 30°N/S, which cools the southern and warms the northern hemisphere, in a similar way as in Kang *et al.* [5, 6]. This may represent, for example, energy transport associated with an oceanic meridional overturning circulation, or interhemispheric differences in surface albedo such as those due to differences in ice cover. The resulting poleward atmospheric energy fluxes are stronger in the southern than in the northern hemisphere and lead to an ITCZ north of the equator, as on Earth. Details of the simulations are given in Appendix A.

Global warming

The contours in Fig. 2.2a show typical mass flux streamfunctions for a cold and a warm case in the global warming scenario. In the warmer climate, the region of maximum low-level upward mass flux and the zero contour of the mass flux streamfunction are located farther away from the equator. This accompanies an increase in tropopause height and Hadley circulation width [cf. 44–46]. At the same time, the precipitation maximum (Fig. 2.2b) lies farther away from the equator in the warmer climate, as does the colocated maximum of the low-level upward mass flux. The precipitation maximum is also strengthened in the warmer climate, primarily

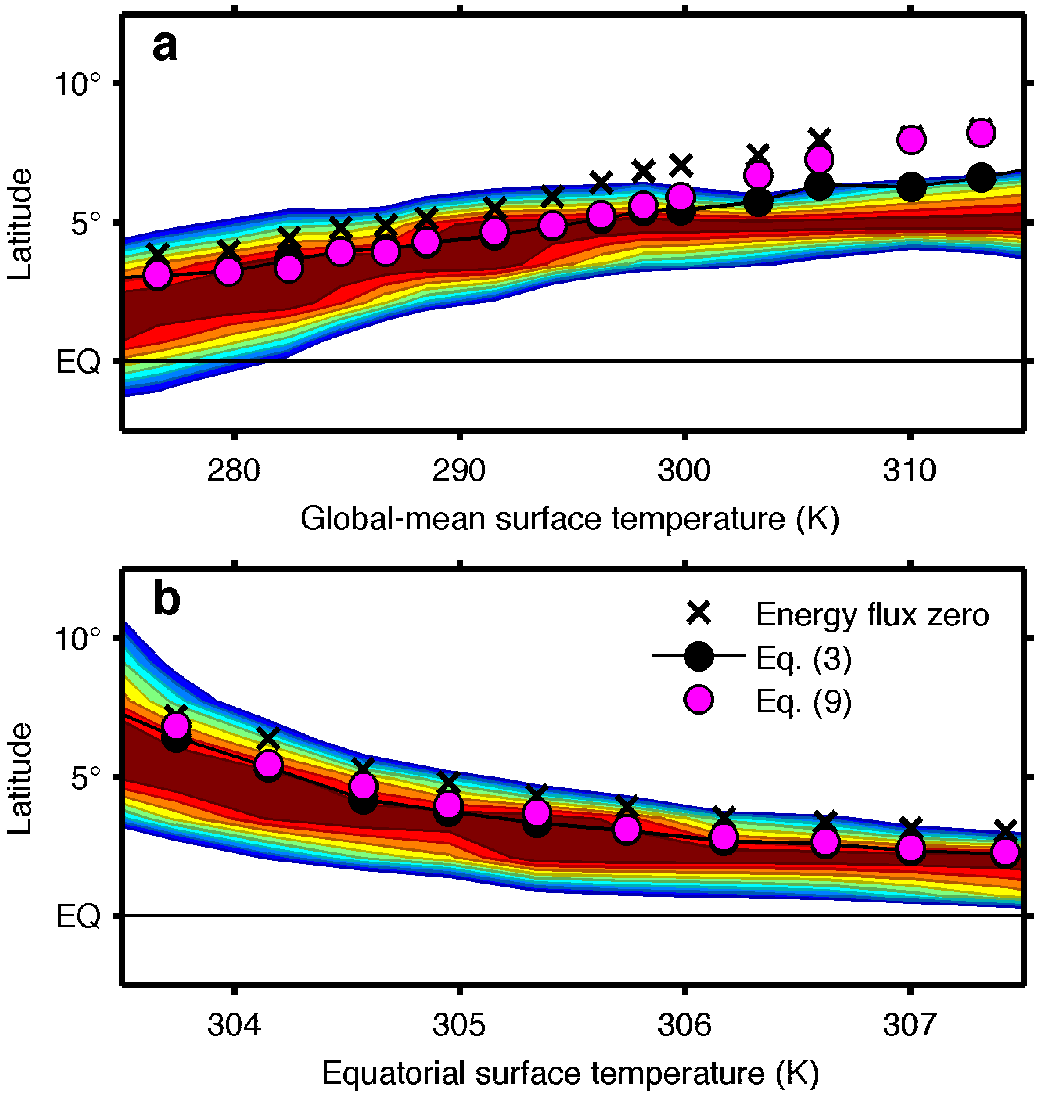

Figure 2.3: ITCZ position in GCM simulations under (a) global and (b) tropical warming. Colors show precipitation normalized by its global maximum, with contours from 0.9 to 1.0. Black crosses indicate where the moist static energy flux is zero. Black dots show the ITCZ latitude δ calculated from Eq. (2.3). Magenta dots show the approximate ITCZ latitude δ calculated from Eq. (2.8). The horizontal axes are (a) global-mean surface temperature and (b) equatorial surface temperature. The ITCZ shifts are qualitatively different in the two series of simulations: Under global warming, the ITCZ shifts are primarily caused by hemispherically asymmetric changes in extratropical latent energy fluxes and associated changes in cross-equatorial energy flux (cf. blue line in Fig. 2.1). Under tropical warming, the ITCZ shifts are primarily caused by changes to the net energy input to the equatorial atmosphere (cf. red line in Fig. 2.1).

because of the increased near-surface specific humidity in the tropics.

Generally, as the longwave optical depth and global-mean surface temperature increase, the ITCZ and its tropical precipitation maximum shift monotonically away from the equator (Fig. 2.3a). Our estimate (2.3) of the ITCZ position captures this shift to within $\lesssim 2^\circ$ (Fig. 2.3a, black dots). If the cross-equatorial energy flux $\langle \overline{v\,h} \rangle_0$ is related to interhemispheric asymmetries as in Eq. (2.4), the resulting estimate of the ITCZ position is essentially indistinguishable from that shown in Fig. 2.3a. The larger errors in the warmer climates arise in part because the ITCZ as defined by the precipitation maximum and the zero of the atmospheric energy flux (Fig. 2.3a, crosses) begin to diverge and are up to 2° apart in the warmest climates.

In the global-warming simulations, changes in δ are primarily associated with hemispherically asymmetric changes in extratropical eddy energy fluxes (Fig. 2.5a). Changes in the net energy input to the equatorial atmosphere by themselves would imply an equatorward shift of the ITCZ as the climate warms (Fig. 2.6a). Their effect (2° equatorward ITCZ shift over the range of simulations) is overcompensated by the effect of the energy flux changes (7° poleward shift). In our simulations, the net energy input to the equatorial atmosphere increases with increasing global-mean surface temperature primarily because the equatorial top-of-atmosphere outgoing longwave radiation decreases as the temperature increases. This is because the atmosphere exports more energy from the tropics to the extratropics in warmer climates, thus increasing the radiative imbalance at the top of the atmosphere at the equator. If changes in δ are regressed onto changes in the cross-equatorial atmospheric energy flux $\langle \overline{v\,h} \rangle_0$ alone, disregarding that the energy input to the equatorial atmosphere also varies, we find that δ increases by 3°–4° for every PW reduction in $\langle \overline{v\,h} \rangle_0$, quantitatively consistent with studies that regress the location of maximum precipitation directly on the cross-equatorial energy transport [2, 8]. However, this overemphasizes the role of the cross-equatorial energy flux, because the energy input to the equatorial atmosphere varies simultaneously. If changes in δ are regressed onto changes in both the cross-equatorial atmospheric energy flux and the net energy input to the equatorial atmosphere, δ increases by 4°–6° for every PW reduction in $\langle \overline{v\,h} \rangle_0$, holding the energy input to the equatorial atmosphere fixed.

Decomposing the cross-equatorial energy flux into components as in Eq. (2.4) shows that the principal reason for the monotonic poleward shift of the ITCZ under global warming lies in a strengthening of extratropical latent energy fluxes and their hemispherically asymmetric component, which overcompensate nonmonotonic changes

in extratropical dry static energy fluxes (Fig. 2.5a). This is in agreement with earlier studies that identified the latent energy flux as the main driver of ITCZ shifts in CO_2-doubling simulations in idealized setups [e.g., 20, 47]. It is also consistent with the notion that latent energy fluxes dominate the poleward energy flux in warm climates [41, 48–50], with pre-existing asymmetries in latent energy fluxes amplifying as the climate warms [51].

The response of the ITCZ location to increases of the longwave optical depth likely depends on the strength of the imposed hemispherically antisymmetric ocean energy uptake/release O in midlatitudes. A stronger pre-existing antisymmetry in ocean energy uptake/release implies a stronger response of the eddy moist static energy flux term in Eq. (2.4) because of the Clausius-Clayperon nonlinearity that governs latent energy flux changes [e.g., 51]. As a consequence, the response of the ITCZ location to increased longwave optical depth may be nonmonotonic for some strengths of the antisymmetric ocean energy uptake/release.

Tropical warming

The contours in Fig. 2.4a show typical mass flux streamfunctions for a cold and a warm case in the tropical warming scenario. The region of maximum low-level upward mass flux and the zero contour of the mass flux streamfunction are located closer to the equator in climates with higher equatorial surface temperatures. At the same time, the Hadley circulation is narrower and stronger, resembling qualitatively (albeit not quantitatively) El Niño conditions on Earth [52]. The precipitation maximum (Fig. 2.4b) is located closer to the equator. The strengthened maximum precipitation in the case with a warmer equatorial surface arises because the mass flux is strengthened and the near-surface specific humidity in the tropics is increased.

Generally, as the imposed ocean energy flux converges at the equator and with it tropical surface temperatures increase, the ITCZ and its tropical precipitation maximum shift toward the equator (Fig. 2.3b). Our estimate (2.3) of the ITCZ position again captures this shift accurately, to within $\lesssim 2^\circ$ (Fig. 2.3b, black dots). As for the global-warming simulations, if the cross-equatorial energy flux $\langle \overline{v\,h} \rangle_0$ is related to interhemispheric asymmetries as in Eq. (2.4), the resulting estimate of the ITCZ position remains essentially indistinguishable from that shown in Fig. 2.3b. But in contrast to the global-warming simulations, changes in δ in the tropical-warming simulations are primarily associated with changes in the net energy input to

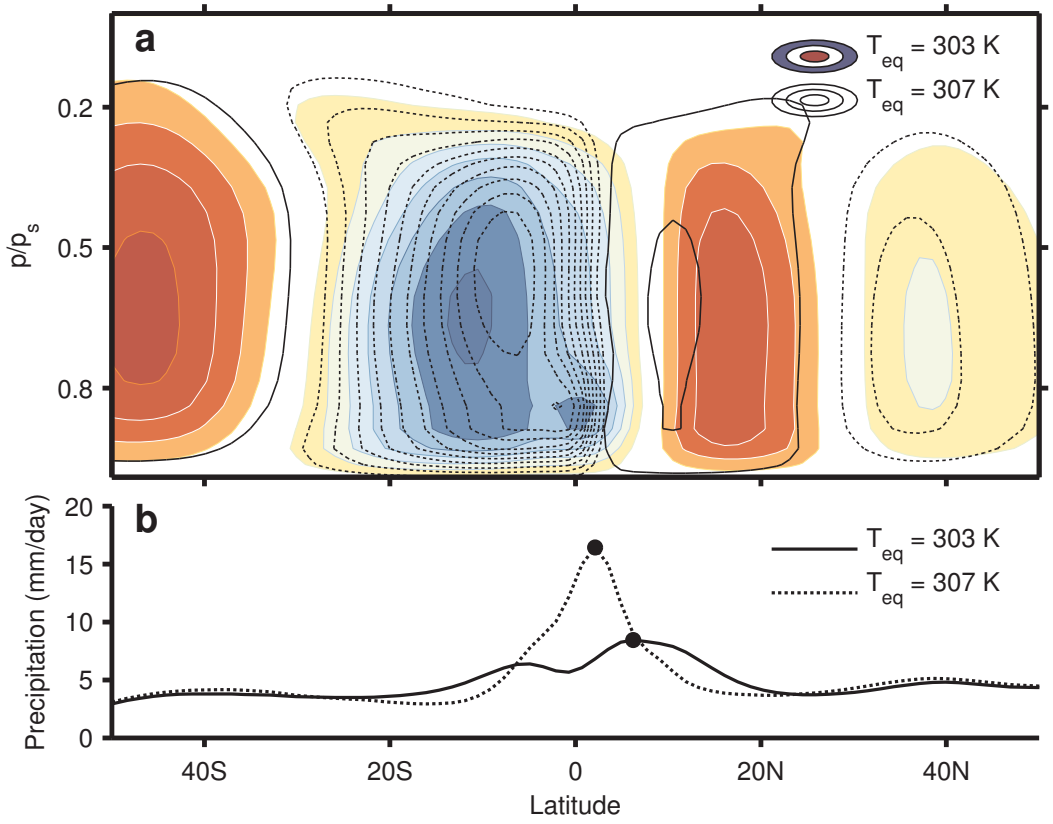

Figure 2.4: (a) Mass flux streamfunction and (b) precipitation for equatorial surface temperatures $T_{\mathrm{eq}} = 303$ K and $T_{\mathrm{eq}} = 307$ K in the tropical warming scenario. Colors and contours as in Fig. 2.2. The maximum and minimum values of the streamfunctions are 6.9×10^{10} kg s^{-1} and -11.5×10^{10} kg s^{-1} at $T_{\mathrm{eq}} = 303$ K, and 8.8×10^{10} kg s^{-1} and -17.8×10^{10} kg s^{-1} at $T_{\mathrm{eq}} = 307$ K. The black dots in (b) mark the precipitation maximum. The ITCZ is generally located closer to the equator in simulations with higher equatorial surface temperatures, and the maximum precipitation is strengthened. In addition, the Hadley cells contract. The zero of the mass flux stream function moves equatorward as equatorial surface temperatures increase, but it remains poleward of the precipitation maximum.

the equatorial atmosphere. The equatorial net energy input increases monotonically and strongly (Fig. 2.6b); however, the cross-equatorial energy flux remains nearly unchanged (Fig. 2.5b).

Increasing the width of the tropical forcing does not change the response qualitatively as long at the impact on moist static energy fluxes associated with extratropical eddies remains small. This is consistent with the linear approximation implicit in (2.3) because the denominator only depends on the amplitude of the net energy input at the equator.

Implications

The simulations illustrate how cross-equatorial energy transport and the net energy input to the equatorial atmosphere act together to determine the ITCZ position. They demonstrate that changes in the ITCZ position do not need to be correlated with changes in cross-equatorial energy transport but can be associated with changes in equatorial net energy input alone.

In reality, most changes in ITCZ position likely are a superposition of changes in tropical energy input and cross-equatorial energy transport. Such changes can be caused by a variety of processes, from changes in cloud albedo and aerosol loading to changes in ocean upwelling. For example, an increased equatorial shortwave albedo (everything else fixed) reduces the net incoming shortwave radiation $\mathcal{S}_0$ and makes the ITCZ position more sensitive to a given cross-equatorial energy transport, leading to a poleward shift of the ITCZ. Similarly, weakened upwelling and energy uptake $\mathcal{O}_0$ by the equatorial oceans leads to an equatorward shift of the ITCZ. Such tropical changes can act together or in concert with changes in extratropical eddy energy fluxes to lead to complex changes in the ITCZ position.

2.5 Closure approximations

While the expressions for the ITCZ position in terms of energy fluxes are relatively accurate, it is desirable to relate the ITCZ position to quantities that are more easily measured or inferred, in particular for climates of the past. To do so, we relate the relevant energy fluxes through a series of closure approximations to near-surface temperatures.

Atmospheric eddy energy fluxes

The eddy energy flux $\langle\overline{v'h'}\rangle = \langle\overline{v's'}\rangle + \langle\overline{v'l'}\rangle$ at the edges of the tropical belt is a mediator between low and high latitudes and communicates extratropical changes to

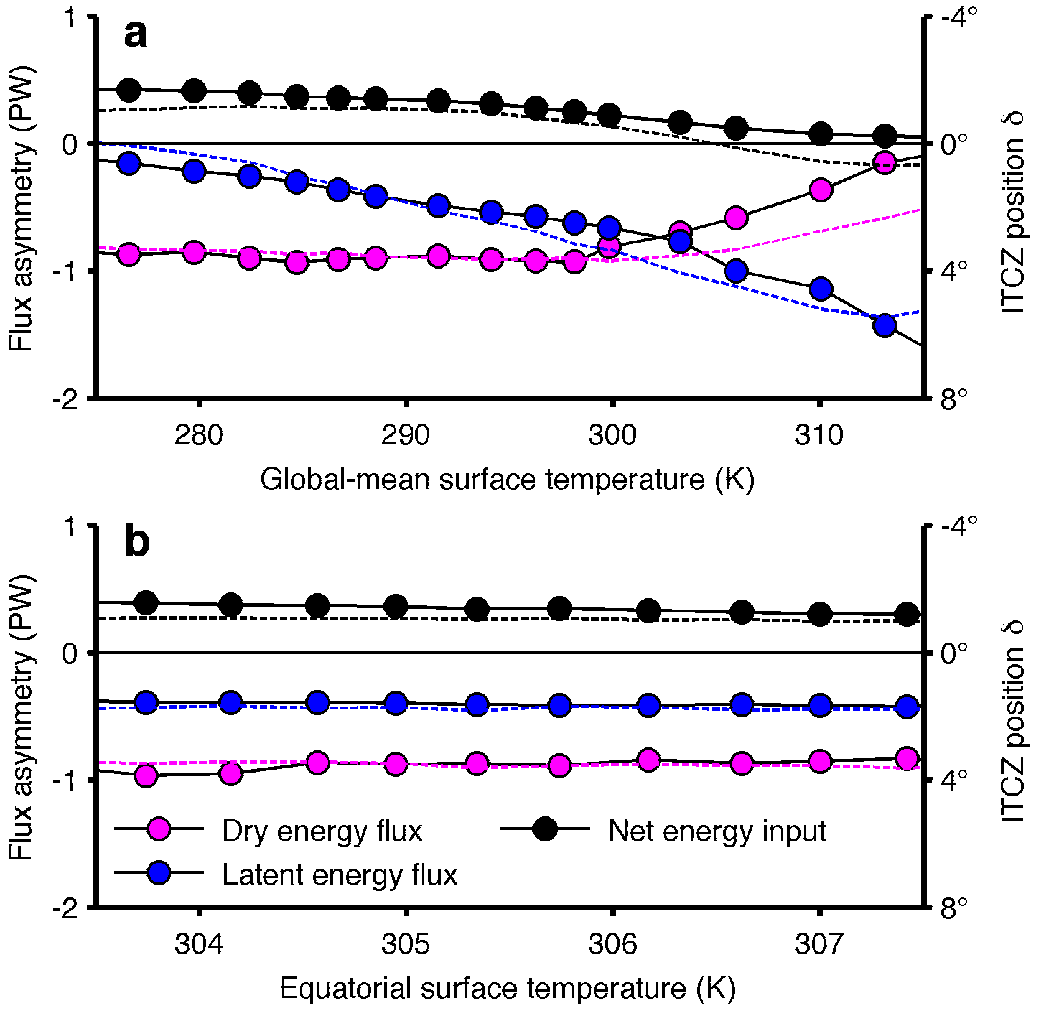

Figure 2.5: Interhemispheric asymmetries in energy fluxes in GCM simulations under (a) global warming and (b) tropical warming. The interhemispheric asymmetries are measured by the arithmetic mean of the fluxes at the subtropical latitude where the mean moist static energy flux $\langle \overline{v}\,\overline{h} \rangle$ in each hemisphere is zero. Plotting symbols and solid lines show the flux asymmetries in the GCM simulations. Dashed lines show the respective approximations (Eqs. 2.5–2.6). The right axis shows the implied ITCZ position when the denominator in Eq. (2.3) is taken from a reference climate with a global-mean surface temperature of 288 K and an equatorial surface temperature of 304 K. Under global warming, the latent energy fluxes experience the largest changes, primarily because of large changes in subtropical saturation specific humidity (cf. Eq. 2.5). Under tropical warming, hemispherically asymmetric changes in energy fluxes are small.

the tropics and tropical changes to the extratropics. The simplest closure approximation of this vertically integrated flux is a diffusive mixing length closure [e.g., 6, 43], which is best justifiable for conserved quantities on scales larger than typical eddy length scales. However, closure approximations for fluxes of latent energy (water vapor) must take into account that moist air parcels from the subtropical boundary layer are transported upward and poleward, losing moisture along the way through cooling, condensation, and precipitation. The vertical structure of the flux must be considered, which can lead to a non-local dependence of water vapor fluxes, for example, on a subtropical specific humidity [41, 45, 48–50, 53, 54].

We use a diffusive closure for the vertically integrated moist static energy flux $\langle\overline{v'h'}\rangle$, which approximates the vertically integrated dry static energy flux $\langle\overline{v's'}\rangle$ in terms of near-surface temperature gradients and the vertically integrated latent energy flux $\langle\overline{v'l'}\rangle$ by taking into account the strong vertical structure of specific humidity through diffusion of moisture along dry isentropes (see Appendix B). The approximate eddy moist static energy flux at the edges of the tropics is given by

$$\langle\overline{v'h'}\rangle \approx \langle\overline{v's'}\rangle\,(1+\beta q_s) \approx \pm\alpha\, v_e \Delta T\,(1+\beta q_s)\,. \tag{2.5}$$

The coefficient α includes the relevant physical constants and depends on the location of the storm track. The velocity v_e is a typical eddy velocity, and $\Delta T = T_{70°\mathrm{N,S}} - T_{20°\mathrm{N,S}}$ is the pole-to-subtropics temperature difference evaluated at the top of the boundary layer between 70° and 20° latitude in each hemisphere (see Appendix B). Annual-mean reanalysis data for Earth's current atmosphere indicate $\alpha \approx 2.3 \times 10^5\,\mathrm{J\,K^{-1}\,m^{-2}}$ in the northern and in the southern hemisphere. The eddy velocity v_e varies in the northern hemisphere between $10\,\mathrm{m\,s^{-1}}$ in winter and $6.5\,\mathrm{m\,s^{-1}}$ in summer and in the southern hemisphere between $9.5\,\mathrm{m\,s^{-1}}$ in winter and $8\,\mathrm{m\,s^{-1}}$ in summer. The temperature difference ΔT between ±70° and ±20° latitude varies in the northern hemisphere between 32 K in winter and 18 K in summer and in the southern hemisphere between 32.5 K in winter and 29.5 K in summer [55]. This formulation also captures the contribution of stationary eddies to the dry static energy flux, although, unlike for transient eddies, it is more difficult to justify using diffusive closures for stationary eddies.

In our simulations, where there are only transient eddies, the formulation (2.5) captures the variations of the interhemispheric asymmetry in the dry static energy fluxes [first term in (2.5)] to within 15% in climates with global-mean surface temperatures $\lesssim$ 305 K (Fig. 2.5). We relate the latent energy flux, directed poleward

and upward approximately along isentropes from the subtropics to the extratropics [e.g., 56], to the dry static energy flux $\langle\overline{v's'}\rangle$ by using the slope of near-surface isentropes averaged over the extratropics and the saturation specific humidity q_s evaluated in the subtropics (see O'Gorman & Schneider [41] and Appendix B). The resulting approximation of the latent energy flux is the dry static energy flux multiplied by the factor βq_s, where β depends on the subtropical relative humidity, near-surface temperature, and extratropical near-surface static stability. For Earth's current atmosphere, reanalysis data indicate $\beta q_s \approx 0.8$ in the northern and 0.9 in the southern hemisphere in the annual mean [55], showing that dry static and latent energy fluxes are of similar importance in both hemispheres. In our simulations, this formulation captures the variations of the interhemispheric asymmetry in the latent energy fluxes to within 30% for climates with global-mean surface temperatures $\gtrsim 285$ K (Fig. 2.5).

For all simulations presented, this closure for eddy moist static energy fluxes is essentially indistinguishable from diffusing moist static energy directly, i.e., approximating $\langle\overline{v'h'}\rangle$ in terms of the near surface moist static energy gradient. The main difference lies in the functional dependence of β on other quantities (see Appendix B). However, the choice of closure does not affect our conclusions in what follows.

Asymmetric energy input to tropical belt

In addition to hemispherically asymmetric eddy energy fluxes at the edges of the tropical belt, the hemispherically asymmetric net energy input to the atmosphere in the tropical belt [second term on right-hand side of (2.4)] also contributes to interhemispheric asymmetries and hence to cross-equatorial energy transport. But in our and other simulations and in observational data [35, 55], the interhemispheric differences in eddy energy fluxes at the edges of the tropical belt contribute at least 50% to the cross-equatorial energy flux. In the simulations, the contribution of the asymmetric net energy input to the tropical belt is smaller, all of it being attributable to asymmetries in the outgoing longwave radiation (Fig. 2.5). We therefore approximate the net energy input to the atmosphere in the tropical belt as

$$-\left\{\int_0^y (\mathcal{S} - \mathcal{L} - O)\, dy\right\}_S^N \approx \gamma\,(T_{20^\circ\mathrm{N}} - T_{20^\circ\mathrm{S}})\,. \tag{2.6}$$

Here, $\gamma \approx 2.8 \times 10^6\,\mathrm{W\,K^{-1}\,m^{-1}}$ for the simulations, and $\gamma \approx 1.7 \times 10^6\,\mathrm{W\,K^{-1}\,m^{-1}}$ for Earth's atmosphere [35]. Asymmetries in ocean energy uptake O between the hemispheres are important for Earth's atmosphere and likely account for much of

the difference in γ to the simulations; hemispheric asymmetries in net shortwave radiation in the tropics may also contribute, although they are small when averaged over the entire hemispheres [38, 57]. In our simulations, this formulation introduces errors less than 30% for global-mean temperatures between 280 K and 300 K, with larger errors in warmer climates (see Fig. 2.5).

The overall error in the cross-equatorial energy transport introduced by the various approximations does not exceed 30% over the range of simulations presented here. This is a relatively good approximation given that the interhemispheric asymmetry is a small difference between the large eddy fluxes in each hemisphere (see Appendix B) and given that global-mean surface temperatures vary by 40 K over the range of simulations.

Equatorial energy input to the atmosphere

For the purpose of this paper, we treat the net incoming shortwave radiation at the equator, $\mathcal{S}_0$, and the equatorial ocean energy uptake, $\mathcal{O}_0$, as external parameters, without attempting to relate them to the climate state. In reality, of course, both are related to the climate state, through the shortwave albedo (e.g., cloudiness) and ocean energy flux, which is intimately coupled to the atmospheric circulation and its energy flux [58, 59]. This leaves us to relate the outgoing longwave radiation at the equator, $\mathcal{L}_0$, to the climate state and specifically the equatorial surface temperature T_0. We do so by relating the surface temperature to the temperature at the emission height H_0 by $T_0 - \Gamma_0 H_0$, where Γ_0 is the vertically-averaged (moist adiabatic) lapse rate at the equator ($\Gamma_0 \approx 5.3\,\mathrm{K\,km^{-1}}$ in Earth's present climate). Linearizing the Stefan-Boltzmann law around a reference temperature $\check{T}$ then gives for the outgoing longwave radiation at the equator,

$$\mathcal{L}_0 \approx \sigma_b \check{T}^4 + 4\sigma_b \check{T}^3 \left(T_0 - \Gamma_0 H_0 - \check{T}\right), \tag{2.7}$$

with the Stefan-Boltzmann constant σ_b. The emission height at the equator varies with the concentration and distribution of infrared absorbers. In Earth's present climate, $H_0 \approx 8\,\mathrm{km}$ is a good approximation [55], but H_0 increases as the concentration of greenhouse gases increases. This gives an excellent approximation of the equatorial outgoing longwave radiation $\mathcal{L}_0$, with errors of less than 10% across our simulations if variations in Γ_0 and H_0 are taken into account but $\check{T} = 250$ K is taken as fixed (Fig. 2.6).

ITCZ position

Combining the above approximations to re-express the ITCZ position (2.3) gives

$$\delta \approx -\frac{1}{a} \frac{\{\alpha\, v_e \Delta T\,(1+\beta q_s)\}_S^N + \gamma\,(T_{20^\circ\mathrm{N}} - T_{20^\circ\mathrm{S}})}{\mathcal{S}_0 - \sigma_b \check{T}^4 - 4\sigma_b \check{T}^3 \left(T_0 - \Gamma_0 H_0 - \check{T}\right) - \mathcal{O}_0}. \tag{2.8}$$

Estimating the different terms from annually and zonally averaged reanalysis data [55] and using 20 W m^{-2} for the net energy input in the denominator [35] gives $\delta \approx 6^\circ$ for the present climate, consistent with observations. The expression (2.8) shows how an expression for the ITCZ position involving energy fluxes can be converted into one involving surface temperatures and, in particular, hemispheric surface temperature contrasts, among other quantities. It makes explicit how perspectives focusing on energy fluxes [e.g., 5, 6] and those focusing on surface temperatures [e.g., 30] can be reconciled.

In our simulations, expression (2.8) captures much of the overall shift of the ITCZ. Under global warming, it captures the poleward shift well for global-mean surface temperatures between 280 K and 300 K (Fig. 2.3a); however, the poleward shift for warmer climates is not estimated accurately because interhemispheric asymmetries in dry static and latent energy fluxes are not estimated accurately (Fig. 2.5a). Under tropical warming, it captures the equatorward shift of the ITCZ over the entire range of simulations (Fig. 2.3b).

Neglecting interhemispheric differences between all components except near-surface temperatures shows why the ITCZ is generally located in the warmer hemisphere,

$$\delta \propto \frac{(T_{70^\circ\mathrm{N}} - T_{70^\circ\mathrm{S}}) - \epsilon\,(T_{20^\circ\mathrm{N}} - T_{20^\circ\mathrm{S}})}{\mathcal{S}_0 - \mathcal{L}_0 - \mathcal{O}_0}. \tag{2.9}$$

Here, $\epsilon \approx 2$ depends only on the parameters multiplying the temperatures in Eq. (2.8). Because in the annual and zonal mean, temperature contrasts between high latitudes of the northern and southern hemisphere (about 7 K) are generally larger than temperature contrasts between the subtropics (about 2 K), the numerator in Eq. (2.9) is positive for Earth's present climate. This leads to a mean ITCZ position $\delta > 0$ in the northern hemisphere. It also explains why the ITCZ position is correlated with interhemispheric temperature differences [60], provided the subtropical temperatures in the northern and southern hemispheres are taken as approximately equal.

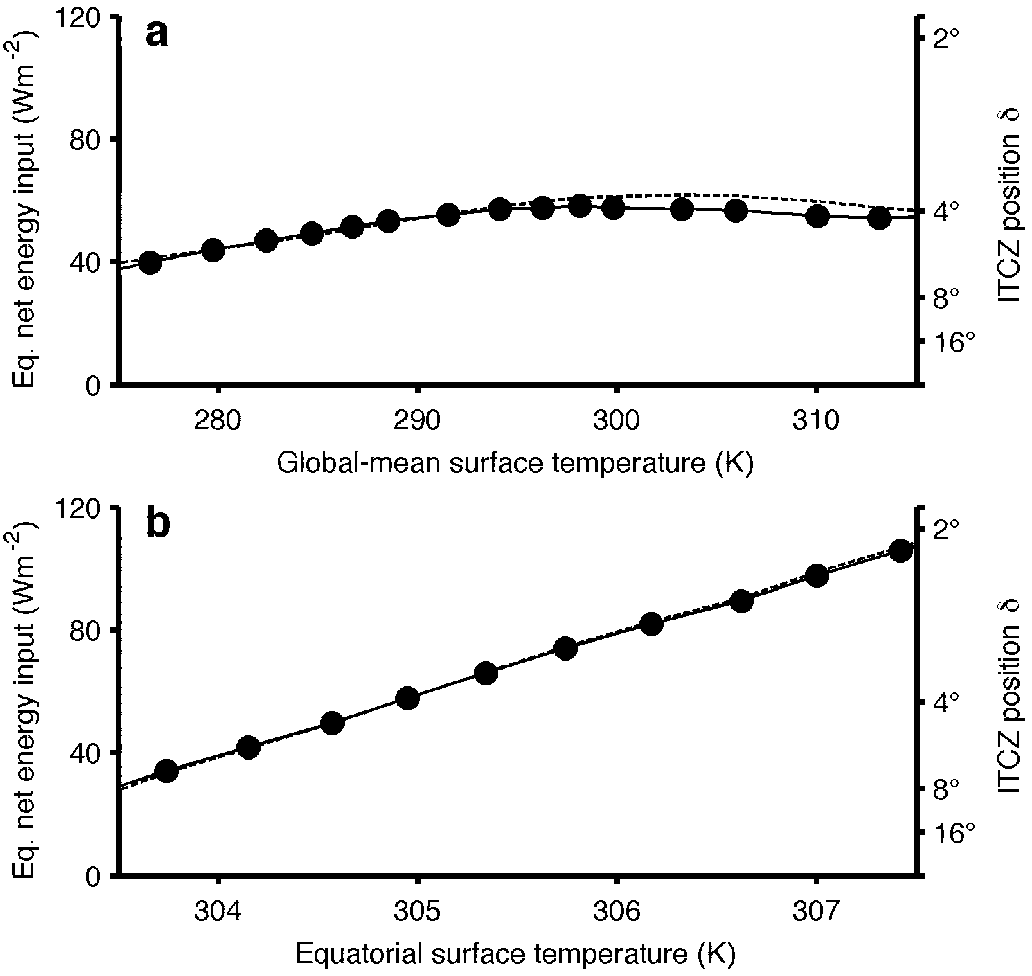

Figure 2.6: Net energy input to the atmosphere at the equator in GCM simulations under (a) global and (b) tropical warming. Dots and solid lines show the GCM results; dashed lines show approximations in which the outgoing longwave radiation is approximated (Eq. 2.7). The right axis shows the implied ITCZ position when the numerator in Eq. (2.3) is taken from a reference climate with a global-mean surface temperature of 288 K and an equatorial surface temperature of 304 K. The reciprocal of the net energy input at the equator is a measure of the sensitivity of the ITCZ position to interhemispheric asymmetries in energy fluxes. Under global warming, the changes in the net energy input by themselves would imply an equatorward shift of the ITCZ in colder climates and little change in warmer climates. But in fact, the ITCZ shifts poleward (Fig. 2.3a), implying changed interhemispheric asymmetries in energy fluxes (Fig. 2.5a) dominate the ITCZ shift. Under tropical warming, the changes in the net energy input imply an equatorward shift of the ITCZ, which in fact occurs (Fig. 2.3b).

2.6 Conclusions and discussion

We have shown that the ITCZ position in the zonal mean is approximately determined by two factors: the cross-equatorial energy transport in the atmosphere, and the net energy input to the equatorial atmosphere (Eq. 2.3). Atmospheric energy fluxes are generally directed away from the ITCZ in the zonal mean, implying that the ITCZ is located close to a zero of the atmospheric meridional energy flux, as has been previously demonstrated [e.g., 5, 6]. For an ITCZ not too far from the equator, so that the atmospheric energy flux can be approximated as varying linearly with latitude between the equator and the ITCZ, it then follows that a northward energy flux across the equator implies an ITCZ in the southern hemisphere, and a southward energy flux across the equator implies an ITCZ in the northern hemisphere. How far from the equator the ITCZ is located is controlled by the divergence of the atmospheric energy flux at the equator, or by the 'slope' of the energy flux as a function of latitude (Fig. 2.1). Because this is equal to the net energy input to the equatorial atmosphere (neglecting energy storage in the atmosphere), it is the net energy input to the equatorial atmosphere that controls the sensitivity of the ITCZ position to cross-equatorial energy transport. The hemispheric energy balance, in turn, shows how the cross-equatorial energy transport is related to interhemispheric contrasts in extratropical eddy energy fluxes and in the tropical energy input to the atmosphere (Eq. 2.4).

Relating extratropical eddy energy fluxes and the tropical net energy input to the atmosphere through a series of closure approximations to surface temperatures, among other factors, we have shown how ITCZ variations associated with energetic changes can be related to temperature changes, both in the tropics and in the interhemispheric temperature contrast (Eqs. 2.8 and 2.9). This reconciles perspectives on the ITCZ position that have focused on energy fluxes with those that have focused on surface temperatures and interhemispheric temperature contrasts. It shows that these perspectives are not mutually contradictory, but are in fact compatible with each other and complementary.

Our theory and simulations allow us to offer unified interpretations of seemingly disparate previous results. Paleoclimatological evidence and more recent observations and simulations show that the ITCZ has shifted in the past and suggest that the ITCZ can shift with variations in atmospheric greenhouse gas concentrations, aerosol loadings, and El Niño [23, 31, 33, 47, 61]. The anticorrelation between ITCZ position and cross-equatorial energy transport has been noted in many previ-

ous studies. But on the basis of that anticorrelation, it has been suggested that for some of the observed and inferred ITCZ shifts—for example, during the Little Ice Age—large changes in cross-equatorial energy transport would be necessary [2]. Our results instead suggest that smaller changes in cross-equatorial energy transport may account for the observed or inferred shifts when changes in the net energy input to the equatorial atmosphere are also considered. In other words, the correlation coefficient between the ITCZ position and the cross-equatorial atmospheric energy transport (or the interhemispheric temperature contrast) depends on climate. For example, in our global warming simulations, the ITCZ position depends approximately linearly on the cross-equatorial atmospheric energy transport, moving 3°–4° poleward for every PW reduction in the energy transport—quantitatively consistent with previous studies [e.g., 2]. However, this overemphasizes the importance of the cross-equatorial energy flux and conceals the role of the equatorial net energy input to the atmosphere, which varies at the same time. If the net energy input to the atmosphere is kept fixed, the ITCZ position moves 4°–6° poleward for every PW reduction in the energy transport—quantitatively consistent with our first-order estimate (2.3).

Previous modeling studies with aquaplanet GCMs with slab oceans have shown that the ITCZ is typically located in the warmer hemisphere because the atmosphere transports energy across the equator into the colder hemisphere [4–6, 20, 29]. In this picture, high-latitude changes (e.g., in ice cover) are communicated to the tropics by large-scale extratropical eddies and ocean circulations. Differential warming in one hemisphere, even far from the equator, can then drive ITCZ shifts toward that hemisphere [2, 28, 30]. Our approximate quantitative expression (Eq. 2.8) for the ITCZ position shows how interhemispheric temperature differences relate to the ITCZ position, namely, primarily through interhemispheric differences in extratropical meridional temperature contrasts.

Because the ITCZ is not only controlled by interhemispheric asymmetries in energy fluxes that lead to cross-equatorial energy transport, but also by the net energy input to the equatorial atmosphere, the ITCZ can shift even without cross-equatorial energy transport changes, for example, when there is reduced equatorial ocean energy uptake, such as during El Niño. This also shows that tropical processes alone (e.g., changes in cloud albedo or energy uptake by the equatorial oceans) can lead to ITCZ shifts. Thus, to understand future ITCZ shifts, it is important to understand not only changes in cross-equatorial energy transport, which can be

remotely triggered, but also tropical changes in equatorial upwelling, El Niño, and in the equatorial cloud and aerosol distributions, as they all enter the equatorial energy balance.

We have approached the question of what sets the position of the ITCZ from an energetic perspective, leading to results that depend, among other factors, on near-surface temperatures. This leaves open the question of what determines the temperatures. Answering that question requires consideration of the angular momentum balance of the atmosphere and how it controls the circulations that accomplish the atmospheric energy transport [e.g., 44, 46, 62, 63]. Additionally, the ITCZ defined by the precipitation maximum is not always co-located with the zero of the atmospheric energy flux, because the maximum upward mass flux and mean precipitation maximum are determined by the meridional derivative of the mass flux streamfunction and not necessarily by where the streamfunction (or the energy flux) vanish [2, 8]. A completely closed theory of the tropical precipitation maximum therefore would require understanding both the angular momentum and energy balances of the tropical troposphere. Additionally, for a theory that can also be applied to seasonal variations, it will be important to have a theory of seasonal ocean energy storage and release. And particularly for monsoon regions, it is questionable whether energy fluxes alone will give a sufficiently accurate picture of ITCZ variations [7]. Even when they do, it may become necessary to go beyond the linear approximations of energy fluxes on which we focused in this paper.

2.7 Appendix A: Description of GCM and simulations

The GCM has a simplified representation of the hydrological cycle and radiative transfer [41, 42]. It only takes into account the liquid-vapor phase transition, has no ice phase, and the latent heat of evaporation is fixed at $L_v = 2.5 \times 10^6\,\mathrm{J\,kg^{-1}}$. It uses a two-stream gray radiation scheme with prescribed and time-invariant optical opacity profiles.

The top-of-atmosphere insolation is imposed as an approximate annual mean,

$$\mathcal{S} = \frac{S_0}{4}\left(1 + \frac{\Delta_s}{4}\left(1 - 3\sin^2\phi\right)\right). \tag{2.10}$$

Here, $S_0 = 1360\,\mathrm{W\,m^{-2}}$ is the solar constant, and $\Delta_s = 1.2$ is a nondimensional measure of the insolation gradient. The shortwave radiative flux is attenuated going downward, with increasing vertical coordinate $\sigma = p/p_s$ (pressure p normalized by surface pressure p_s) by an exponential factor $\exp(-\tau_s\sigma^2)$, where $\tau_s = 0.22$ is

the shortwave optical thickness of the atmosphere. This represents roughly the absorption of shortwave radiation by atmospheric water vapor. However, dynamic radiative water vapor feedback or cloud feedbacks are not taken into account.

Longwave radiation is absorbed by an idealized absorber with a mixture of characteristics of a well-mixed greenhouse gas and water vapor. It has an optical depth $\tau = \eta\tau_{\text{ref}}(\phi)$, where η is a rescaling factor that is varied in the global-warming simulations to rescale the reference optical depth;

$$\tau_{\text{ref}} = \left(f_l\sigma + (1 - f_l)\sigma^4\right)\left(\tau_e + (\tau_p - \tau_e)\sin^2\phi\right). \tag{2.11}$$

Here, $f_l = 0.2$ measures the fraction of the absorber whose optical depth increases with σ (i.e., an approximately well-mixed absorber), $(1 - f_l)$ is the fraction of the water vapor-like absorber, $\tau_e = 7.2$ is the longwave optical depth at the equator, and $\tau_p = 1.8$ is the longwave optical depth at the poles.

The lower boundary is a slab ocean mixed layer with uniform depth $d = 1\,\text{m}$ and with a uniform and constant albedo of 0.3. The surface mixed layer energy budget is given by

$$\rho_0 c_0 d\,\partial_t T_{\text{sfc}} = \mathcal{S}_{\text{sfc}} - \mathcal{L}_{\text{sfc}} - \mathcal{E} - \mathcal{H} - \mathcal{O}, \tag{2.12}$$

where ρ_0 is the surface water density, c_0 is the surface water heat capacity, T_{sfc} is the surface temperature, $\mathcal{S}_{\text{sfc}}$ is the net downwelling shortwave radiation at the surface, $\mathcal{L}_{\text{sfc}}$ is the net upwelling longwave radiation at the surface, $\mathcal{E}$ is the latent heat flux due to surface evaporation, $\mathcal{H}$ is the sensible heat flux, and $\mathcal{O}$ is the ocean energy flux divergence. The surface fluxes $\mathcal{E}$ and $\mathcal{H}$ are represented by standard bulk aerodynamic formulae.

We impose a zonally symmetric and time-independent ocean energy flux divergence (Fig. 2.7),

$$\mathcal{O} = \hat{\mathcal{O}}_s \cos(\phi)^{-1}\left(1 - \frac{\phi^2}{\delta\phi_s^2}\right)\exp\left[-\frac{\phi^2}{2\delta\phi_s^2}\right] \tag{2.13a}$$

$$+ \hat{\mathcal{O}}_a\left(\exp\left[-\frac{(\phi - \phi_{\text{SH}})^2}{2\delta\phi_a^2}\right] - \exp\left[-\frac{(\phi - \phi_{\text{NH}})^2}{2\delta\phi_a^2}\right]\right) \tag{2.13b}$$

$$+ \hat{\mathcal{O}}_t \exp\left[-\frac{\phi^2}{2\delta\phi_t^2}\right]. \tag{2.13c}$$

Here, $\hat{\mathcal{O}}_s$ is the amplitude of the hemispherically symmetric ocean energy flux divergence, and $\delta\phi_s = 11.3°$ (standard deviation of Gaussian) is a measure of its width around the equator. The hemispherically antisymmetric energy flux divergence with amplitude $\hat{\mathcal{O}}_a$ is used to drive the ITCZ off the equator, with $\phi_{\text{NH}} = 60°$,

$\phi_{\mathrm{SH}} = -\phi_{\mathrm{NH}}$, $\delta\phi_a = 7°$, and $\hat{O}_a = 100\,\mathrm{W\,m^{-2}}$ in all simulations. It represents an interhemispheric asymmetry in the high-latitude surface energy balance and can be thought of as a difference in planetary albedo between the northern and southern hemispheres, or as a steady deep ocean circulation that transports energy from the southern to the northern high latitudes. The relatively large amplitude chosen here is necessary to induce sufficiently large ITCZ shifts in our simulations and is not meant to be a faithful representation of the actual antisymmetric component of the annually-averaged surface energy budget on Earth. The tropical ocean energy flux divergence with amplitude $\hat{O}_t$ is used in the tropical warming simulations to change the equatorial energy balance. The standard deviation $\delta\phi_t = 4.9°$ confines this component to the equatorial region.

Moist convection is parameterized by a simplified quasi-equilibrium scheme that relaxes temperatures to a moist adiabat and specific humidity to a profile with a fixed reference relative humidity of 70% [41, 43]. Large-scale condensation is parameterized so that relative humidity on the grid scale does not exceed 100%. The excess water is removed as precipitation, without reevaporation of condensate.

The GCM's dynamical core integrates the primitive equations spectrally at a horizontal resolution of T85 with 30 unevenly spaced vertical σ levels. The spin-up time for the simulations is 2 years from an isothermal resting state. Time averages are taken over 4 years after spin-up.

Global warming simulations

In the global warming simulations, we vary the longwave optical depth $\tau = \eta\tau_{\mathrm{ref}}(\phi)$ by varying the rescaling factor η between 0.4 and 6.0 (18 simulations), as in O'Gorman & Schneider [41]. This results in climates with global-mean surface temperatures between 275 K and 315 K. The amplitudes of the symmetric and tropical ocean energy flux divergences are taken to be zero, $\hat{O}_s = \hat{O}_t = 0$. The simulations overestimate the precipitation and circulation strengths for Earth-like global-mean surface temperatures because the symmetric component of the ocean energy transport is zero [46]. We avoid prescribing a fixed symmetric ocean energy flux, because it leads to spurious double ITCZs in cold climates.

Tropical warming simulations

In the tropical warming simulations, the optical depth is fixed at $\eta = 1.0$, resulting in climates with an Earth-like global-mean surface temperature of 288 K. The amplitude of the symmetric ocean energy flux divergence is fixed at $\hat{O}_t = 50\,\mathrm{W\,m^{-2}}$,

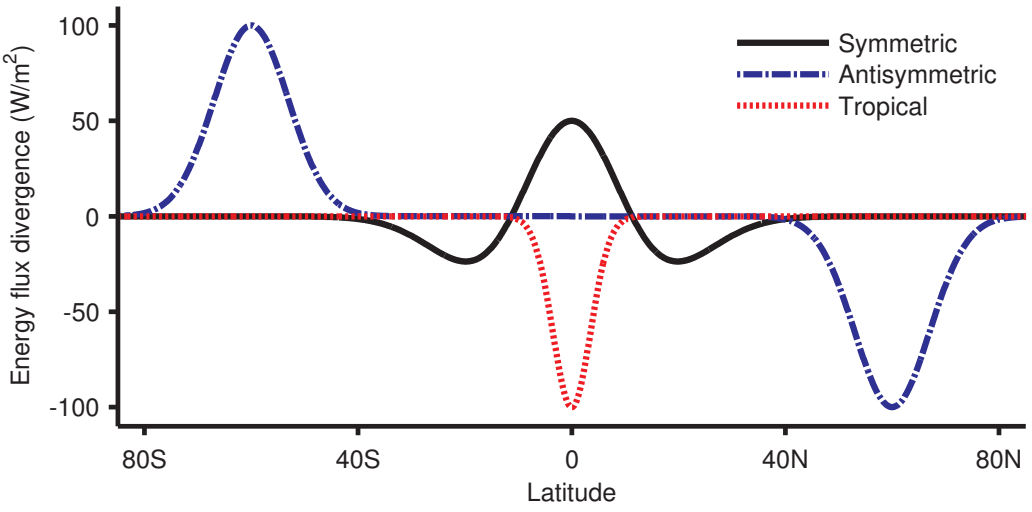

Figure 2.7: The different components of the ocean energy flux divergence used in the idealized GCM experiments. The solid black line shows the symmetric ocean energy flux divergence with amplitude 50 W/m^2 given by the term (2.13a). It is used in the tropical warming experiments. The dashed-dotted blue line shows the antisymmetric ocean energy flux divergence with amplitude 100 W/m^2 that is used to drive the ITCZ off the equator in all experiments. Its functional form is given by the term (2.13b). The dashed red line shows the tropical ocean energy flux divergence with amplitude -100 W/m^2 that is used in the tropical warming simulations. Its functional form is given by the term (2.13c).

and the amplitude of the tropical ocean energy flux divergence $\hat{O}_t$ is varied between $-110\,\mathrm{W\,m^{-2}}$ and $10\,\mathrm{W\,m^{-2}}$ (13 simulations). This results in zonal-mean equatorial surface temperatures between 303 K and 308 K.

2.8 Appendix B: Closure approximations for eddy energy fluxes

Closure 1: Diffusing dry static energy and latent energy separately

At the subtropical latitudes where the vertically, zonally, and temporally averaged moist static energy flux $\langle \overline{v}\,\overline{h} \rangle$ changes sign, we approximate the eddy flux of dry static energy diffusively as

$$\langle \overline{v's'} \rangle \approx \pm c_d\, c_p \frac{p_0}{g} v_e \cos(\phi_s) \Delta T. \tag{2.14}$$

Here, c_d is a constant coefficient, $v_e = \sqrt{\mathrm{EKE}\, g/p_0}$ where EKE is the vertically integrated eddy kinetic energy averaged over the hemisphere, and ϕ_s is the latitude of the eddy kinetic energy maximum (i.e., the storm track location). On the right-hand side, we dropped the overbars of zonal and time mean quantities to improve readability.

We made the following assumptions in this closure:

- The vertically-averaged eddy flux of dry static energy can be represented by near-surface fluxes, and the potential energy flux component $g\langle\overline{v'z'}\rangle$ can be neglected in the extratropics (it vanishes for geostrophic advecting velocities if the zonal and temporal mean is taken along isobars).
- The near-surface eddy fluxes can be closed diffusively invoking an average eddy velocity.
- The relevant length scale for the diffusive closure is given by the energy-containing length scale of the turbulent velocity field, and mean temperatures vary over the same length scale, assumed to extend from the subtropics to near the poles. (This justifies the use of pole-to-subtropics temperature differences provided changes in eddy length scales with climate are ignored.)

For the eddy flux of specific humidity q (or latent energy $L_v q$), we use a scaling in terms of the meridional gradient of specific humidity along (dry) isentropes near the surface $\langle\overline{v'q'}\rangle \propto v_e \partial_y q\big|_\theta$ [41, 48–50]. The meridional gradient of specific humidity $q \approx \mathcal{H} q_s$ along isentropes can be reexpressed in terms of the relative humidity $\mathcal{H}$ and the saturation specific humidity q_s. To calculate derivatives of q_s along isentropes, we use the simplified Clausius-Clapeyron relation also used in the GCM,

$$e_s(T) = e_0 \exp\left[-\frac{L_v}{R_v}\left(\frac{1}{T} - \frac{1}{T_0}\right)\right], \tag{2.15}$$

where $e_0 = 610.78$ Pa, $R_v = 461.5\ \mathrm{JK^{-1}\,kg^{-1}}$ is the gas constant of water vapor, and $T_0 = 273.16$ K. The saturation vapor pressure and the specific humidity q_s are approximately related by $q_s \approx \epsilon_r e_s/p$, with $\epsilon_r \approx 0.622$ being the ratio of the gas constants of dry air and water vapor. The derivative of q along isentropes is then given by

$$\left.\frac{\partial q}{\partial y}\right|_\theta = \frac{\mathcal{H} q_s}{p}\left(\frac{\epsilon_r L_v}{c_p T} - 1\right)\left.\frac{\partial p}{\partial y}\right|_\theta + q_s \left.\frac{\partial \mathcal{H}}{\partial y}\right|_\theta. \tag{2.16}$$

We neglect gradients of relative humidity along isentropes and rewrite the slope of isentropes in terms of meridional gradients of potential temperature $\partial_y\theta$ and static stability $\partial_p\theta$. Averaging over the extratropics introduces the pole-to-subtropics temperature difference ΔT and the location of the storm track as in Eq. (2.14). Because specific humidity decays rapidly with altitude away from the surface, we

obtain a scaling for the eddy moisture fluxes at the edges of the tropics in terms of the subtropical near-surface saturation specific humidity and relative humidity,

$$\langle\overline{v'q'}\rangle \approx \pm c_m \frac{p_0}{g} v_e \cos(\phi_s)\Delta T \left(\frac{\epsilon_r L_v}{c_p T} - 1\right) \mathcal{H}\hat{\Gamma} q_s. \tag{2.17}$$

Here, c_m is a constant coefficient, $\hat{\Gamma}^{-1} = -p_0\partial_p\theta$ is a static stability measure averaged over the extratropics, and T is a near-surface temperature. We evaluate the near-surface temperature T, relative humidity $\mathcal{H}$, and saturation specific humidity q_s in the subtropics at ±20°.

In addition to the assumptions made for the dry fluxes, we made the following assumptions for this closure:

- The near-surface turbulent fluxes can be closed via eddy velocities and gradients along isentropes.
- Gradients of relative humidity along isentropes are unimportant for gradients of specific humidity along isentropes.

Combining the closures for the eddy fluxes of dry static energy and latent energy, we obtain the eddy flux of moist static energy in the subtropics,

$$\langle\overline{v'h'}\rangle = \langle\overline{v's'}\rangle (1 + \beta q_s) \tag{2.18a}$$

$$= \pm\alpha\, v_e \Delta T\, (1 + \beta q_s), \tag{2.18b}$$

$$\alpha = c_d\, c_p \frac{p_0}{g} \cos(\phi_s), \tag{2.18c}$$

$$\beta = \frac{c_m}{c_d}\frac{L_v}{c_p}\left(\frac{\epsilon_r L_v}{c_p T} - 1\right)\mathcal{H}\hat{\Gamma}. \tag{2.18d}$$

Determining the coefficients c_d and c_m by fitting the flux closures to the simulated fluxes at the reference climate with global-mean surface temperature around 288 K gives $c_d \approx 0.03$ and $c_m \approx 0.01$–0.02. Fitting the coefficients to reanalysis data for Earth's atmosphere gives similar results. The differences in c_d and c_m between the hemispheres are around 12% in the GCM simulations and in reanalysis data, and so are negligible for our purposes. This closure is used in Section 4.

Closure 2: Moist static energy diffusion

The above closure (2.18) for the eddy moist static energy flux differs from a diffusive closure for the vertically-averaged eddy moist static energy flux: It assumes that the

vertically-averaged eddy dry static energy flux can be approximated in terms of the meridional temperature gradient, neglecting any vertical structure in dry static energy transport, whereas it explicitly takes into account the vertical structure of the eddy latent energy transport. This is reasonable because specific humidity generally varies much more strongly with height than temperature or dry static energy. Diffusing moist static energy directly without taking into account the vertical structure of specific humidity leads to the following expression for the turbulent moist static energy flux at the edges of the tropics (in terms of near-surface quantities):

$$\langle\overline{v'h'}\rangle \approx \pm c_h \frac{p_0}{g}\, v_e \cos(\phi_s)\Delta h \tag{2.19a}$$

$$= \pm c_h \frac{p_0}{g}\, v_e \cos(\phi_s)\left(c_p\Delta T + L_v\Delta q\right) \tag{2.19b}$$

$$= \pm c_h \frac{p_0}{g}\, v_e \cos(\phi_s)\left(c_p\Delta T + \frac{L_v^2\mathcal{H}q_s}{R_vT^2}\Delta T\right) \tag{2.19c}$$

$$= \pm c_h c_p \frac{p_0}{g}\, v_e \cos(\phi_s)\Delta T\left(1 + \frac{L_v^2\mathcal{H}}{c_pR_vT^2}q_s\right) \tag{2.19d}$$

$$= \langle\overline{v's'}\rangle\,(1+\beta' q_s), \tag{2.19e}$$

$$\alpha' = c_h c_p \frac{p_0}{g}\, v_e \cos(\phi_s), \tag{2.19f}$$

$$\beta' = \frac{L_v^2\mathcal{H}}{c_pR_vT^2}. \tag{2.19g}$$

Here, $c_h = c_d$ is a dimensionless coefficient and h, T, $\mathcal{H}$, q are evaluated near the surface. Comparing β from the closure (2.18) with β' from (2.19) reveals the difference between the two approaches. For Earth's climate $\beta' q_s \approx 1$. The closure (2.19) overestimates the latent energy transport for Earth-like global mean surface temperatures ($T \approx 290$ K) by 20–25% in our simulations, but it has the virtue of only requiring one fitting parameter c_h.

For the inferences in Section 4, both closure schemes are equally useful; the choice of closure does not affect our conclusions.

Chapter 3

THE EQUATORIAL ENERGY BALANCE, ITCZ POSITION, AND DOUBLE ITCZ BIFURCATIONS

1. Bischoff, T. & Schneider, T. The equatorial energy balance, ITCZ position, and double ITCZ bifurcations. *J. Climate* **29.** doi:10.1175/JCLI-D-15-0328.1 (2016).

3.1 Abstract

The intertropical convergence zone (ITCZ) migrates north–south on seasonal and longer time scales. Previous studies have shown that the zonal-mean ITCZ displacement off the equator is negatively correlated with the energy flux across the equator: When the ITCZ lies in the northern hemisphere, energy flows southward across the equator, and vice versa. The hemisphere that exports energy across the equator is the hemisphere with more net energy input, and it is usually the warmer hemisphere. But states with a double ITCZ straddling the equator also occur, for example, seasonally over the eastern Pacific, and frequently in climate models. Here it is shown how the ITCZ position is connected to the energy balance near the equator in a broad range of circumstances, including states with single and double ITCZs. Taylor expansion of the variation of the meridional energy flux around the equator leads to the conclusion that for large positive net energy input into the equatorial atmosphere, the ITCZ position depends linearly on the cross-equatorial energy flux. For small positive equatorial net energy input, the dependence of the ITCZ position on the cross-equatorial energy flux weakens to the third root. When the equatorial net energy input or its curvature becomes negative, a bifurcation to double-ITCZ states occurs. Simulations with an idealized aquaplanet general circulation model (GCM) confirm the quantitative adequacy of these relations. The results provide a framework for assessing and understanding causes of common climate model biases and for interpreting tropical precipitation changes, such as those evident in records of climates of the past.

3.2 Introduction

The bulk of the tropical precipitation falls in the intertropical convergence zone (ITCZ), a band of convective clouds in the tropics that migrates meridionally on

seasonal and longer timescales. In the zonal mean, precipitation has one maximum that migrates from the northern hemisphere tropics in boreal summer to the southern hemisphere tropics in boreal winter. Locally, however, the precipitation can have more than one maximum in a given sector of longitudes. For example, over the eastern Pacific, the ITCZ is located north of the equator most of the year, meandering by a few degrees latitude around 6°. However, for a brief period in spring [64, 65], it splits into two ITCZs straddling the equator (Fig. 3.1a). Current climate models exaggerate this split into two ITCZs (Fig. 3.1b), leading to the well known double-ITCZ bias of the models [e.g., 9, 66].

Many previous studies, analyzing observations and simulations, have shown that the position of the ITCZ is negatively correlated with the strength of the zonal-mean energy flux across the equator [e.g., 2, 4–6, 20, 29]. Because the energy flux across the equator is generally directed from the warmer into the cooler hemisphere and strengthens with the temperature contrast between the hemispheres [67], the ITCZ position is also correlated with the interhemispheric temperature contrast [e.g., 3, 7, 30, 60]. Despite this progress, however, it has remained unclear how the ITCZ position is generally related to the atmospheric energy balance. We have recently shown that if the meridional energy flux varies approximately linearly with latitude around the equator, the ITCZ position is proportional to the strength of the cross-equatorial energy flux and inversely proportional to the flux divergence at the equator, or the equatorial net energy input [1, 67]. Here we expand on that work to show how the ITCZ position relates to the energy balance near the equator more generally, even when the energy flux varies nonlinearly with latitude around the equator. This also provides a framework within which bifurcations to double-ITCZ states, such as those occurring seasonally over the Pacific or frequently in climate models, can be understood and analyzed.

As in Bischoff & Schneider [67], we test the theoretical developments to be presented with simulations with an idealized aquaplanet GCM. This affords tests over a very broad range of simulated climates, with continuous variations of ITCZ positions and bifurcations from single to double ITCZs. Section 3.3 provides an overview over the idealized GCM used in this study and introduces the different forcing scenarios with which we generate a wide range of different ITCZs. Section 3.4 describes how the ITCZ position relates to mass and energy fluxes. Section 3.5 discusses how the ITCZ position is linked to the equatorial energy balance, and specifically to the meridional energy flux and its derivatives at the equator. The theoretical developments are

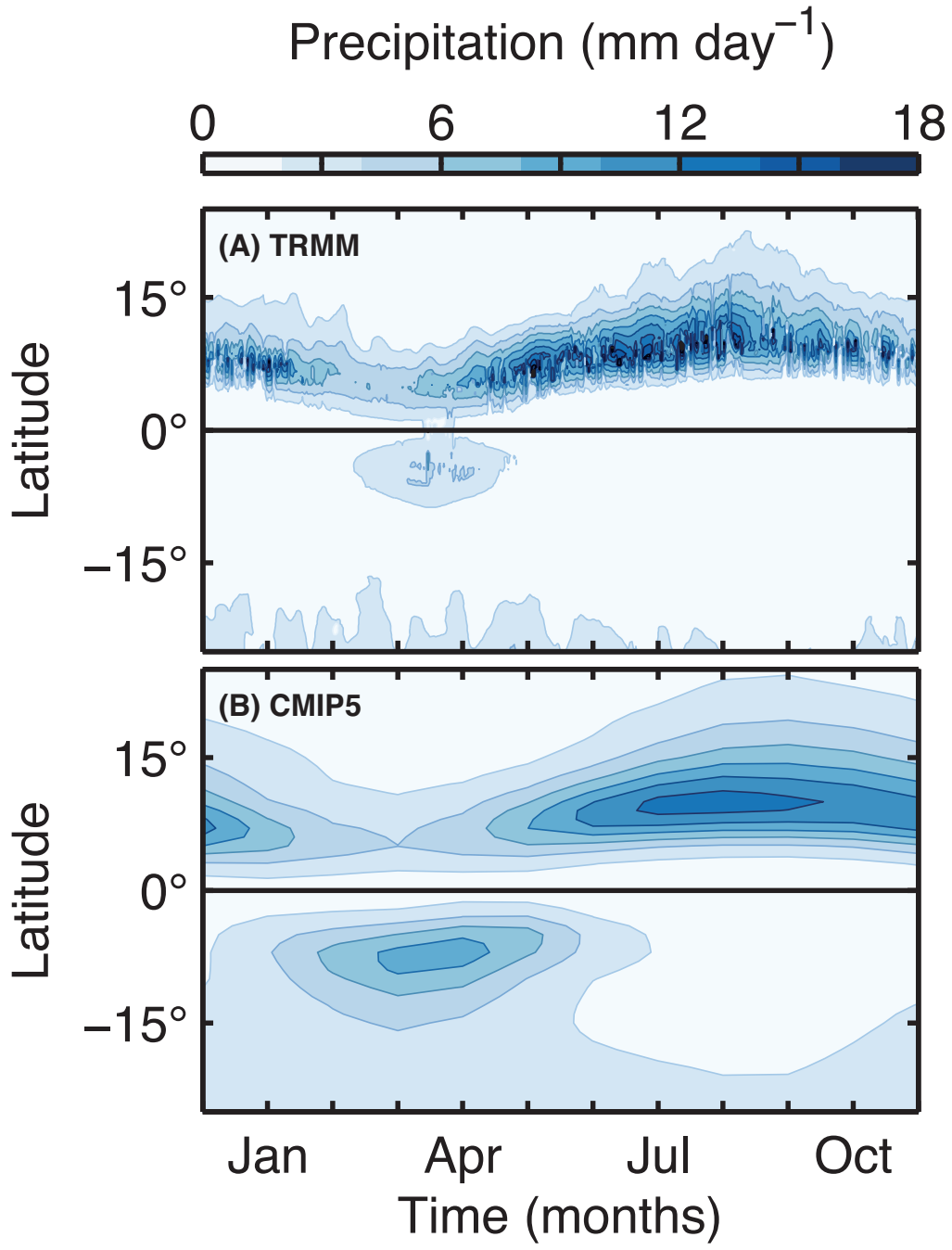

Figure 3.1: Annual cycle of eastern Pacific precipitation in observations and climate simulations. (a) Observed daily precipitation rates from the Tropical Rainfall Measuring Mission (TRMM) Multisatellite Precipitation Analysis (TMPA, [68]), averaged over the years 1998–2012. (b) Simulated monthly precipitation rates from the ensemble mean of CMIP5 models, including all models for which these data are available. (For models for which multiple runs were available, only the first one is included.) In both panels, the precipitation rates are averaged over the longitude sector between 100°W and 140°W. During spring in the eastern Pacific, the ITCZ splits into two ITCZs north and south of the equator in observations and simulations. However, climate models exaggerate this split in duration and intensity.

illustrated and tested with the idealized GCM simulations. Section 3.6 summarizes our results and discusses some of their implications for climate modeling and the interpretation of climate records. The appendix contains theoretical considerations that supplement those in Section 3.5.

3.3 Idealized GCM simulations

Model

The idealized GCM used in this study integrates the hydrostatic primitive equations using the spectral dynamical core of the Geophysical Fluid Dynamics Laboratory's Flexible Modeling System. It uses T85 spectral resolution in the horizontal and, in the vertical, 30 unevenly spaced σ levels, where $\sigma = p/p_s$, with p denoting pressure and p_s surface pressure. The GCM is similar to the one described in Frierson [43], O'Gorman & Schneider [41], or Merlis *et al.* [69]. It employs a two-stream gray radiation scheme, with shortwave and longwave absorption in the atmosphere modeled using time-independent zonally symmetric absorber profiles. Atmospheric scattering of radiation is not explicitly taken into account; the effect of shortwave scattering on the surface energy balance is taken into account by using an enhanced surface albedo [41].

The GCM has a simple representation of the hydrological cycle, modeling only the vapor-liquid phase transition with a fixed latent heat of vaporization $L_v = 2.6 \times 10^6$ J kg^{-1}. Water vapor condenses when saturation is reached at the grid scale. Additionally, the model also uses a quasi-equilibrium convection scheme that relaxes convectively unstable atmospheric columns to a moist-pseudoadiabatic temperature profile with a fixed relative humidity of 70% [41, 43]. Re-evaporation of precipitation is not taken into account, and precipitation from convection and grid-scale condensation is returned to the surface instantly.

The lower boundary is modeled as a slab ocean surface with a constant uniform albedo of $\alpha = 0.3$, satisfying the surface energy balance

$$\rho c_0 d\, \partial_t T_{\mathrm{sfc}} = \mathcal{S}_{\mathrm{sfc}} - \mathcal{L}_{\mathrm{sfc}} - \mathcal{E} - \mathcal{H} - \mathcal{O}, \tag{3.1}$$

where the constant $\rho = 1000$ kg m^{-3} denotes the surface water density, $c_0 = 4000$ J kg^{-1} K^{-1} the surface water heat capacity, $d = 1$ m the depth of the ocean slab (coarsely representing the mixed layer); and the variable T_{sfc} denotes the surface temperature, $\mathcal{S}_{\mathrm{sfc}}$ the net downwelling shortwave radiation at the surface, $\mathcal{L}_{\mathrm{sfc}}$ the net upwelling longwave radiation at the surface, $\mathcal{E}$ the latent heat flux associated

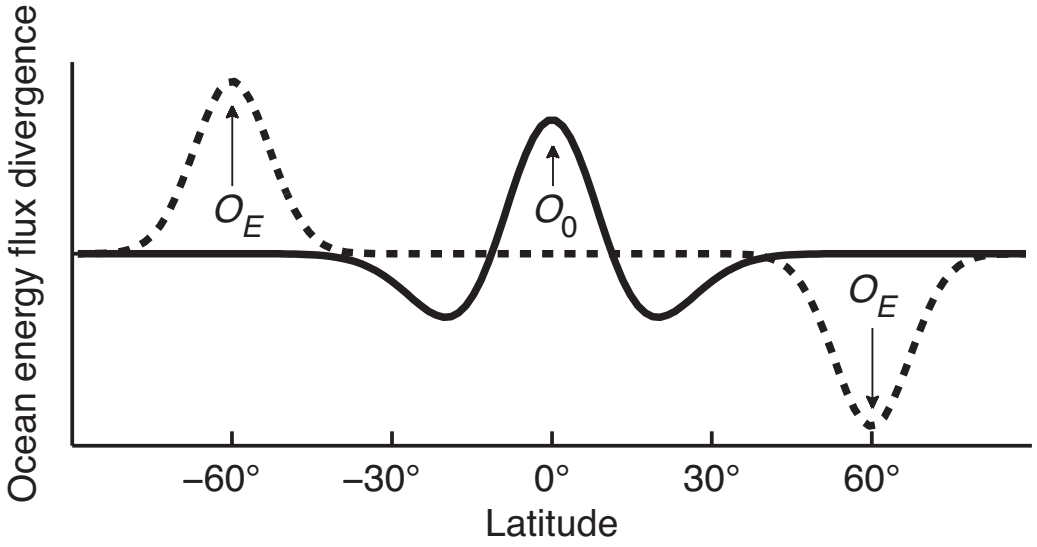

Figure 3.2: Sketch of the imposed ocean energy flux divergence in the idealized GCM simulations. The two parameters varied are O_0, the amplitude of the equatorial ocean energy flux divergence, and O_E, the amplitude of the extratropical ocean energy flux divergence. The solid line shows the symmetric component of the ocean energy flux divergence, and the dashed line shows the antisymmetric component. Both are varied independently of each other from 0 W m^{-2} to 100 W m^{-2} in steps of 10 W m^{-2}, resulting in a total of 121 simulations.

with surface evaporation, and $\mathcal{H}$ the sensible heat flux. The fluxes $\mathcal{E}$ and $\mathcal{H}$ are represented via standard bulk aerodynamic formulae.

The term O in the surface energy balance (3.1) represents ocean energy flux divergence and is the the primary quantity we vary to generate different ITCZ structures. The ocean energy flux divergence is prescribed to be time-independent and zonally symmetric, and of the form (see Fig. 3.2)

$$O = O_0 \cos(\phi)^{-1} \left(1 - \frac{\phi^2}{\delta\phi_0^2}\right) \exp\left[-\frac{\phi^2}{2\delta\phi_0^2}\right] \tag{3.2a}$$

$$+ O_E \exp\left[-\frac{(\phi + \phi_{\mathrm{NH}})^2}{2\delta\phi_E^2}\right] \tag{3.2b}$$

$$- O_E \exp\left[-\frac{(\phi - \phi_{\mathrm{NH}})^2}{2\delta\phi_E^2}\right]. \tag{3.2c}$$

Here, O_0 and O_E are parameters that are used to vary the structure of tropical precipitation, ϕ denotes latitude, $\phi_{\mathrm{NH}} = 60°$ is the latitude at which perturbations of the extratropical ocean energy flux divergence (amplitude O_E) are centered, and

$\delta\phi_0 = 16^\circ$ and $\delta\phi_E = 7^\circ$ are fixed widths of variations in ocean energy flux divergence. The values of $\delta\phi_E$ and ϕ_{NH} are chosen so that the part of O that is antisymmetric about the equator is approximately zero within the tropics ($\pm 30^\circ$ latitude), similar to what was done in Kang *et al.* [5, 6]. The antisymmetric part of O resembles the ocean energy flux divergence of an idealized deep overturning circulation that transports heat from the southern hemisphere high latitudes to the northern hemisphere high latitudes. The value of $\delta\phi_0$ is chosen so that the spatial structure of the symmetric part of O approximately resembles the symmetric part of the zonal-mean ocean energy flux divergence inferred from space-based measurements and reanalysis data [e.g., 35, 70, 71]; it also resembles the ocean energy flux divergence in a zonally symmetric wind-driven surface ocean that transports heat from the deep tropics to the subtropics [46, 58]. Both the symmetric and the antisymmetric components of O integrate to zero in an area-weighted sense.

Simulation series

To test and illustrate the theory to be outlined in section 3.5, we performed simulations without a seasonal cycle, similar to the ones in Kang *et al.* [5, 6] and Bischoff & Schneider [67], varying O_0 and O_E independently from 0 W m^{-2} to 100 W m^{-2} in steps of 10 W m^{-2}. The range of O_0 is representative of equatorial ocean energy flux divergences on Earth derived from space-based measurements and reanalysis data, which take values that can exceed 100 W m^{-2}, e.g., in the eastern Pacific [Fig.2 in 71]. On Earth in the zonal mean, the equatorial ocean energy flux divergence assumes values around 50–60 W m^{-2} [Fig.3 in 35]. A cross-equatorial oceanic heat transport of about 0.4 PW as observed on Earth [36, 72] corresponds to an extratropical forcing amplitude O_E of about 10 W m^{-2}.

Fig. 3.3 shows the cross-equatorial atmospheric moist static energy flux for all simulations. We find that it depends nearly linearly on O_E and is only weakly dependent on O_0. Changing O_E can therefore be thought of changing the cross-equatorial atmospheric moist static energy flux, while changing O_0 leaves it relatively unchanged.

Figure 3.4 shows mass flux streamfunctions for 9 representative simulations. The black triangles indicate the ITCZ position, identified as the global precipitation maximum. For all values of O_0, the ITCZ moves farther into the hemisphere that receives more energy as O_E is increased, as was found in previous studies [e.g., 2, 5, 6, 20, 29]. Concurrently, the cross-equatorial branch of the mass flux streamfunction

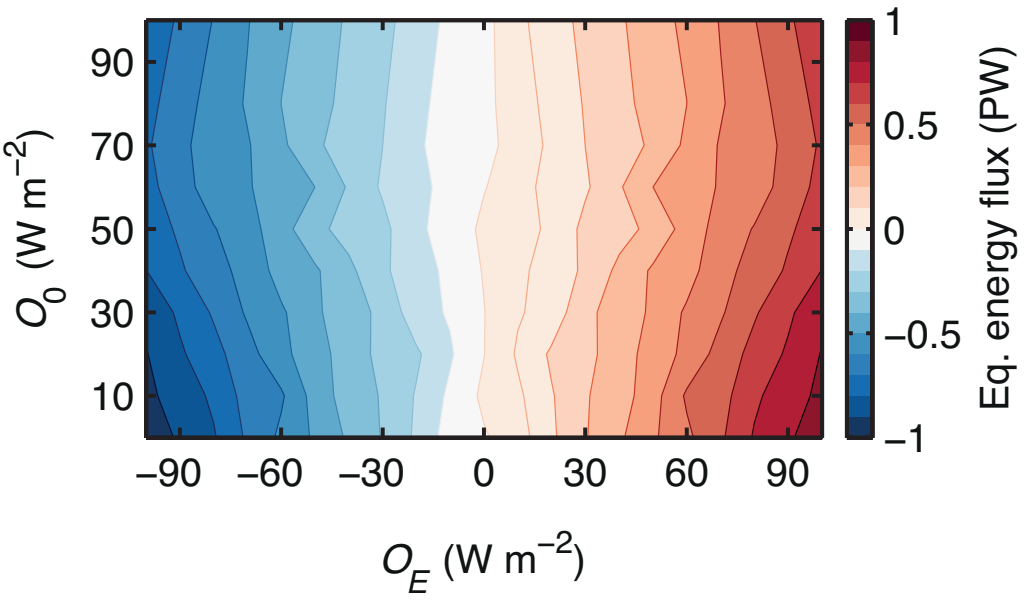

Figure 3.3: Cross-equatorial atmospheric moist static energy flux for all 121 simulations. The cross-equatorial energy flux is weakly sensitive to the ocean energy flux divergence at the equator, O_0, and it varies approximately linearly with O_E for fixed O_0. Only simulations with positive O_E were performed, and the data points are mirrored about $O_E = 0$.

extends farther from the ITCZ across the equator, so that the subtropical terminus of the Hadley circulation in the opposite hemisphere varies little compared with the ITCZ position. The latitude of the ITCZ and of the zero of the streamfunction in the mid-troposphere are approximately (within ∼2°) co-located in all simulations.

3.4 ITCZ, energy flux equator, and moist static energy maximum

In the zonal and temporal mean, the ITCZ can be identified with the global precipitation maximum. Because evaporation rates E around the ITCZ vary more weakly in time and space than precipitation rates P, the ITCZ can also be identified with the maximum of the moisture flux convergence, which in a statistically steady state balances the net precipitation $P - E$,

$$P - E = -\partial_y \langle \overline{vq} \rangle. \tag{3.3}$$

Here, angle brackets $\langle \cdot \rangle$ denote a mass-weighted vertical integral over atmospheric columns, and overbars $\overline{(\cdot)}$ denote a zonal and temporal mean, possibly restricted to a sector of longitudes into which zonal fluxes can be neglected. We use local Cartesian coordinates for notational convenience, with $y = a\phi$, Earth's radius a, and latitude

ϕ; however, we perform all numerical calculations in spherical coordinates. In Earth's atmosphere, the moisture flux convergence on the right-hand side of (3.3) is dominated by the time- and zonal-mean circulation, but eddies also contribute [73–75]. However, the eddy contributions do not substantially shift the maximum of the moisture flux convergence, so the ITCZ can be identified with the maximum of the moisture flux convergence associated with the mean meridional circulation alone, $-\partial_y \langle \bar{v}\, \bar{q} \rangle$. Further approximating the moisture flux $\langle \overline{v}\, \overline{q} \rangle$ by the mean meridional mass flux and specific humidity q_s near the surface yields (see Appendix A for details)

$$-\partial_y \langle \bar{v}\, \bar{q} \rangle \approx \frac{q_s}{2\pi a \cos(\phi)} \partial_y \Psi_{\max}(\phi), \tag{3.4}$$

where $\Psi_{\max}$ is the mass flux streamfunction at the level of its extremum within the Hadley cells (this level typically lies in the lower troposphere above the planetary boundary layer). The relation (3.4) assumes that the near-surface specific humidity varies meridionally on larger scales than the streamfunction Ψ, and it neglects meridional derivatives of $\cos(\phi)$. Because the vertical mass flux is $\propto \cos^{-1}(\phi)\partial_y \Psi$, the relation (3.4) implies that the maximum moisture flux convergence associated with the mean meridional circulation, and thus the ITCZ, are located where the vertical water vapor transport is maximal [cf. 2]. If, additionally, the mass flux streamfunction Ψ in the vicinity of the ITCZ is approximately antisymmetric about the ITCZ, so that $\partial_{yy} \Psi_{\max} = 0$ at the ITCZ, the latitude of the ITCZ will coincide with the zero of the streamfunction, $\Psi_{\max}(\phi) = 0$. This is approximately the case in our GCM simulations (Fig. 3.4).

Similar reasoning based on the same approximations also provides a basis for approximately identifying the ITCZ with the energy flux equator: the zero of the atmospheric meridional energy transport [e.g., 4, 6]. In the vicinity of the ITCZ, the flux of moist static energy $h = c_p T + gz + L_v q$ (symbols have their usual meanings) associated with the mean meridional circulation can be approximated as

$$\langle \bar{v}\, \bar{h} \rangle \approx -\frac{\Delta h}{2\pi a \cos(\phi)} \Psi_{\max}(\phi), \tag{3.5}$$

where Δh is a gross moist stability, the effective moist static energy difference between the upper and lower branches of the mean mass transport circulation ([34, 76]; see Appendix A for details). This relation implies that to the extent that the latitude of the ITCZ coincides with a zero of the mass flux streamfunction, where $\Psi_{\max}(\phi) = 0$ (or with locations where the gross moist stability Δh vanishes), it also coincides with the zero of the energy flux associated with the mean meridional

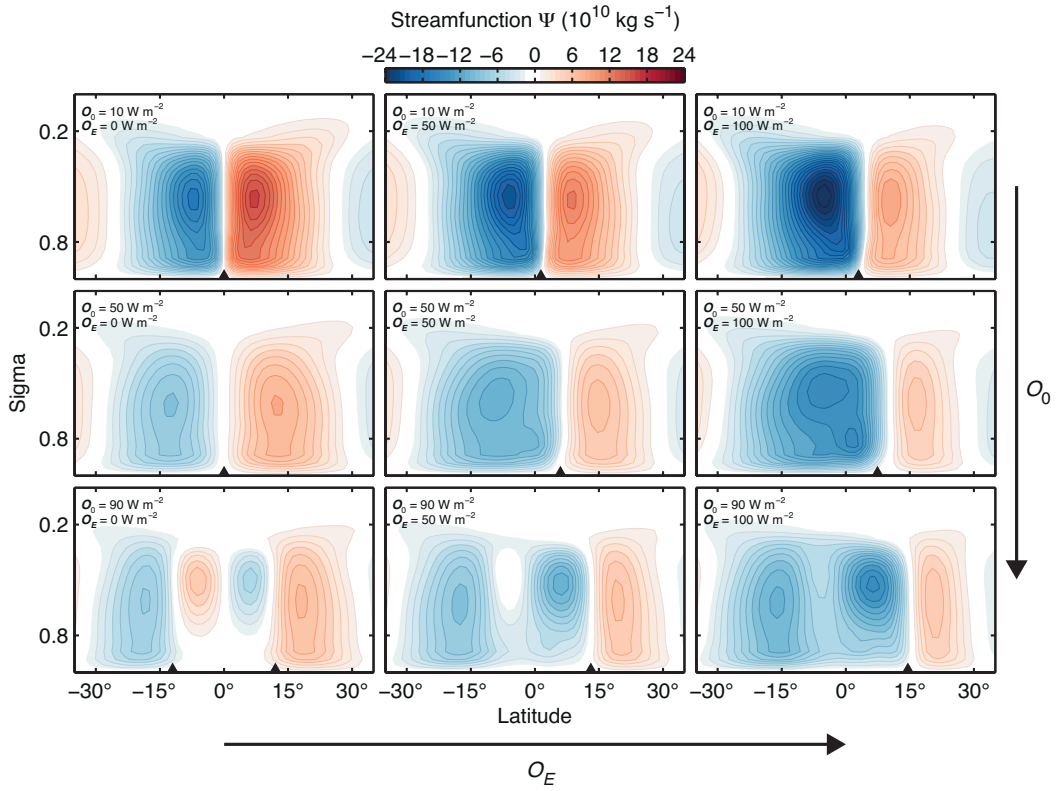

Figure 3.4: Mass flux streamfunction Ψ for nine simulations with different O_0 and O_E. The ocean energy flux divergence at the equator, O_0, increases from top to bottom, and the extratropical ocean energy flux divergence, O_E, increases from left to right. Black triangles indicate the ITCZ position for each simulation, identified as the global precipitation maximum. As O_0 and O_E are increased, the ITCZ moves farther into the more strongly heated hemisphere. For the simulations with $O_E = 0$, an increase in O_0 eventually leads to a double ITCZ, associated with an atmospheric energy transport from the subtropics to the equator that partially compensates for the strong equatorial ocean cooling (bottom left panel).

circulation, where $\langle \bar{v}\,\bar{h} \rangle = 0$. In other words, the atmospheric mean meridional circulation transports energy away from the ITCZ, and the associated energy flux changes sign at the ITCZ, like the mass flux in the upper branches of the circulation. If, additionally, eddy energy fluxes do not substantially modify the zero of the energy flux, the ITCZ approximately coincides with the energy flux equator, the zero of the total meridional energy flux $\langle \overline{vh} \rangle$ [5]. This is the case in our statistically zonally symmetric GCM simulations (Fig. 3.5).

A further connection between the ITCZ position and energetic quantities can be made if the zero contour of the mass flux streamfunction is approximately vertical in

the free troposphere, as it is in our simulations (Fig. 3.4) and in Earth's atmosphere [e.g., 44]. In that case, the zero of the mass flux streamfunction also approximately coincides with the moist static energy maximum near the surface [77]. This connection between the zero of the streamfunction and the near-surface moist static energy maximum arises because, in the vicinity of the ITCZ, the Hadley cells are nearly angular momentum–conserving, which means that streamlines and angular momentum contours coincide [44, 63]. A vertical zero contour of the streamfunction

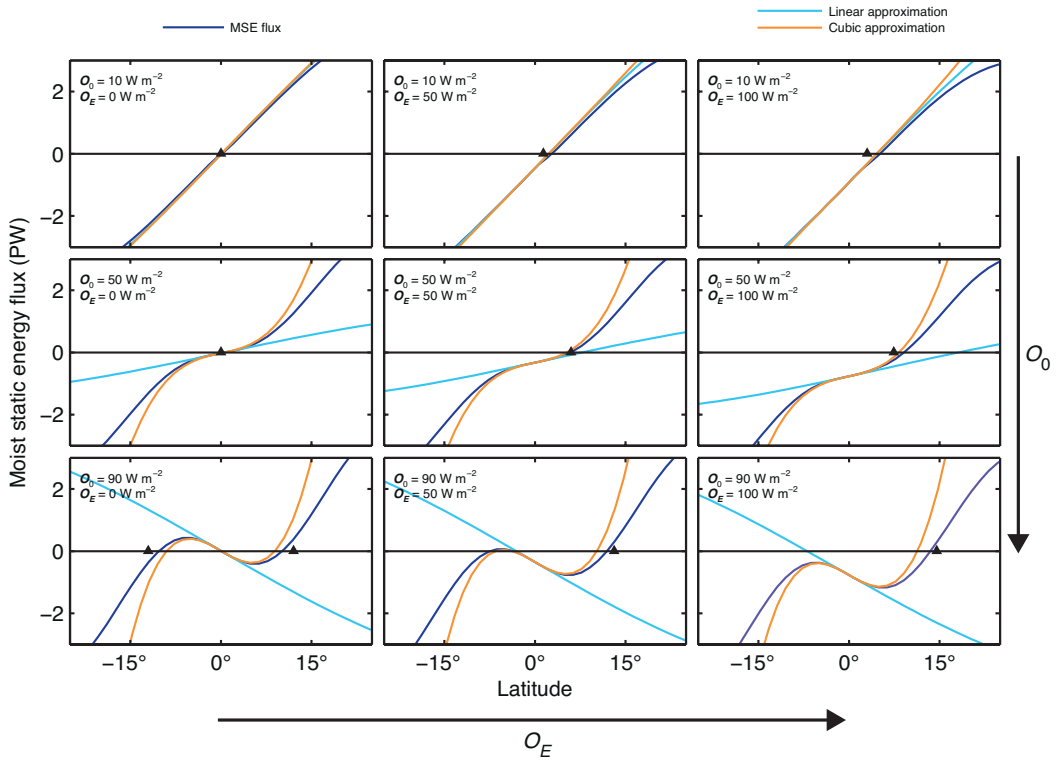

Figure 3.5: Zonal-mean column moist static energy flux $\langle \overline{vh} \rangle$ (dark blue) and linear approximations (light blue) and cubic approximations (orange) for the nine simulations with different O_0 and O_E in Fig. 3.4. As in Fig. 3.4, the black triangles indicate the ITCZ position for each simulation. The ITCZ (black triangles) and the energy flux equator (zero of blue line, $\langle \overline{vh} \rangle = 0$) vary together in all simulations. The linear approximation (3.8) approximates $\langle \overline{vh} \rangle$ well for simulations with low O_0 between $-15°$ and $15°$. For $O_0 \gtrsim 50$ W m^{-2}, the linear approximation breaks down, and a cubic approximation (3.9) becomes necessary to capture the energy flux equator approximately.

must coincide with an angular momentum contour, which implies that the vertical zonal wind shear (i.e., the vertical angular momentum gradient) at the latitude of the streamfunction zero must vanish. Because thermal wind balance in an atmosphere

with approximately moist adiabatic stratification links the vertical zonal wind shear to gradients of near-surface moist static energy [78], the net result is that a vertical zero contour of the mass flux streamfunction generally occurs at the near-surface moist static energy maximum [77]. This is also where thermodynamic arguments suggest precipitation should be favored [34, 79].

Deviations from these leading-order expectations do occur. For example, the zero of the mass flux streamfunction, the energy flux equator, and the ITCZ do not always coincide when the streamfunction is strongly asymmetric about the ITCZ, such as during monsoons, when the cross-equatorial Hadley cell is much stronger than the Hadley cell that is confined to the summer hemisphere [e.g., 2]. However, meridional migrations of the ITCZ have similar magnitude as those of the energy flux equator [e.g., 5, 7, 67], and eddy contributions to derivatives of the meridional energy flux are much smaller than the contribution of the mean meridional circulation [72]. In what follows, we therefore identify the ITCZ with the energy flux equator, where $\langle\overline{vh}\rangle = 0$, and discuss the energetic constraints its position has to satisfy. A detailed study of the extent to which these constraints apply in Earth's atmosphere appears in a companion paper [19].

3.5 Energetic constraints on ITCZ position

Energy fluxes and their meridional structure

In a statistically steady state, the zonal-mean energy balance of atmospheric columns reads [e.g., 34]

$$\partial_y \langle\overline{vh}\rangle = \mathcal{S} - \mathcal{L} - \mathcal{O}, \tag{3.6}$$

which states that the divergence of the meridional moist static energy flux in atmospheric columns (left-hand side) is balanced by the net energy input to the atmosphere (right-hand side, see Fig. 3.6). The net energy input consists of net incoming shortwave radiation $\mathcal{S}$ and outgoing longwave radiation $\mathcal{L}$ at the top of the atmosphere, and any energy uptake $\mathcal{O}$ at the surface. Because the ability of land surfaces to store energy is negligible, the surface energy uptake $\mathcal{O}$ occurs in the oceans. Within the oceans, this energy uptake $\mathcal{O}$ can be balanced by storage, especially on seasonal timescales, and energy flux divergence, which dominates on longer timescales. If the energy balance is not approximately in a statistically steady state, as it is in the simulations on which we focus here, energy storage in atmospheric columns must also be considered, amounting to an additional term $-\partial_t\langle e\rangle$, where $e = c_p T + L_v q$ is the moist enthalpy. This term would have to be added to

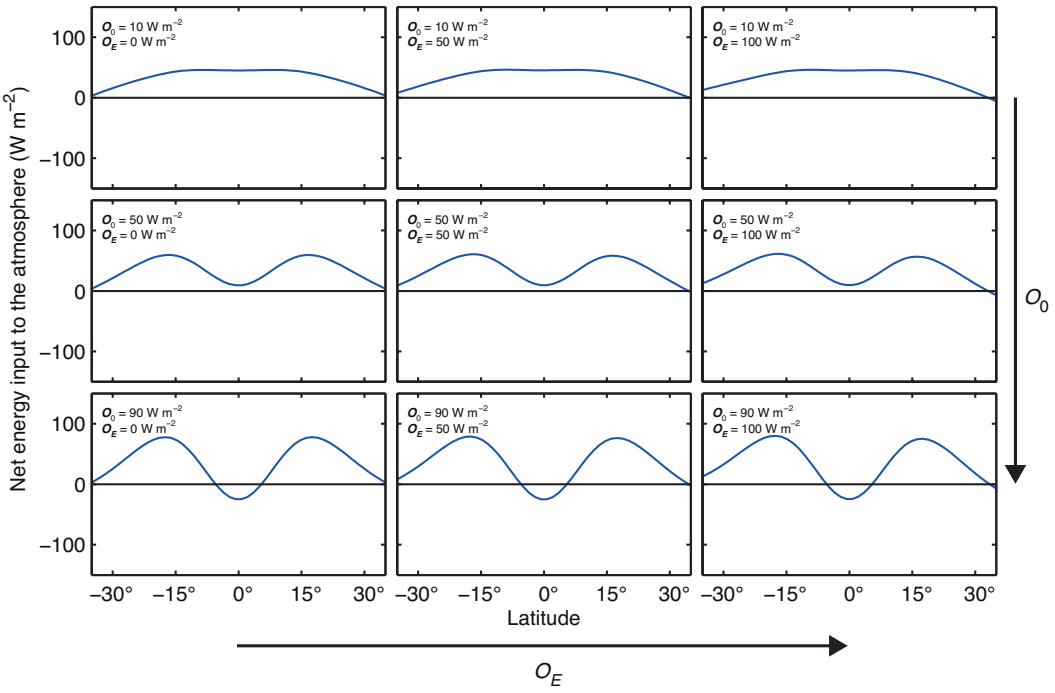

Figure 3.6: Net energy input $\mathcal{S} - \mathcal{L} - \mathcal{O}$ to the tropical atmosphere for the nine simulations with different O_0 and O_E in Figs. 3.4 and 3.5. As the ocean energy flux divergence at the equator, O_0, is increased (going from top to bottom in columns of figure panels), the net energy input to the equatorial atmosphere decreases. At the same time, the meridional curvature of the net energy input at the equator increases. Near the equator, the net energy input remains approximately symmetric about the equator even for strongly hemispheric asymmetric forcing (large O_E).

$\mathcal{S} - \mathcal{L} - \mathcal{O}$ on the right-hand side; our considerations in what follows would remain valid with this modified right-hand side.

The atmospheric energy balance (3.6) implies that the atmosphere transports energy from regions of positive net energy input (e.g., the tropics) to regions of negative net energy input (e.g., the extratropics). As in Bischoff & Schneider [67], we expand the zonal-mean energy flux $\langle\overline{vh}\rangle$ around the equator

$$\langle\overline{vh}\rangle_\phi = \langle\overline{vh}\rangle_0 + a\partial_y\langle\overline{vh}\rangle_0\,\phi + \frac{1}{2}a^2\partial_{yy}\langle\overline{vh}\rangle_0\,\phi^2 + \frac{1}{6}a^3\partial_{yyy}\langle\overline{vh}\rangle_0\,\phi^3 + O(\phi^4), \quad (3.7)$$

with expressions with subscript 0 evaluated at the equator. The equator is a convenient reference point, because in our GCM simulations the quadratic term is negligible compared to the cubic term because $\mathcal{S}$, $\mathcal{L}$, and $\mathcal{O}$ are nearly symmetric about the equator, so that $\partial_{yy}\langle\overline{vh}\rangle_0 = \partial_y\,(\mathcal{S} - \mathcal{L} - \mathcal{O})_0$ is small (see Fig. 3.6). The same is true for Earth's atmosphere in the annual mean: According to the energy

flux data described in Fasullo & Trenberth [35] and Trenberth & Fasullo [71][1], the ratio of the coefficients of the quadratic and cubic terms is small,

$$3\partial_{yy}\langle\overline{vh}\rangle_0 / \left[a\partial_{yyy}\langle\overline{vh}\rangle_0\right] \lesssim 0.02.$$

This implies that for an ITCZ more than ~0.04 rad $\approx 2^\circ$ off the equator, the quadratic term is at least a factor of 2 smaller than the cubic term (and for an ITCZ closer to the equator, both likely are negligible compared to the linear term). The underlying physical reason is that the absorbed solar radiation $\mathcal{S}$ is almost symmetric about the equator in the annual mean, except for the modulation through shortwave scattering by the ITCZ clouds themselves [80]. The outgoing longwave radiation is almost symmetric about the equator, even seasonally, except for the modulation through longwave absorption by the ITCZ clouds and by the enhanced humidity of the atmosphere near the ITCZ. The approximate symmetry of the longwave radiation arises because temperatures in the free troposphere vary approximately symmetrically about the equator, even when the ITCZ is far off the equator and the Hadley circulation is strongly asymmetric [1, 81]. Modulations of $\mathcal{S}$ and $\mathcal{L}$ by the ITCZ clouds largely cancel because the shortwave and longwave effects of deep clouds nearly cancel [80, 82, 83]. Asymmetries in $\mathcal{O}$ are not large enough to offset the near-symmetry of $\mathcal{S} - \mathcal{L}$. Therefore, the quadratic term in the expansion (3.7) may often be negligible, and we neglect it in what follows.

Using the atmospheric energy balance (3.6), we can then rewrite the expansion (3.7) to get, at first order, the linear approximation for the moist static energy flux near the equator used in Bischoff & Schneider [67] and Schneider *et al.* [1],

$$\langle\overline{vh}\rangle_\phi \approx \langle\overline{vh}\rangle_0 + a\,(\mathcal{S} - \mathcal{L} - \mathcal{O})_0\ \phi; \tag{3.8}$$

at third order, we get the cubic approximation without the quadratic term

$$\langle\overline{vh}\rangle_\phi \approx \langle\overline{vh}\rangle_0 + a\,(\mathcal{S} - \mathcal{L} - \mathcal{O})_0\ \phi + \frac{a^3}{6}\partial_{yy}\,(\mathcal{S} - \mathcal{L} - \mathcal{O})_0\ \phi^3. \tag{3.9}$$

These equations relate the moist static energy flux at a latitude ϕ to the cross-equatorial moist static energy flux $\langle\overline{vh}\rangle_0$, the equatorial net energy input $(\mathcal{S} - \mathcal{L} - \mathcal{O})_0$, and its curvature $\partial_{yy}\,(\mathcal{S} - \mathcal{L} - \mathcal{O})_0$. The linear approximation is adequate when $\langle\overline{vh}\rangle_\phi$ varies approximately linearly with latitude around the equator. In what follows, however, we are interested in cases when $\langle\overline{vh}\rangle_\phi$ varies nonlinearly around the

[1] The data are available at https://climatedataguide.ucar.edu/climate-data/era-interim-derived-components

equator, and the cubic term in Eq. (3.9), with the curvature of the equatorial net energy input as coefficient, needs to be taken into account.

Fig. 3.5 illustrates the forms the energy flux $\langle\overline{vh}\rangle_\phi$ near the equator takes in our GCM simulations with varying O_0 and O_E. It also shows the linear (3.8) and cubic (3.9) approximations. For simulations with equatorial ocean energy flux divergence $O_0 < 50$ W m^{-2}, the linear approximation (3.8) captures the energy flux well between $-15°$ and $15°$ latitude. For simulations with equatorial ocean energy flux divergence $O_0 \geq 50$ W m^{-2}, the cubic approximation (3.9) is more accurate and captures the strong nonlinearity around the equator that develops when the ocean energy flux divergence near the equator is large. The cubic term in Eq. (3.9) plays an important role in controlling the ITCZ position, as shown in Fig. 3.5: it determines whether a single or double ITCZ forms.

The flux approximations (3.8) and (3.9) also lend themselves to physical interpretation of how the equatorial atmospheric energy balance impacts the ITCZ position. For example, consider a fixed southward (negative) cross-equatorial energy flux $\langle\overline{vh}\rangle_0$ (columns of Fig. 3.5). If the equatorial net energy input $(\mathcal{S} - \mathcal{L} - O)_0$ to the atmosphere is small, implying a small slope $\partial_y\langle\overline{vh}\rangle_0$ of the energy flux as a function of latitude near the equator, the region of negative energy flux has to extend far into the northern hemisphere, implying an energy flux equator and ITCZ far in the northern hemisphere. Conversely, if the equatorial net energy input to the atmosphere is larger, the region of negative energy flux does not have to extend so far into the northern hemisphere. Similar arguments apply to the curvature term $\partial_{yy}(\mathcal{S} - \mathcal{L} - O)_0$ in the cubic expansion (3.9), which controls the meridional flatness of the equatorial net energy input to the atmosphere as a function of latitude. If the net energy input is flat ($\partial_{yy}(\mathcal{S} - \mathcal{L} - O)_0$ is small and positive), the region of negative energy flux has to extend farther into the northern hemisphere than when it is less flat. In other words, net energy input that is more strongly peaked near the equator favors an ITCZ closer to the equator, as is intuitive. See Fig. 3.6 for some examples of meridional structures of net energy inputs $\mathcal{S} - \mathcal{L} - O$ in our simulations.

In what follows, we group the simulations into three categories depending on the relative importance of the terms in the cubic expansion (3.9).

Strong positive equatorial net energy input

If the equatorial net energy input $(\mathcal{S} - \mathcal{L} - O)_0$ to the atmosphere is large and positive, its curvature near the equator can be neglected, and the linear approximation (3.8) for

the energy flux near the equator is adequate. In our simulations, this is the case when

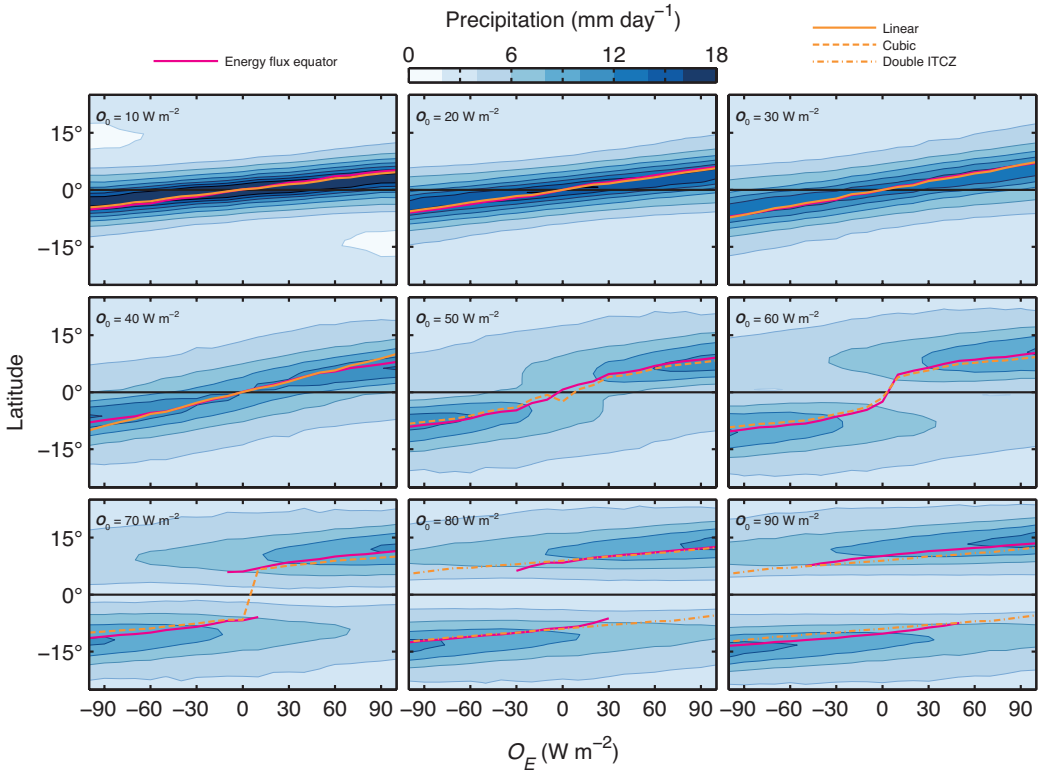

Figure 3.7: Precipitation rate in all 121 simulations, for different values of the extratropical ocean energy flux divergence (O_E, horizontal axes) at fixed values of the ocean energy flux divergence at the equator (O_0, increasing from top left to bottom right panel). Magenta lines show the energy flux equator, where $\langle \overline{vh} \rangle = 0$. The ITCZ latitude depends approximately linearly on O_E for $O_0 \lesssim 50$ W m^{-2}. For $O_0 \gtrsim 50$ W m^{-2}, the ITCZ latitude depends nonlinearly on O_E, as can be understood from the nonlinear dependence of $\langle \overline{vh} \rangle$ on latitude (Fig. 3.5). Orange lines show the approximations for the energy flux equator from Eq (3.10) (linear, solid), Eq. (3.11) (cubic, dashed), and Eq. (3.13) (double ITCZ, dashed-dotted). Only simulations with positive O_E were performed, and the data points are mirrored about $O_E = 0$.

the ocean energy flux divergence is sufficiently weak, $O_0 \lesssim 50$ W m^{-2} (Fig. 3.5, top row). Identifying the ITCZ with the energy flux equator where $\langle \overline{vh} \rangle = 0$, denoting its latitude by δ, and solving (3.8) for δ gives

$$\delta \approx -\frac{\langle \overline{vh} \rangle_0}{a\,(\mathcal{S} - \mathcal{L} - \mathcal{O})_0}. \tag{3.10}$$

In this case, the ITCZ latitude is anticorrelated with the cross-equatorial energy flux. The resulting approximate ITCZ latitude δ captures the variation of the actual ITCZ

latitude with the amplitude O_E of the extratropical ocean energy flux divergence in our simulations for $O_0 \lesssim 50$ W m^{-2} (Fig. 3.7). The sensitivity of the ITCZ position to O_E and thus to the cross-equatorial energy flux $\langle\overline{vh}\rangle_0$ (which is controlled by O_E) increases as O_0 increases and therefore $(\mathcal{S} - \mathcal{L} - \mathcal{O})_0$ decreases, in good agreement with the linear approximation (3.10). This also illustrates that ITCZ shifts can arise when $(\mathcal{S} - \mathcal{L} - \mathcal{O})_0$ changes, independently of changes in the cross-equatorial energy flux $\langle\overline{vh}\rangle_0$.

Weak positive equatorial net energy input

A slightly more complicated situation arises when the cubic term in the expansion of the energy flux (3.9) approximately balances the zeroth-order term, the cross-equatorial energy flux $\langle\overline{vh}\rangle_0$. In this case, the equatorial net energy input to the atmosphere is small compared to the other terms in Eq. (3.9), and one can solve for δ perturbatively using an asymptotic expansion (see Appendix B for details). This leads to an approximation for the energy flux equator δ that is, at leading order, given by

$$\delta \approx \frac{1}{a}\left(\frac{-6\langle\overline{vh}\rangle_0}{\partial_{yy}\,(\mathcal{S} - \mathcal{L} - \mathcal{O})_0}\right)^{\frac{1}{3}} - \frac{2\,(\mathcal{S} - \mathcal{L} - \mathcal{O})_0}{a\partial_{yy}\,(\mathcal{S} - \mathcal{L} - \mathcal{O})_0}\left(\frac{-6\langle\overline{vh}\rangle_0}{\partial_{yy}\,(\mathcal{S} - \mathcal{L} - \mathcal{O})_0}\right)^{-\frac{1}{3}}. \quad (3.11)$$

This approximation is only valid for nonzero $\langle\overline{vh}\rangle_0$. In the special case of $(\mathcal{S} - \mathcal{L} - \mathcal{O})_0 = 0$, it reduces to the scaling

$$\delta \propto \left[-\langle\overline{vh}\rangle_0\right]^{\frac{1}{3}}, \quad (3.12)$$

that is, a weaker dependence of ITCZ latitude on the cross-equatorial energy flux than under the linear approximation.

The approximation (3.11) captures the behavior of the ITCZ in our simulations with 40 W m^{-2} $< O_0 <$ 70 W m^{-2} (Fig. 3.7). In these simulations, the equatorial net energy input is small, $(\mathcal{S} - \mathcal{L} - \mathcal{O})_0 \lesssim 10$ W m^{-2}, and the linear approximation performs poorly when O_E and the cross-equatorial energy flux $\langle\overline{vh}\rangle_0$ are sufficiently large (Fig. 3.5, middle row).

These results indicate that the ITCZ position does not necessarily vary linearly with $\langle\overline{vh}\rangle_0$ under all circumstances, as was assumed in several previous studies [e.g., 2, 20]. Instead, nonlinear scalings can be more appropriate. The value of the equatorial net energy input to the atmosphere (around 10 W m^{-2}) where the linear approximation performs poorly in our simulations happens to be close to the corresponding value for Earth in the annual mean ([35], their Fig. 3; [1, 72]).

Negative equatorial net energy input

When the equatorial net energy input to the atmosphere $(\mathcal{S} - \mathcal{L} - O)_0$ is negative, the energy flux is no longer monotonically increasing with latitude, and two energy flux equators—a double ITCZ—can form on either side of the equator (Fig. 3.5, bottom row). Two energy flux equators can also form when the curvature $\partial_{yy} (\mathcal{S} - \mathcal{L} - O)_0$ becomes negative; however, ocean energy flux divergence near the equator prevents that from occuring in our simulations. When two off-equatorial energy flux equators form, the atmosphere transports energy toward the equator, away from the two off-equatorial ITCZs. When, additionally, the cubic term in the expansion (3.9) approximately balances the linear term, while the cross-equatorial energy flux $\langle\overline{vh}\rangle_0$ introduces only a small correction, we can solve for the two latitudes δ of the energy flux equators using an asymptotic expansion (see Appendix B), leading to

$$\delta \approx \pm\frac{1}{a}\left(-\frac{6\,(\mathcal{S} - \mathcal{L} - O)_0}{\partial_{yy}\,(\mathcal{S} - \mathcal{L} - O)_0}\right)^{\frac{1}{2}} + \frac{\langle\overline{vh}\rangle_0}{2a\,(\mathcal{S} - \mathcal{L} - O)_0}. \tag{3.13}$$

This is valid for small cross-equatorial energy flux $\langle\overline{vh}\rangle_0$, that is, small asymmetries of the two ITCZs around the equator.

The double-ITCZ approximation (3.13) captures the ITCZs in our simulations with $O_0 > 70$ W m^{-2} (Fig. 3.7). The position of the two distinct convergence zones north and south of the equator vary linearly with O_E or $\langle\overline{vh}\rangle_0$—provided the cross-equatorial energy flux is weak enough (for $\langle\overline{vh}\rangle_0 \lesssim 0.3$ PW in our simulations). For stronger cross-equatorial energy fluxes $\langle\overline{vh}\rangle_0$, all terms in the cubic expansion (3.9) are important, and δ is most conveniently calculated numerically.

Fig. 3.8 shows the bifurcation from single to double ITCZs for different values of O_E. The bifurcation is most obvious for small O_E, where it occurs for an equatorial ocean energy flux divergence $O_0 \approx 50$ W m^{-2}: If O_0 exceeds this value, the equatorial net energy input to the atmosphere $(\mathcal{S} - \mathcal{L} - O)_0$ becomes negative in our simulations, and a double ITCZ forms. As it happens, Earth's ocean energy uptake at the equator is close to the value at which the bifurcation occurs in our simulations: It amounts to about $O_0 \approx 54$ W m^{-2} in the annual mean according to the data in Fasullo & Trenberth [35, their Fig. 3] and Loeb *et al.* [83].

Relating cross-equatorial energy flux to amplitude of extratropical forcing

The results so far relate the ITCZ position to the atmospheric energy balance near the equator. In that sense, they are diagnostic, because the atmospheric energy balance

in itself depends on the atmospheric circulation near the equator and thus on the ITCZ position. In our simulations, because the cross-equatorial energy flux depends primarily and approximately linearly on the amplitude of the imposed extratropical ocean energy flux divergence (Fig. 3.3), we can go a step further and express the cross-equatorial energy flux as a function of the extratropical forcing parameter O_E,

$$\langle \overline{vh} \rangle_0 = \gamma O_E. \tag{3.14}$$

Here, $\gamma \approx 1.92 \times 10^5$ m is an empirical parameter determined from a fit to the simulation with $O_0 = 50$ W m^{-2} and $O_E = 100$ W m^{-2}. The closure (3.14) can be justified by linearly relating the high-latitude temperature difference between the hemispheres to the extratropical forcing amplitude O_E, and using a diffusive energy flux closure for extratropical eddies [e.g., 67]. Alternatively, one can use an energy

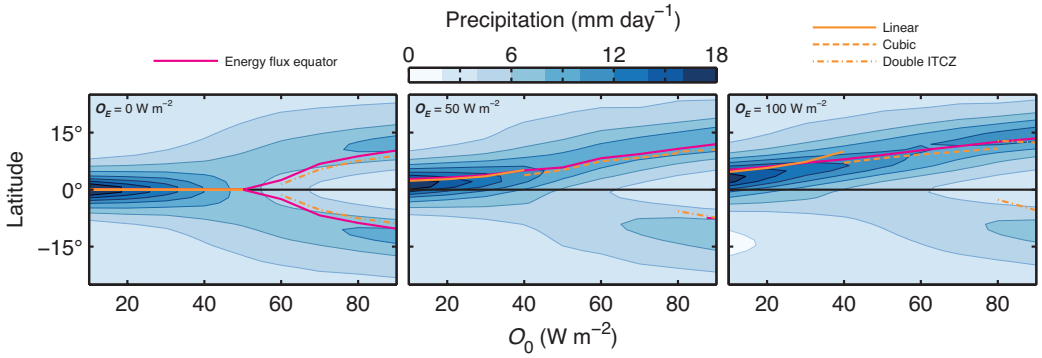

Figure 3.8: Precipitation rate as in Fig. 3.7, but now as a function of the equatorial ocean energy flux divergence (O_0, horizontal axis) at fixed values of the extratropical ocean energy flux divergence O_E. Magenta lines show the energy flux equator, where $\langle \overline{vh} \rangle = 0$. The ITCZ latitude depends nonlinearly on O_0 for all values of O_E. For $O_0 \gtrsim 50$ W m^{-2}, the ITCZ bifurcates from a single- to a double-ITCZ state. Orange lines show the approximations for the energy flux equator from Eq (3.10) (linear, solid), Eq. (3.11) (cubic, dashed), and Eq. (3.13) (double ITCZ, dashed-dotted). The lines shown are the same as in Fig. 3.7 and correspond to the approximations that are most appropriate for the respective simulations; equation (3.10) for simulations with $O_0 \leq 50$ W m^{-2}, equation (3.11) for simulations with $50 < O_0 \leq 80$ W m^{-2}, and equation (3.13) for simulations with $80 < O_0$ W m^{-2}.

transport efficiency parameter as in Kang *et al.* [5, 6] to justify the closure (3.14). In either case, the extratropical forcing impacts the tropical circulation through the mediation by extratropical eddies that transport heat and moisture from the subtropics to the extratropics, and the parameter γ indicates the strength of the coupling between the extratropical forcing amplitude O_E and the tropical circulation.

Combining the closure (3.14) with the approximations (3.10), (3.11), or (3.13) for the ITCZ latitude, we arrive at expressions for δ that depend only on the forcing parameters O_0 and O_E if changes in $\mathcal{S}$ and $\mathcal{L}$ are neglected. If we fix $\mathcal{S}$ and $\mathcal{L}$ as functions of latitude to those in the simulation with $O_0 = 50.0$ W m^{-2} and $O_E = 0$ W m^{-2}, we obtain the approximate values $\hat{\delta}$ listed in the last column of Table 3.1. These approximate ITCZ positions $\hat{\delta}$ obtained solely from the external forcing parameters O_E and O_0, using the fixed fitting parameter γ and fixed functions $\mathcal{S}$ and $\mathcal{L}$, agree within $\lesssim 1^\circ$ with the values of δ obtained diagnostically from the energy balance in the simulations.

This closure approach is successful in our simulations because the cross-equatorial energy flux is almost entirely determined by the amplitude of the imposed, hemispherically antisymmetric but zonally symmetric, extratropical energetic forcing. However, it will be less successful in more realistic settings when, for example, zonally asymmetric extratropical ocean energy flux divergences, which may have only a small or no projection on the zonal mean, generate stationary waves that lead to modulations of the cross-equatorial energy flux [1]. In that latter case, more sophisticated closures for the extratropical energy transport, taking stationary eddies into account, need to be used in expressions for the cross-equatorial energy flux [67].

3.6 Discussion and conclusions

Summary

To study how the ITCZ depends on the energy balance near the equator, we varied the strength of the cross-equatorial atmospheric energy flux and the energy input to the equatorial atmosphere over wide ranges by perturbing an ocean energy flux divergence imposed at the lower boundary of an idealized aquaplanet GCM. As in previous studies with idealized GCMs [e.g., 5, 6], we find that the latitude of the ITCZ and of the energy flux equator coincide approximately. This remains true when two zeros of the atmospheric energy flux straddle the equator, leading to a double ITCZ.

The energy flux equator and ITCZ position are determined by how the atmospheric energy flux $\langle \overline{vh} \rangle$ varies with latitude around the equator. If the variations are approximately linear with latitude, the ITCZ displacement off the equator, δ, is proportional to the cross-equatorial energy flux $\langle \overline{vh} \rangle_0$ and inversely proportional to its divergence, the net energy input to the equatorial atmosphere $(\mathcal{S} - \mathcal{L} - \mathcal{O})_0$. If higher-order terms need to be considered in a Taylor expansion of the energy flux

O_E (W m^{-2})	O_0 (W m^{-2})	$\phi_{P_{\max}}$ (°)	$\phi_{\Psi_{\max}=0}$ (°)	$\phi_{\overline{\langle vh\rangle}=0}$ (°)	δ (°)	$\hat{\delta}$ (°)
0	10	0.0	0.0	0.1	0.1	0.0
0	50	0.0	0.0	0.7	–	–
0	90	± 12.0	±11.0	±10.2	± 8.9	±9.9
50	10	1.4	2.4	2.8	2.3	1.8
50	50	6.0	7.0	5.8	5.2	5.8
50	90	13.1	13.5	11.9	10.0 (-8.0)	10.8 (-8.9)
100	10	3.0	4.9	5.2	4.6	3.5
100	50	7.4	10.5	9.1	8.3	8.3
100	90	14.5	15.5	13.5	11.2 (-6.6)	11.7 (-8.0)

Table 3.1: Summary of various measures of the ITCZ position for the nine simulations shown in Fig. 3.4. Here, $\phi_{P_{\max}}$ denotes the latitude of the precipitation maximum between $-20°$ and $20°$, $\phi_{\Psi_{\max}=0}$ denotes the latitude of the zero of the mass flux streamfunction at the level of its maximum between $-20°$ and $20°$, $\phi_{\overline{\langle vh\rangle}=0}$ denotes the latitude of the energy flux equator between $-20°$ and $20°$, δ has its usual meaning from the text, and $\hat{\delta}$ is the approximation obtained with the closure (3.14) with the $\mathcal{S}$ and $\mathcal{L}$ fixed to those in the simulation with $O_0 = 50.0$ W m^{-2} and $O_E = 0$ W m^{-2}. Where applicable, the values in parentheses show the second solution according to the double-ITCZ approximation (3.13).

around the equator, and if the second-order term can be neglected (as is the case in the idealized GCM and in the annual mean on Earth), more complicated situations can arise. If $(\mathcal{S}-\mathcal{L}-O)_0$ is small but positive, the dependence of the ITCZ position δ on $\langle\overline{vh}\rangle_0$ weakens to the third root. If $(\mathcal{S}-\mathcal{L}-O)_0$ becomes negative, or if its curvature $\partial_{yy}(\mathcal{S}-\mathcal{L}-O)_0$ becomes negative, a bifurcation to double-ITCZ states occurs. The ITCZ positions δ then not only depend on $\langle\overline{vh}\rangle_0$ and $(\mathcal{S}-\mathcal{L}-O)_0$, but also on the curvature $\partial_{yy}(\mathcal{S}-\mathcal{L}-O)_0$ near the equator.

We have demonstrated the quantitative adequacy of these relations in the idealized GCM simulations, which have a statistically stationary and zonally symmetric climate. Previous studies using observations and more comprehensive climate models have documented relations between the ITCZ position and the atmospheric energy flux [e.g., 2, 4, 20, 29, 33]. This suggest that our results may apply to Earth's atmosphere, at least in the zonal and long-term mean. A detailed study of their applicability to seasonal and interannual variations of the ITCZ appears in a companion paper [19]. Several broader implications for the interpretation of climate records and climate modeling can already be seen.

Implications for interpreting climate records

Our results provide a framework within which a broad range of ITCZ variations can be interpreted and previous results can be re-contextualized. For example, paleoclimatological evidence and observations suggest that the ITCZ has migrated meridionally in the past, and that it may do so again in the future in response to anthropogenic climate changes [e.g., 1, 3, 31, 33, 61, 84–88]. Often such ITCZ migrations are interpreted in terms of changes in cross-equatorial atmospheric energy fluxes, triggered, for example, by changes in the albedo of one hemisphere that may be caused by changes in glaciation or aerosol loadings. Our results show that the ITCZ position does not only depend on the cross-equatorial energy flux and factors that may influence it, such as the interhemispheric temperature contrast [e.g., 3, 7]. The ITCZ position is also controlled by the equatorial net energy input and, especially if that is small or negative, by its higher derivatives with respect to latitude. The latter can modulate the sensitivity of the ITCZ to changes in the cross-equatorial atmospheric energy flux. This may account, for example, for the double ITCZ that arises during spring in the eastern Pacific (Fig. 3.1), which collapses to a single ITCZ south of the equator during El Niño [64, 65]. Consistent with our analysis, the equatorial net energy input to the atmosphere in the eastern Pacific is usually negative [71] but becomes positive during strong El Niños [19], when even the South Pacific Convergence Zone—an extreme double ITCZ—can collapse onto the equator [89, 90].

Stated generally, a linear relation between the ITCZ position and the cross-equatorial atmospheric energy flux cannot usually be expected. Dependencies of the ITCZ position on the equatorial net energy input to the atmosphere and its derivatives should be examined.

Implications for climate modeling

The ITCZ position depends on the equatorial net energy input to the atmosphere, $(\mathcal{S} - \mathcal{L} - \mathcal{O})_0$, which is a small residual of large terms [1]: For Earth in the annual and zonal mean, the net incoming shortwave radiation is about $\mathcal{S}_0 = 323$ W m^{-2}; the outgoing longwave radiation is about $\mathcal{L}_0 = 251$ W m^{-2}; the ocean energy uptake is about $\mathcal{O}_0 = 54$ W m^{-2}, leaving the relatively small residual $(\mathcal{S} - \mathcal{L} - \mathcal{O})_0 \approx 18$ W m^{-2}. This alone makes the ITCZ position sensitive to small biases in climate models' energy balances, such as may occur through biases in cloud shortwave and longwave effects. Beyond that, our results show that the ITCZ position can also depend, for example, on the curvature of $(\mathcal{S} - \mathcal{L} - \mathcal{O})$ as a function of latitude.

This makes the ITCZ position sensitive, for example, to biases in the sharpness of equatorial ocean upwelling, and likely leads to a dependence of the ITCZ position on model resolution.

For example, Earth's ITCZ appears to be close to the boundary at which $(\mathcal{S}-\mathcal{L}-\mathcal{O})$ becomes negative and the bifurcation to a double-ITCZ state occurs. Relatively small biases in the energy balance may thus lead to the well known double ITCZ bias of climate models [9]. Extratropical model biases likely contribute to this tropical bias [e.g., 66]. But tropical biases, for example, in cloud radiative effects [e.g., 6, 91, 92] or ocean energy uptake, may also play a role, with cloud feedbacks being especially important. Consistent with our framework, the double-ITCZ bias in climate models appears to be related to a cool bias of equatorial sea surface temperatures [93, 94], suggesting a low bias of the equatorial net energy input to the atmosphere. Because the equatorial net energy input to the atmosphere depends on the ocean energy uptake, climate models with a fixed ocean energy transport, or with fixed sea surface temperatures, can give a different structure of the ITCZ and how it changes with climate than models with interactive ocean energy transport [94].

An analysis of climate model biases within the framework we presented here promises to be a fruitful avenue of research. This may help identify the causes of the biases.

Open questions

Relating the energy flux equator and ITCZ position in greater detail and generality than has been done previously to the energy balance of the atmosphere represents progress. Nonetheless, the energy balance is merely one identity the atmosphere has to satisfy; a Taylor expansion of it around the equator provides diagnostic relations for the ITCZ position but does not represent a closed dynamical theory [1]. The quantities entering the energy balance themselves depend on the atmospheric circulation and thus on the ITCZ position. For example, the net energy input depends on the atmospheric circulations responsible for the energy transport and its divergence, which in turn depend on where the ITCZ is located [e.g., 79, 81, 95–100]. A closed theory of the ITCZ must, for example, also take the angular momentum balance into account, both near the surface [e.g., 99, 101, 102] and in the free troposphere [e.g., 44]. The angular momentum balance in part controls the mean meridional mass flux $\Psi_{\max}$ [e.g., 63], which together with the gross moist

stability enters the energy balance through the relation (3.5) between mass fluxes and energy fluxes. The angular momentum balance controlling the mean meridional mass flux in turn depends on eddy fluxes of angular momentum [62], which thus also can affect the ITCZ position through the energy transport associated with the mean meridional circulation. However, such dependencies are only implicit if one focuses on the energy balance alone. How the constraints from the energy balance and angular momentum balance are to be coupled in a closed theory is a largely unresolved question.

In addition to such unresolved questions, the ITCZ on Earth is not zonally symmetric, so that a local theory for an ITCZ position that depends on longitude is needed. This may be accomplished by including zonal moist static energy fluxes in versions of the energy balance (3.6) averaged over finite longitudinal sectors.

Also appearing in the relation (3.5) between mass fluxes and energy fluxes is the gross moist stability [34, 76]. For the gross moist stability, likewise no closed and generally adequate theory exists yet [103]. Additionally, the ITCZ is not always co-located with the energy flux equator. Resolving these outstanding questions remains as a challenge to dynamicists.

3.7 Appendix A: Relating energy, moisture, and mass transports

The column-integrated moisture flux associated with the mean meridional circulation in a statistically steady state can be approximated as

$$\langle \overline{v}\,\overline{q} \rangle = \int_0^{p_s} \mathcal{H}(\overline{v})\overline{v}\,\overline{q}\,\frac{dp}{g} + \int_0^{p_s} \mathcal{H}(-\overline{v})\overline{v}\,\overline{q}\,\frac{dp}{g} \tag{3.15a}$$

$$\approx q_t \int_0^{p(\overline{v}=0)} \overline{v}\,\frac{dp}{g} + q_s \int_{p(\overline{v}=0)}^{p_s} \overline{v}\,\frac{dp}{g} \tag{3.15b}$$

$$= (q_t - q_s) \int_0^{p(\overline{v}=0)} \overline{v}\,\frac{dp}{g} \tag{3.15c}$$

$$\approx -\frac{q_s \Psi_{\max}(\phi)}{2\pi a \cos(\phi)}. \tag{3.15d}$$

Here, we have used the mean value theorem for integrals to go from the first to the second line, q_s and q_t are representative specific humidities in the lower branch and upper branch of the overturning circulation (divided at the level at which the mean meridional flow vanishes), and $\mathcal{H}$ denotes the Heaviside function. Mass conservation in atmospheric columns was used in going from the second to the third line. And because the specific humidity in the upper branch is much lower than that

in the lower branch, $q_t \ll q_s$, the final approximate equality follows, with the mass flux streamfunction $\Psi(p, \phi) = 2\pi a \cos(\phi) \int_0^p \overline{v}\, dp/g$.

Similarly, the column-integrated energy flux associated with the mean meridional circulation can be approximated as

$$\langle \overline{v}\, \overline{h} \rangle = \int_0^{p_s} \mathcal{H}(\overline{v}) \overline{v}\, \overline{h}\, \frac{dp}{g} + \int_0^{p_s} \mathcal{H}(-\overline{v}) \overline{v}\, \overline{h}\, \frac{dp}{g} \tag{3.16a}$$

$$\approx \frac{(h_t - h_s)\Psi_{\max}(\phi)}{2\pi a \cos(\phi)} \tag{3.16b}$$

$$\approx \frac{\Delta h \Psi_{\max}(\phi)}{2\pi a \cos(\phi)}, \tag{3.16c}$$

where $\Delta h = h_t - h_s$ is a gross moist stability [34, 76].

3.8 Appendix B: Asymptotic approximation for the ITCZ position

Section 4 presented asymptotic approximations to the ITCZ position, which were approximate roots δ of a third-order polynomial of the form

$$0 = A + B\delta + C\delta^3, \tag{3.17}$$

where $A = \langle \overline{vh} \rangle_0$, $B = a\partial_y \langle \overline{vh} \rangle_0$, and $C = \frac{1}{6} a^3 \partial_{yyy} \langle \overline{vh} \rangle_0$. If $C = 0$, then equation (3.17) can be solved straightforwardly by

$$\delta = -\frac{A}{B}, \tag{3.18}$$

corresponding to approximation (3.10) for strong positive equatorial net energy input.

For weak positive equatorial net energy input (small B), when the cubic term in the expansion of the energy flux (3.9) approximately balances the constant term, we can expand δ in a power series in B

$$\delta = \delta_0 + \delta_1 B + \dots. \tag{3.19}$$

Inserting this series for δ into equation (3.17) gives at zeroth order

$$0 = A + C\delta_0^3 \quad \Rightarrow \quad \delta_0 = \left(-\frac{A}{C} \right)^{1/3}, \tag{3.20}$$

and at first order

$$0 = B\delta_0 + 3C\delta_0^2 B\delta_1 \quad \Rightarrow \quad \delta_1 = -\frac{1}{3C\delta_0}. \tag{3.21}$$

If $A \neq 0, C \neq 0$, the perturbation expansion for δ is then given by

$$\delta \approx \delta_0 \left(1 + \frac{\delta_1}{\delta_0} B\right) = \left(-\frac{A}{C}\right)^{1/3} \left[1 - \frac{1}{3}\frac{B}{C}\left(-\frac{C}{A}\right)^{2/3}\right], \tag{3.22}$$

which corresponds to the approximation (3.11).

For negative equatorial net energy input and when A is small, the cubic term in the expansion of the energy flux (3.9) approximately balances the linear term, and we can expand δ in a power series in A

$$\delta = \delta_0 + \delta_1 A + \ldots. \tag{3.23}$$

Inserting this series for δ into equation (3.17) gives at zeroth order

$$0 = \left(B + C\delta_0^2\right)\delta_0 \quad \Rightarrow \quad \delta_0 = 0 \quad \text{or} \quad \delta_0 = \pm\left(-\frac{B}{C}\right)^{1/2}, \tag{3.24}$$

and at first order ($\delta_0 \neq 0$)

$$0 = A + \delta_1 AB + 3C\delta_0^2 A\delta_1 \quad \Rightarrow \quad \delta_1 = -\frac{1}{B + 3C\delta_0^2} = \frac{1}{2B}. \tag{3.25}$$

If $B \neq 0, C \neq 0$, the perturbation expansion for δ is then given by

$$\delta \approx \pm\left(-\frac{B}{C}\right)^{1/2} + \frac{A}{2B}, \tag{3.26}$$

which corresponds to the approximation (3.13).

Chapter 4

ORBITAL VARIATIONS OF TROPICAL RAINFALL FROM AN IDEALIZED PRECIPITATION MODEL

4.1 Abstract

Tropical rainfall to first order responds to variations in Earth's orbit through shifts of the Intertropical Convergence Zone (ITCZ) and changes in zonally averaged rainfall intensity. Here, a conceptual model is developed that represents both processes and their response to orbital insolation variations. The model predicts the seasonal evolution of tropical rainfall between 30°S and 30°N. Insolation variations impact seasonal rainfall in two different ways: thermodynamically, leading to variations in rainfall intensity through modulation of the water vapor content of the atmosphere; and dynamically, leading to shifts of the ITCZ through modulation of the global atmospheric energy budget. Thermodynamic and dynamic effects act together to shape the annual-mean response of tropical rainfall to changes in Earth's orbit. The model successfully reproduces changes in annual-mean rainfall inferred from paleo-proxies across several glacial-interglacial cycles. It illuminates how orbital precession and variations of Earth's obliquity affect tropical rainfall differently near the equator and farther away from it, with spectral signatures of precession and obliquity variations that shift with latitude. It also provides explanations for the observed different phasings of rainfall minima and maxima near the equator and away from it. For example, the model reproduces a phase shift of ~10 ka between rainfall records from caves in Northern Borneo (4°N) and from China (approximately 30°N). The model suggests that such phase shifts arise through a different weighting of ITCZ shifts and variations in rainfall intensity, thus providing insight into the mechanisms that drive tropical rainfall changes on orbital time scales.

4.2 Introduction

The interpretation of paleoclimatological precipitation records from sediment cores or stalagmites is a difficult task. Not only does their interpretation depend on complex isotopic fractionation processes, among other things. Understanding how any inferred precipitation variations arise mechanistically also remains a challenge. The amount of precipitation that falls at a given location depends on the water vapor content of the atmosphere and the strength of the atmospheric circulations

that transport this water vapor to the location [e.g., 69, 104, 105]. The water vapor content of the atmosphere can change thermodynamically, primarily through temperature-dependent changes in saturation vapor pressure [44, 51]. Atmospheric circulations can change dynamically, for example, by shifting or changing their strength. Any model that attempts to capture how precipitation variations arise, for example, on the time scales of variations in Earth's orbit, must therefore include a representation of the salient thermodynamical and dynamical processes.

Previously, variations of tropical precipitation on orbital time scales have often been related to variations in local or high-latitude insolation induced by orbital variations [e.g., 16, 17], based on the idea that local insolation directly impacts precipitation at a given site. For example, precipitation variations on precessional timescales in Brazil and China are out of phase because summer insolation in the northern hemisphere is more intense when perihelion occurs in boreal summer, causing strengthened monsoon precipitation over Asia, while summer insolation in the southern hemisphere then is reduced, causing weaker monsoon precipitation over Brazil [e.g., 12, 16, 69]. This leads to out-of-phase precipitation variations on precessional timescales in the northern and southern subtropics.

In this paper, we present a conceptual model that captures how tropical precipitation and its seasonal cycle in the zonal mean respond thermodynamically and dynamically to insolation variations. The model is based on the assumption that tropical precipitation changes primarily (i) because precipitation intensity changes thermodynamically in response to tropical insolation variations, which modulate the water vapor content of the atmosphere, and (ii) because the precipitation field as a whole shifts dynamically in latitude, in response to differential global insolation variations that can shift the Intertropical Convergence Zone (ITCZ). The model allows for these two types of changes through a precipitation intensity factor, which is controlled locally by tropical insolation, and through a shape function for the distribution of precipitation with latitude, which encodes the ITCZ latitude and width and depends on the insolation distribution globally.

Previous modeling studies have focused on general circulation model (GCM) simulations that either compare two different climate scenarios (e.g., high vs. low obliquity or June vs. December perihelion) or use accelerated orbital variations to study the seasonality of tropical precipitation [e.g., 69, 104, 106–112]. The main benefit of these models lies in the fact that they can incorporate realistic continental boundary conditions and clouds, among other things. Complexity, however, comes

at a cost in analytic tractability and computational speed. The main virtue of our conceptual model is that it can be analyzed analytically and that it can be simulated at low computational cost, allowing us to illuminate mechanisms of zonal-mean tropical precipitation variations such as those that have been inferred from paleo-records. We use the model to reproduce annual-mean precipitation variations over the past 350 ka that have been inferred from paleo-records at different latitudes, shedding light on various features of the inferred precipitation variations, such as their phase-relation between different latitudes. For example, precipitation variations inferred from caves in northern Borneo at approximately 4° N [13, 15, 18] are phase-shifted by around 10 ka relative to precipitation variations inferred from the Hulu, Sanbao, and Linzhu Caves in China at around 30° N [11, 14, 113]. Our conceptual model provides an explanation of how such phase shifts can arise as a result of the different relative importance of orbital ITCZ shifts and rainfall intensity changes at different latitudes.

Section 4.3 lays out the details of the precipitation model. Section 4.4 discusses how different orbital variations (e.g., precession and obliquity variations) affect precipitation in the model and compares our model hindcasts with low-latitude precipitation records spanning the past 350 ka. Section 4.5 summarizes the results. The appendix provides analytical calculations that help interpretation of the causes of precipitation changes. For example, we show that in the limit of a narrow ITCZ, the annual-mean precipitation at any tropical latitude can be expressed as the product of an ITCZ migration time scale and the precipitation intensity when the ITCZ is overhead. Differences between locations near the equator and subtropical sites arises because near the equator the ITCZ crosses overhead twice a year.

4.3 Model

The zonal-mean precipitation model uses top-of-atmosphere insolation as the only input. This requires simplifying assumptions (e.g., about cloud feedbacks) but leads to a conceptual model that illuminates mechanisms. Our goal is to incorporate just enough complexity to be able to understand orbital changes of precipitation in the zonal mean as they are captured in paleoclimatoglogical precipitation records for the tropics [e.g., 11–18, 26].

Previously, theoretical analyses of paleoclimatological precipitation records for the tropics have resorted to arguments that invoke insolation at a specific time of year at or near the location where the precipitation record is taken, the idea being that

local insolation variations drive precipitation variations at the time when the ITCZ is located at or near the record's site, for example, through the influence of insolation on atmospheric water vapor content or circulation strength [e.g., 11, 14, 16]. One problem with this approach is that insolation at the time when the ITCZ is overhead is not the only important factor to consider when one wants to understand annual-mean precipitation at a given location. For example, high-latitude insolation changes can impact the ITCZ location and the timing of ITCZ passage through the global energy balance of the atmosphere [e.g., 1–3, 5, 6]. Thus, insolation variations across the globe, including at remote locations, can impact annual-mean precipitation at tropical locations.

Here, we adopt a different perspective with a simple nonlinear precipitation model that uses insolation globally as input and represents both thermodynamic and dynamic factors. In the model, the zonal-mean precipitation field is represented as

$$P(\phi, \lambda, T) = e^{\log[P(\phi,\lambda,T)]} = e^{f(\phi,\lambda,T)}, \tag{4.1}$$

where ϕ denotes latitude, λ is solar longitude (see appendix 4.7), T is geological time (kiloyear before present), and $f(\phi, \lambda, T) = \log[P(\phi, \lambda, T)]$ encodes how precipitation varies with latitude (ϕ), time of year (expressed by solar longitude λ), and geological time (T). The geological time T encapsulates all information about the state of Earth's orbit, which is characterized by the orbital parameters longitude of perihelion ϖ, eccentricity e, and obliquity γ. By expanding $f(\phi, \lambda, T)$ to second order around the latitude of maximum tropical precipitation ϕ_m, where the ITCZ is located, and neglecting higher-order contributions, the zonal-mean precipitation field can approximately be written as the Gaussian

$$P(\phi, \lambda, T) \approx P(\phi_m, \lambda, T) e^{-\frac{1}{2\sigma^2}(\phi-\phi_m)^2} \tag{4.2a}$$

$$= \mathcal{M} \times \mathcal{S}. \tag{4.2b}$$

We take the variance $\sigma^2 = -(\partial_{\phi\phi} f(\phi, \lambda, T)|_{\phi=\phi_m})^{-1}$ of the precipitation distribution with latitude to be constant for all values of λ and T. This amounts to assuming that the width of the ITCZ is fixed over seasonal and orbital cycles, which is not entirely accurate [114] but is a useful first approximation. With these assumptions, the zonal-mean precipitation field (4.2) can be decomposed into an intensity factor $\mathcal{M} \equiv P(\phi_m, \lambda, T)$ and a Gaussian shape factor $\mathcal{S} \equiv \exp\left[-(\phi - \phi_m)^2/(2\sigma^2)\right]$. They depend on the ITCZ latitude ϕ_m, which varies on seasonal and geological timescales, and on the variance of the precipitation distribution σ^2 with latitude. Changes in

precipitation $\Delta P = P - P_{\text{ref}}$ relative to a reference distribution P_{ref} as the orbital configuration (T) varies can now be attributed to changes in intensity $\mathcal{M}$ and shape $\mathcal{S}$ via the approximation (neglecting products of intensity changes and ITCZ shifts)

$$\Delta P \approx \underbrace{\Delta\mathcal{M} \times \mathcal{S}_{\text{ref}}}_{\text{intensity changes}} + \underbrace{\mathcal{M}_{\text{ref}} \times \Delta\mathcal{S}}_{\text{ITCZ shifts}}. \tag{4.3}$$

Annual-mean changes in precipitation can be obtained by averaging the variations (4.3) over a year.

We use top-of-atmosphere insolation to parameterize the intensity factor $\mathcal{M}$ as proportional to equatorial insolation. The rationale for this parameterization is that insolation in the deep tropics sets the precipitation intensity thermodynamically through its control on water vapor content [69]. The latitude of the ITCZ ϕ_m in the model is parameterized as proportional to the difference in area-integrated insolation between the northern and southern hemisphere. This parameterization assumes that the hemispheric insolation difference alone controls the cross-equatorial atmospheric energy flux, and that the ITCZ position is proportional to the cross-equatorial energy flux [e.g., 1, 2, 5, 6, 67, 115].

Precipitation intensity

The intensity factor $\mathcal{M} = P(\phi_m, \lambda, T)$ represents the thermodynamic effects of changes in atmospheric water vapor content on precipitation intensity. Atmospheric water vapor content depends primarily on temperature through the saturation vapor pressure because atmospheric relative humidity, especially over oceans, is energetically constrained to change little as the climate changes [41, 44, 116, 117]. Temperature, in turn, depends primarily on insolation [118] and is fairly homogeneous across the tropics [**Charney63**, 119]. So the intensity factor can be assumed to depend only on insolation at the equator, $S(0, \lambda, T)$, and to be independent, for example, of the ITCZ latitude ϕ_m.

To gain insight into how the intensity factor $\mathcal{M}$ varies with equatorial insolation, we expand it to first order about a reference value of equatorial insolation, S_{ref},

$$\mathcal{M} \approx P_0 + \alpha(S - S_{\text{ref}}), \tag{4.4}$$

which is justified because seasonal and orbital insolation variations at the equator are generally small. Here, P_0 is a reference precipitation intensity, and $\alpha = \partial P/\partial S\big|_{S=S_{\text{ref}}} > 0$ defines the sensitivity of precipitation P to variations in equatorial

insolation $S = S(0, \lambda, T)$. (Similar linear approximations have been implicitly or explicitly made in many paleoclimatological studies.) Because Earth's eccentricity e has been small over its geological past and its obliquity γ is also relatively small (albeit not as small as the eccentricity), variations in equatorial insolation $S(0, \lambda, T)$ in turn can be approximately captured by an expansion to first order in eccentricity and obliquity, which substituted into (4.4) gives

$$\mathcal{M} \approx P_0 + \alpha \left\{ \frac{S_0}{\pi}[1 + 2e\cos(\lambda - \varpi)] - S_{\text{ref}} \right\}. \tag{4.5}$$

Here, S_0 is Earth's solar constant (see appendix 4.8 for details). The approximation (4.5) implies that the precipitation intensity at the ITCZ varies sinusoidally with time of year as measured by solar longitude λ. It has a maximum at perihelion ($\lambda = \varpi$) and a minimum at aphelion ($\lambda = \varpi + 180°$); it would be constant for a circular orbit ($e = 0$). In this small-obliquity and small-eccentricity approximation, obliquity γ and the related solar declination angle do not enter insolation at the equator, although they do affect insolation away from the equator—an approximation that incurs errors of less than 20% in the annual and zonal mean.

ITCZ latitude

The shape factor $\mathcal{S} = \exp\left[-(\phi - \phi_m)^2/(2\sigma^2)\right]$ depends on the ITCZ latitude ϕ_m; the width σ is taken to be fixed. So we need to derive an approximation of the latitude ϕ_m of maximum precipitation (or of the ITCZ) in terms of insolation S. We can do this by relating the ITCZ latitude to the cross-equatorial energy flux F_0 [e.g., 2, 4, 5, 36, 67]. This relation can be expressed as

$$\phi_m \propto -F_0(\lambda - \Delta\lambda, T), \tag{4.6}$$

where $\Delta\lambda$ is a phase delay between changes in ϕ_m and changes in F_0 [2]. The ITCZ latitude ϕ_m is related to the cross-equatorial atmospheric energy transport because when the ITCZ moves away from the equator, the cross-equatorial atmospheric circulation strengthens, transporting more energy from the warmer to the colder hemisphere, or, more precisely, from the hemisphere with net energy input into the atmosphere to the hemisphere with net energy loss [2, 5, 6, 36]. To approximate the ITCZ latitude ϕ_m in terms of S, we assume that the cross-equatorial energy flux F_0 is proportional to the hemispheric difference in area-weighted insolation. Using again the first-order approximation for insolation S in terms of eccentricity e and

obliquity γ (appendix 4.8), this leads to

$$\phi_m(\lambda) \approx \beta\left[\int_0^{\pi/2} \cos(\phi) S(\phi, \lambda - \Delta\lambda, T)\,\mathrm{d}\phi - \int_{-\pi/2}^{0} \cos(\phi) S(\phi, \lambda - \Delta\lambda, T)\,\mathrm{d}\phi\right] \tag{4.7a}$$

$$\approx \frac{\beta S_0 \gamma}{2}\left[1 + 2e\cos(\lambda - \Delta\lambda - \varpi)\right]\sin(\lambda - \Delta\lambda). \tag{4.7b}$$

Here, β is a parameter that measures the sensitivity of the ITCZ latitude ϕ_m to the hemispheric difference in area-averaged insolation. We assume that the sensitivity β

Parameter	Value
P_0	$10\,\mathrm{mm\ day^{-1}}$
S_{ref}	$400\,\mathrm{W\ m^{-2}}$
α	$0.075\,\mathrm{W^{-1}\ m^2\ mm\ day^{-1}}$
β	$0.066^\circ\,\mathrm{W^{-1}\ m^2}$
σ	5.0°
$\Delta\lambda$	60°

Table 4.1: Parameter values for simulations with precipitation model.

of the ITCZ latitude to the integrated hemispheric insolation difference is constant. However, Bischoff & Schneider [67, 115] and Adam *et al.* [19] showed that this sensitivity is not constant but depends on the net energy input to the atmosphere near the equator. This would imply that β is, to first order, a linear function of insolation at the equator. If β were taken to be linear in equatorial insolation, like the intensity factor $\mathcal{M}$, it would not substantially impact the model results, only the interpretation of parameters: to first order in eccentricity e, it would amount to a modification of ϕ_m that is small if the sensitivity β only weakly depends on equatorial insolation.

With the expression (4.7) for the ITCZ latitude, the shape function $\mathcal{S}$ of the precipitation model to first order in eccentricity e and obliquity γ becomes

$$\mathcal{S} \approx \left[1 + e\frac{S_0\beta\gamma}{\sigma^2}\cos(\lambda - \Delta\lambda - \varpi)\sin(\lambda - \Delta\lambda)(\phi - \phi_m^0)\right]\exp\left[-\frac{1}{2\sigma^2}(\phi - \phi_m^0)^2\right], \tag{4.8}$$

where ϕ_m^0 is the ITCZ latitude in the no-eccentricity case ($e = 0$):

$$\phi_m^0 = \frac{1}{2}\beta S_0 \gamma \sin(\lambda - \Delta\lambda). \tag{4.9}$$

The model specified by (4.2), (4.5), (4.8), and (4.9) depends only on insolation as input and on the parameters P_0, S_{ref}, α, β, σ, and $\Delta\lambda$. It was used to generate

the numerical solutions discussed in what follows (for the parameter values used in our simulations, see Table 4.1). The parameters P_0, S_{ref}, α, σ are loosely chosen to obtain realistic precipitation values and shapes for the present-day values of the orbital parameters 4.1. The values for β and $\Delta\lambda$ are chosen to reflect ITCZ location sensitivities similar to the ones found in [2, 8, 67]. It is important to not that no extensive parameter tuning has been performed and that the results presented in this paper are not very sensitive to the exact values of the model parameters.

In this section, we have neglected other factors that can also contribute to the zonally-averaged rainfall responses around the ITCZ location. For example, our model does not take into account the presence of a deep oceanic overturning circulation that has been found to affect the zonal- and annual-mean location of the ITCZ [e.g., 36, 120]. The effect of such a circulation can be included in our model, contributing an additional term on the right-hand side of equation (4.7). This can affect precipitation changes ΔP through modifications of $\mathcal{S}_{\text{ref}}$ in equation (4.3) but not through the perturbation components $\Delta\mathcal{M}$ and $\Delta\mathcal{S}$ (provided the ocean circulation strength does not change appreciably). However, we found that including this effect in equation (4.7) does not change our results substantially.

Appendix 4.9–4.10 goes beyond the expressions developed in this section. There we use equations (4.2)–(4.9) to derive analytic approximations for $\overline{P}$ that provide insights into the dependence of the annual- and zonal-mean precipitation $\overline{P}$ on orbital parameters. For example, the approximations highlight why $\overline{P}$ responds to variations in the longitude of perihelion ϖ although annual-mean insolation does not.

4.4 Response to orbital variations

We illustrate the properties of our model with two representative experiments and compare its hindcasts with tropical precipitation variations inferred from the paleo-record.

Results and discussion

Figure 4.1 shows the model output for two different values of Earth's longitude of perihelion: for perihelion occuring in December (Earth's current perihelion), and in June. The precession response of annual-mean precipitation in our model arises from two effects: Boreal summer insolation reaches a maximum in the northern hemisphere when perihelion precesses from December to June with corresponding weakened insolation during austral summer in the southern hemisphere. This im-

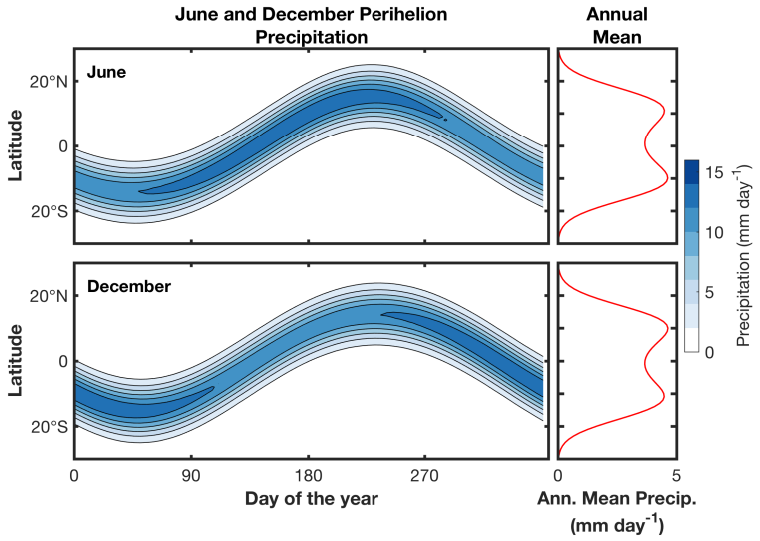

Figure 4.1: Precipitation for two different values of longitude of perihelion ϖ (December and June perihelion). Color contours (blue) indicate precipitation with a contour interval of 2.0 mm day^{-1} and a maximum contour at 16 mm day^{-1}. The red curves in the right panels show annual- and zonal-mean precipitation as a function of latitude. Seasonal maximum precipitation shifts from boreal summer to winter as the longitude of perihelion precesses from June to December. At the same time, in the annual mean, the location of maximum precipitation shifts from the southern to the northern hemisphere due to the nonlinear dependence of the model precipitation on local insolation.

pacts annual-mean precipitation through changes in rainfall intensity and shifts in the ITCZ location. On the other hand, changes in the duration of the seasons (e.g., boreal summer is shortest when perihelion occurs in June, because Earth orbits more rapidly around the sun when it is closer to it) also lead to seasonal ITCZ shifts and concomitant precipitation changes.

The total precipitation changes broken down into intensity changes and changes

due to shifts in the ITCZ according to (4.3) are shown in Figure 4.2. In the annual mean, although annually averaged insolation at each latitude is the same in both simulations, precipitation is enhanced in the subtropics of the hemisphere that receives the more intense summer insolation and is reduced near the equator (see Liu & Schneider [121] for an example of a different planetary climate where this does not occur). The changes in annual-mean precipitation arise because, in our model, precipitation is a nonlinear function of local insolation. Thermodynamic changes in precipitation intensity occur because the intensity factor (reflecting water vapor content) is enhanced around the time of perihelion. Because the ITCZ is in the northern hemisphere in boreal summer, this leads to a dipole pattern in annual-mean precipitation change as a function of latitude when perihelion precesses from December to June: annual-mean precipitation strengthens in the northern hemisphere and weakens in the southern. The annual-mean precipitation changes although there is no change in annual-mean insolation at a given location because the seasonal cycle of the ITCZ position correlates with the precession-induced seasonal water vapor content changes, leading to nonlinearly rectified changes in the annual mean like those seen in aquaplanet GCM simulations [69].

By contrast, dynamic precipitation changes result from shifts of the ITCZ. These occur because the seasonal migration of the ITCZ into the summer hemisphere progresses farther into the hemisphere with summer perihelion: the ITCZ marches farther into the hemisphere with the brighter (and hence, usually, warmer) summer. This leads to dynamically strengthened precipitation in the northern subtropics during boreal summer when perihelion precesses from December to June, and to weakened precipitation in the southern subtropics during austral summer. On the other hand, changes in the duration of the seasons also lead to shift-induced precipitation changes, causing a dipole pattern during winter. In the annual mean, this results in a double dipole pattern of precipitation changes as a function of latitude, with strengthened precipitation in the northern subtropics, weakened precipitation in the northern deep tropics, and oppositely signed changes in the southern hemisphere. Because our model cannot capture zonal variations in precipitation, it should be regarded as a zeroth-order approximation to regions such as the Australo-Asian monsoon sector. For example, in simulations with comprehensive climate models [104, 112], annual- and zonal-mean precipitation changes do not generally have a double dipole pattern because of zonal inhomogeneities in the precipitation field. Instead, the double dipole is present locally, for example, over Asia and Australia [112]. The zonal inhomogeneities lead to cancellations in the zonal average; hence,

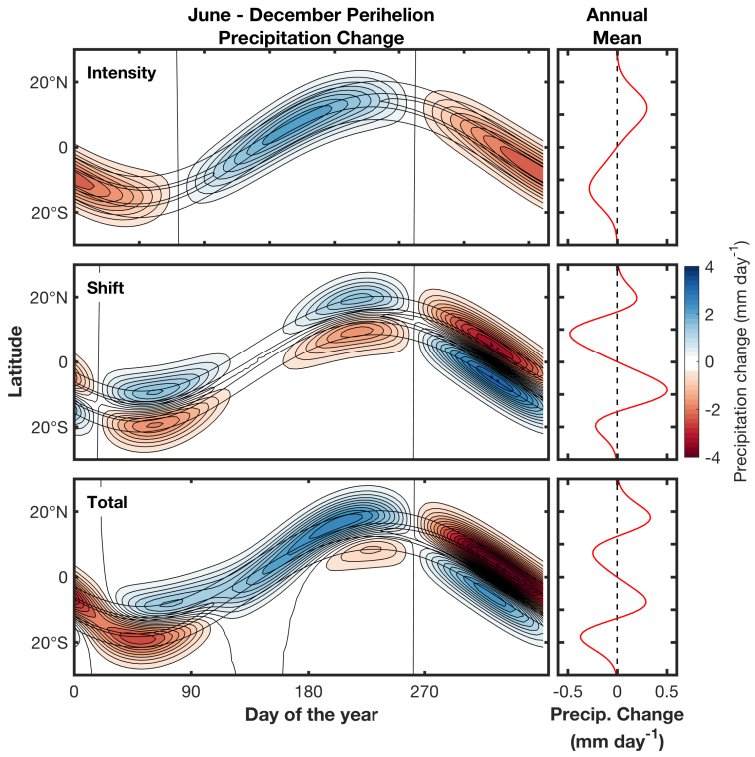

Figure 4.2: Precipitation changes, i.e., differences between the panels in Figure 4.1, owing to precession (variation in longitude of perihelion ϖ from December to June perihelion). Color contours (blue positive, red negative) indicate precipitation changes, with a contour interval of 0.25 mm day^{-1} and a maximum contour at 4 mm day^{-1}. Perihelion occurs in December for the reference case, as is approximately the case for Earth today. The red curves in the right panels show the change in annual-mean precipitation as a function of latitude. Changes in precipitation intensity reflect the thermodynamically strengthened precipitation in the ITCZ around the time when perihelion occurs. Precipitation changes owing to the ITCZ shift occur because the seasonal migration of the ITCZ progresses farther into the hemisphere with the brighter summer (i.e., with summer perihelion).

the pattern does appear in the average.

Figure 4.3 shows the precipitation changes that occur when Earth's obliquity changes from $\gamma = 24.4°$ to $22.4°$. Changes in precipitation intensity in this case are small because near-equatorial insolation changes only weakly when the obliquity varies

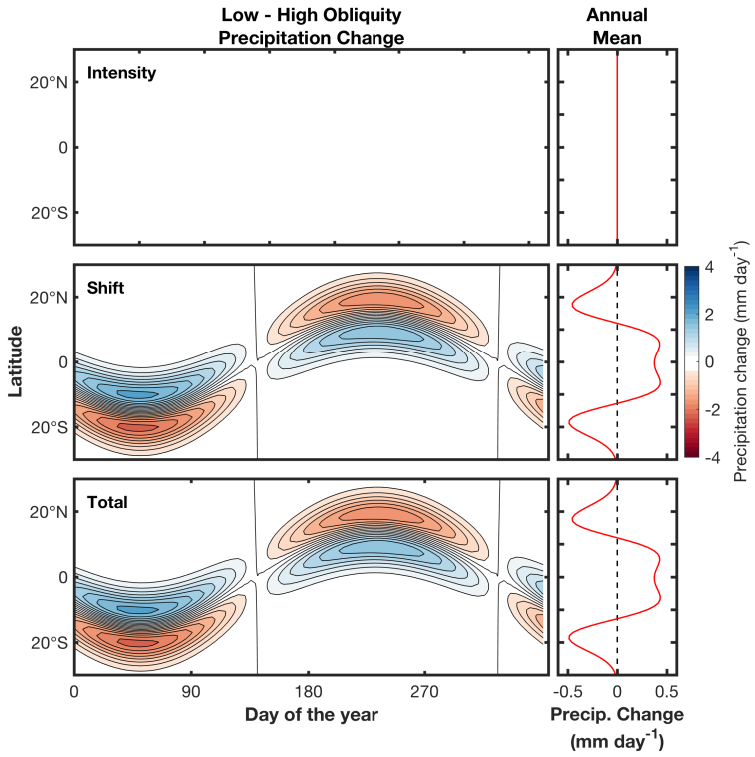

Figure 4.3: Precipitation changes owing to changes in Earth's obliquity from $\gamma = 24.4°$ to $22.4°$. Color conventions are the same as in Figure 4.2. Changes in precipitation intensity are small in this case because near-equatorial insolation changes only weakly when the obliquity varies. Precipitation changes owing to ITCZ shifts are symmetric about the equator because changes in Earth's insolation due to variation in obliquity are symmetric about the equator and are dominated by insolation changes during the solstice seasons.

(the equatorial insolation to first order is independent of obliquity, see appendix 4.8). Because insolation changes under obliquity variations are symmetric about the equator, the annual-mean precipitation changes owing to ITCZ shifts are also symmetric about the equator. Reducing the obliquity weakens the seasonality of insolation. So reducing obliquity weakens annual-mean precipitation in the subtropics dynamically and strengthens it around the equator, because the ITCZ seasonally does not migrate as far poleward for lower obliquities. As a result, total changes in precipitation are dominated by ITCZ shift-induced changes of precipitation.

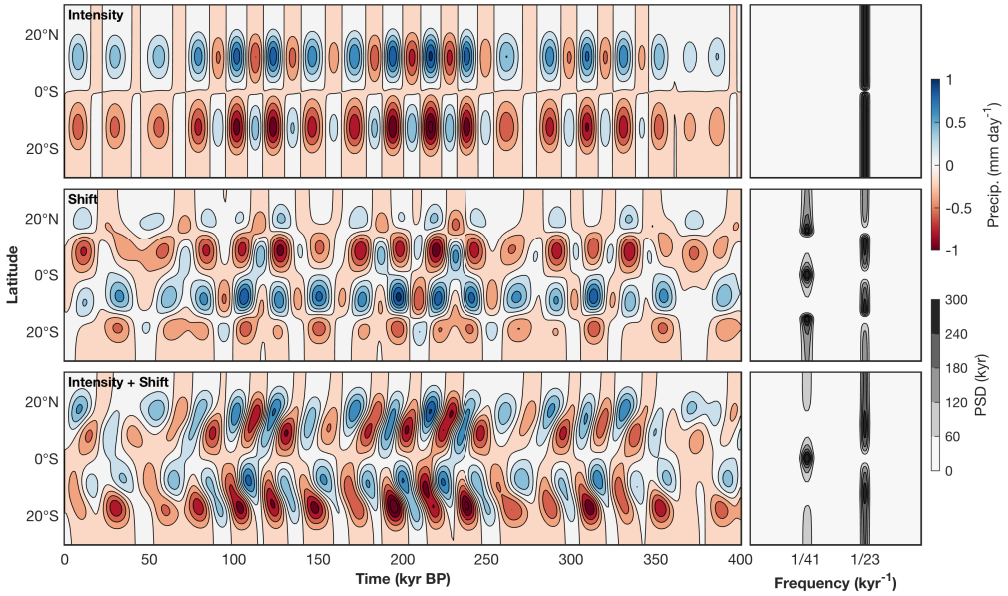

Figure 4.4: Changes in annual-mean precipitation with respect to present-day precipitation. Left panels show time series from model output. Right panels show corresponding Lomb-Scargle [122, 123] periodogram power spectral density estimates for the detrended and standardized time series. Precipitation changes due to changes in precipitation intensity and due to shifts in the seasonal cycle of the ITCZ show the characteristic anti-phasing between hemispheres, but are almost out of phase with each other near the equator. As a result, the phase lines for changes in total precipitation (intensity + shift) are tilted which results in a phase lag of subtropical changes compared to near-equatorial changes. The power spectral density estimate is dominated at the 23 kyr precession band but also shows significant power at the 41 kyr obliquity band. At the equator where hemispherically anti-phased changes vanish, precipitation changes are driven solely by changes in obliquity.

Figure 4.4 shows the model prediction as a function of time and latitude split into intensity changes $\Delta\mathcal{M} \times \mathcal{S}_{\text{ref}}$ (top row) and changes induced by ITCZ shifts $\mathcal{M}_{\text{ref}} \times \Delta\mathcal{S}$ (center row). The dipole and double dipole patterns from Figures. 4.2 and 4.3 are again obvious. It is evident from Figure 4.4 that phase shifts between subtropical and near-equatorial precipitation emerge through a superposition of intensity and shift-induced changes, leading to a meridional tilt with time of positive and negative anomalies in the total changes (bottom row). Similar phase shifts are also seen in paleoclimate records. The right column in Figure 4.4 shows the power spectral density estimates of the model time series. In our model, shift-induced changes introduce a strong obliquity signal in the spectra, especially near the equator. By comparison, obliquity variations lead to only weak intensity changes

near the equator because near-equatorial insolation variations (Eq. (4.12)) induced by obliquity variations are weak (especially compared with subtropical or extratropical insolation variations).

Comparison with paleo-records

The model's response to orbital variations can be compared with geological and geochemical precipitation records of the past 350 ka, which span the northern- and southern-hemisphere subtropics and tropics. We drive the model with orbital insolation variations for this period [124–126]. Figure 4.5 shows the precipitation variations the model produces (black lines), standardized to unit variance, together with paleo-records from China, West Africa, Borneo, Papua New Guinea (PNG), and Brazil (orange/cyan) [11–15, 17, 18, 113, 127, 128]. The gray vertical bars indicate glacial terminations [113].

The data from China, Borneo, and Brazil are speleothem records. The signal shown is the oxygen isotopic composition (δ^{18}O) of speleothem calcite, interpreted to reflect regional precipitation strength. These records have been dated radiometrically (with U-Th dating), leading to precise and accurate age control. In some cases, interpreting subtropical speleothem records, such as the ones from China, to reflect precipitation strength locally, is not appropriate as these records can instead reflect upstream rainfall closer to the equator (e.g., over India and the Indian Ocean) [e.g., 129]. The record from West Africa is based on the Zr content in sediments at ODP Site 658, derived by X-ray fluorescence (XRF) scanning. Zr is used a proxy for grain size and thus the relative importance of dust input, expected to decrease under wetter conditions. The age model is established for the most part by matching benthic δ^{18}O in the core to the global benthic δ^{18}O stack of Lisiecki & Raymo [130], and some fine-tuning of sedimentary signals to nearby radiocarbon-dated cores in the uppermost part of the record [128]. The Papua New Guinea data are (Ti/Ca) count ratios (plotted as ln(Ti/Ca)) in sediment core MD97-2140, again derived by XRF scanning. The ratio is used as a proxy for terrigenous input to the ocean, interpreted as reflecting river runoff. The record is also dated by oxygen isotope stratigraphy, and radiocarbon dating in the youngest part [17]. For comparison, the uppermost record (red/blue) shows standardized δ^{18}O data from the benthic Lisiecki & Raymo [130] stack, which reflects a combination of global ice volume and deep-sea temperature and is used here as a rough proxy of global-mean temperature variations.

It is evident that the model captures many of the orbital precipitation variations

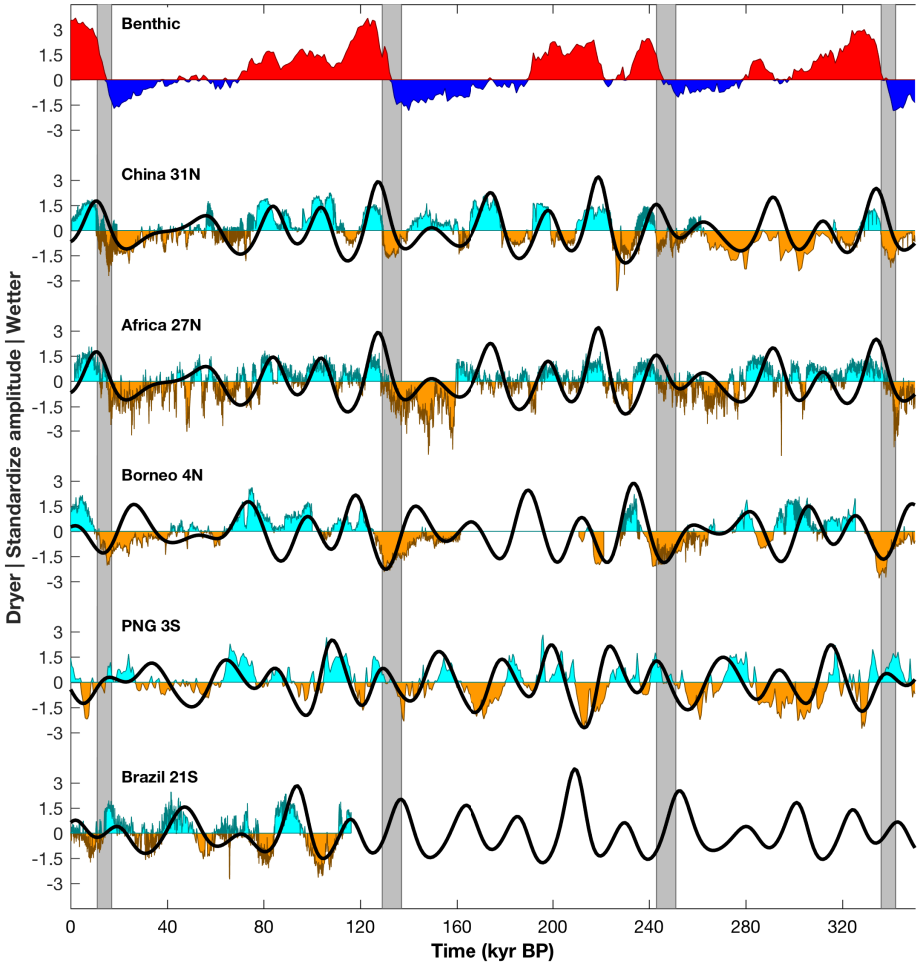

Figure 4.5: Comparison of model with precipitation proxies from the paleo-record for past 350 ka. Colors (orange/cyan) show standardized precipitation proxies and black lines the corresponding standardized precipitation variations at the proxy latitude obtained from the model. Eastern China records are from the Hulu, Sanbao and Linzhu caves [11, 14, 113]. The African record is from ODP Site 658 [128]. The Borneo records are from different caves in Mulu National Park [13, 15, 18, 127]. The Papua New Guinea record is from the sediment core MD97-2140 [17]. The Brazilian record is from Botuvera cave [12]. All time series are de-trended and rescaled to unit variance.

recorded in the paleo-proxies. The agreement is best for subtropical records, where the model is able to capture, for example, the characteristic anti-phasing between Chinese and Brazilian records. For subtropical records, the agreement is better for northern-hemisphere records from China and West Africa, where the model captures the records well for the past 350 ka. For the Brazilian record the agreement is reasonable, but model-data comparisons are hampered by the limited length of the record. For records from Borneo, the model captures the behavior well between approximately 60 ka and 160 ka and 220 ka and 270 ka, whereas there are substantial model-data discrepancies between 0 ka and 60 ka. The discrepancies for the past 60 ka cannot be resolved by manipulating the model parameters, which points to effects not captured by our model, such as the zonal variations shown to be important in GCM simulations [112]. The model agrees well with the record from Papua New Guinea, where the past 350 ka are captured.

It is particularly noteworthy that the model captures the phase shift by around 10 ka between precipitation extrema in the subtropical Eastern China caves and the equatorial Borneo record. For example, the Eastern China cave records [11, 14, 113] indicate a precipitation maximum during or immediately after the past four glacial terminations. By contrast, the corresponding precipitation maximum in Borneo [13, 15, 18, 127] occurs about 10 ka later. It has been suggested that such phase shifts may arise because of the impact of insolation changes on El-Niño variability [15, 18]. Our model suggests that even in the absence of El Niño modulations and other zonally varying climate changes, a phase shift between the precipitation variations in the subtropics and deep tropics can occur through an interplay of orbital effects on precipitation intensity and ITCZ shifts.

Figure 4.6 shows the same records as in Figure 4.5 but focusing on the past 160 ka, to see variations in greater detail. The gray lines show standardized insolation curves near the location where the records are taken at the times of the year deemed relevant for local precipitation by the authors of the respective studies (typically, the time of year when the ITCZ is overhead). For the Borneo record [13, 15, 18], both our model and the insolation curve used in Carolin *et al.* [15, 18] provide good fits to the data. For the Papua New Guinea record [17], our model shows better agreement with the data than the insolation curve used in Tachikawa *et al.* [17]. For all subtropical records, there is no substantial difference between the commonly used insolation curves and our model. This is because the ITCZ passes overhead only once per year, and precipitation changes in our model are driven

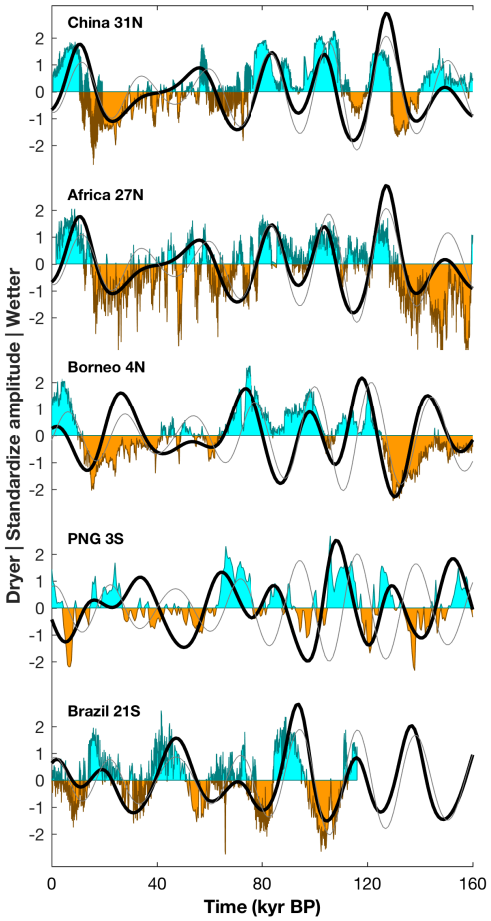

Figure 4.6: Comparison of model with precipitation proxies from the paleo-record for past 160 ka. As in Figure 4.5, colors show standardized precipitation proxies and black lines the corresponding standardized precipitation variations at the proxy latitude obtained from the model. Grey lines show standardized insolation at 31° N (China), although many studies use insolation at 65° N, 27° N (Africa), 4° N (Borneo), 3° S (PNG), and 21° S (Brazil) for solar longitudes 90° (China), 90° (Africa), 180° (Borneo), 270° (PNG), and 270° (Brazil). All time series are detrended and rescaled to unit variance.

primarily by changes in summer insolation, which affect the intensity and the shift component of precipitation similarly in the subtropics. However, an advantage of our physically motivated precipitation model is that it can point to mechanisms of tropical precipitation changes.

Figure 4.7 shows the power spectral density estimates corresponding to the proxy time series in Figures 4.5 and 4.6 (left column) and the power spectral density estimates for the precipitation model (black lines) as well as for representative insolation curves (red lines, which correspond to the grey lines in Figure 4.6). Almost all proxy time series show significant power at the 23-kyr precession band and at the 41-kyr obliquity band, except for the proxy record from Brazil, which is too short for a 41-kyr peak to be significant. In contrast to insolation curves near the equator, which do not contain significant power in the obliquity band, our precipitation model predicts significant power in the obliquity band even for rainfall records near the equator. This can be understood from Equation (4.12) because all terms involving the sine of latitude are very small near the equator so that the obliquity dependence of insolation becomes a second-order effect near the equator. The precipitation model predicts significant power at the obliquity band even around the equator because higher-latitude insolation, which is affected by obliquity variations, impacts rainfall near the equator in the annual mean. It does so through ITCZ shifts and changes in timing of the ITCZ passage, which which can be seen in Figure 4.4 (right column).

For all records shown in Figs. 4.5–4.7, our model provides reasonable fits to the standardized precipitation data, even for sites that are located at very different longitudes. In addition, our model is able to capture the phase shifts between records from different latitudes, e.g., in the subtropics (China or Brazil) and deep tropics (Borneo or Papua New Guinea). The parameters of the precipitation model were not tuned to provide a best fit to the records shown in the figures. Rough approximations about the dynamical and thermodynamical properties of the atmospheric circulation suffice to generate reasonable agreement between the model and the data.

4.5 Conclusions

In this paper we presented and analyzed an idealized numerical precipitation model for tropical latitudes. The model approximates the zonally- and annually averaged precipitation field using only insolation as input. Even without extensive calibration of the parameters, we find that the model estimate for mean precipitation in the

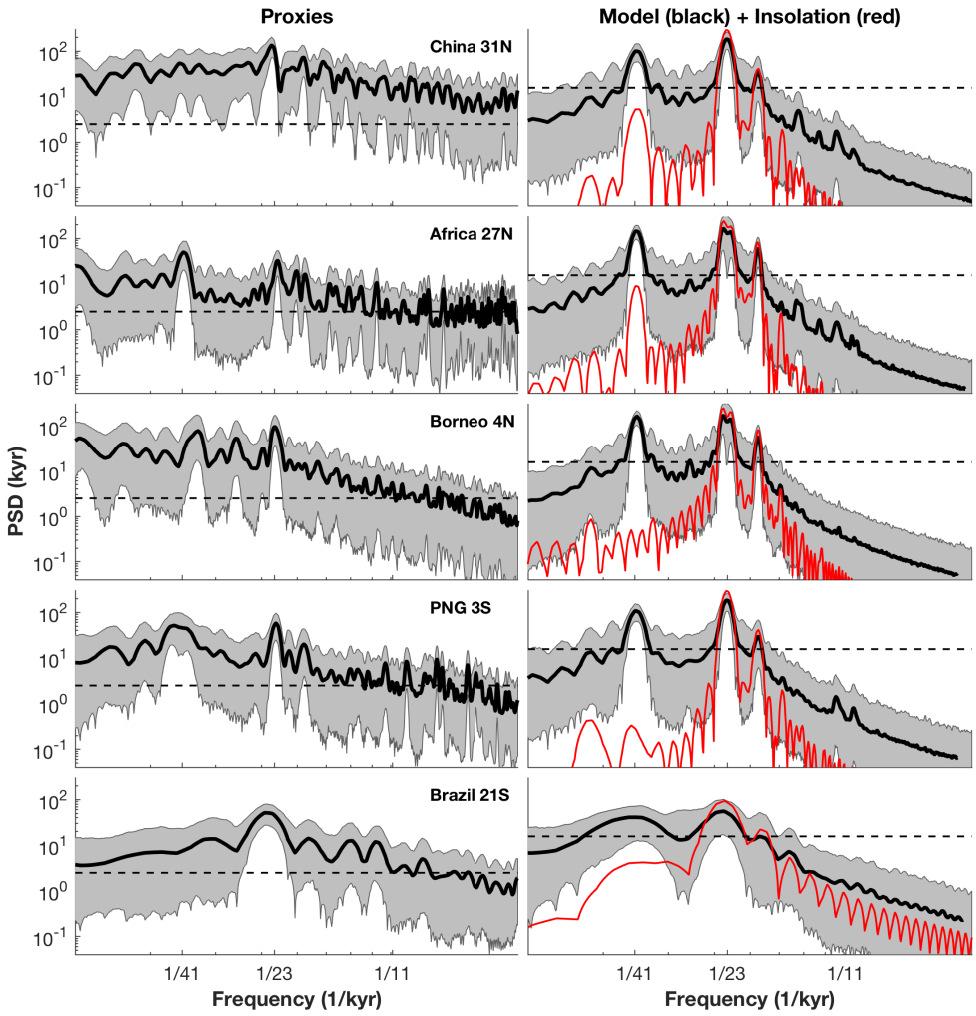

Figure 4.7: Spectral density estimates of precipitation proxies (left column) from the paleo-record using the standardized and detrended time series from Figure 4.5. Solid lines show bootstrap sample mean estimates. Grey areas show 95% bootstrap confidence interval (see appendix for details of the method). The black dashed lines shows the 95% detection probability threshold. The 23 kyr precession peak is significant in all records and the 41 kyr obliquity peak is significant in all records but the records from China and Botuvera cave in Brazil. Right column shows corresponding spectral density estimates of precipitation model (black lines) based on model time series of the same length at the corresponding proxy time series. The precipitation model was evaluated at 31° N (China), 27° N (Africa), 4° N (Borneo), 3° S (PNG), and 21° S (Brazil). Grey areas again show the 95% confidence interval. Red lines show the spectral density estimate of the standardized insolation curves at the same locations for solar longitudes 90° (China), 90° (Africa), 180° (Borneo), 270° (PNG), and 270° (Brazil).

tropics agrees well with standardized paleoclimatological records over the past several hundred thousand years.

More concretely, to study how differences among precipitation records from different latitudes arise, we compared the model output to a set of tropical precipitation records collected near latitudes ranging from approximately 30° S to 30° N. We find that our model can capture phase shifts among subtropical precipitation records [11, 12, 14, 113] and records that were collected from sites near the equator [13, 15, 18, 127], and that these phase lags are caused by the interplay of changes in precipitation intensity and shifts of the ITCZ. In addition, our model is able to explain the spectral power of these proxy records at the precession and obliquity bands, showing that shifts in the ITCZ location over the seasonal cycle can introduce an obliquity signal in near-equatorial precipitation, which cannot be explained by local insolation alone.

Our results provide a framework in which a wide range of paleoclimatological records can be interpreted mechanistically. For example, it has been suggested that phase shifts among different tropical precipitation records arise due to complex dynamical processes stemming from zonal variations in the oceanic and atmospheric circulations [e.g., 15, 17, 18]. It is certainly the case that continental configuration and zonal asymmetries in circulations, among other things, play an important role in determining local precipitation in the tropics. But already our relatively simple conceptual model reproduces phase shifts across latitudes like those inferred from paleo-precipitation records. Zonal variations and regional circulation specifics may be superimposed on this zeroth-order approximation to understand in more detail how low-latitude precipitation varies on orbital timescales. We propose the precipitation model presented here as a null hypothesis that can be tested with future low-latitude precipitation records. In general, phase lags between records can stem from a variety of sources, and our model makes clear predictions about the frequency content and the phase relationships between different latitudes owing to just the insolation changes at the top of the atmosphere.

4.6 Appendix A: Spectral density estimation

Spectral density estimation is performed using the Lomb–Scargle periodogram method [122, 123, 131, 132] for unevenly spaced time series on the detrended, zero-mean, and unit-variance time series. The 95% confidence intervals on the spectral densities are determined via resampling from the original time series using a nonparametric bootstrapping procedure that takes the autocorrelations of the time

series into account [133]. We resample the original time series by drawing block samples of random length L_i to obtain a new time series of the same length L as the original data time series (for the last block we use a truncation to obtain the correct total length L). The block lengths L_i are drawn from a geometric distribution with probability mass function $p(1-p)^{L_i-1}$, where p is the inverse of the optimal block length for the time series [134]. We draw 1000 bootstrap samples using this procedure and estimate the Lomb-Scargle periodogram for each one of the bootstrap samples to obtain a probability density function at each frequency which allows us to determine the 95% confidence interval at each frequency. The detection probability is estimated by assuming as null hypothesis that the data is composed of independent Gaussian random variables.

4.7 Appendix B: Solar longitude

The solar longitude λ is the angular distance the Earth has moved along its orbit since vernal equinox. It is therefore a shifted true anomaly, which in turn measures the angular distance between perihelion and Earth's position along its orbit. Using Kepler's second law, the time derivative of the solar longitude is approximately given by

$$\frac{\mathrm{d}\lambda}{\mathrm{d}t} \approx \frac{2\pi}{Y_a}\frac{(1+e\cos(\lambda-\varpi))^2}{\left(1-e^2\right)^{3/2}} \approx \frac{2\pi}{Y_a}\left(1+2e\cos(\lambda-\varpi)\right), \tag{4.10}$$

where $Y_a = 365.26\ \mathrm{d} = 31558464\ \mathrm{s}$ is the anomalistic year, e is the eccentricity of Earth's orbit, and ϖ is the longitude of perihelion [124]. In the second step in equation (4.10) we expanded the expression on the right-hand side to first-order in eccentricity using a Taylor expansion, i.e., it is the small eccentricity limit of the left-hand side. The main benefit of this relation for our purposes, is that it can be used to convert integrals of functions that depend indirectly on time through $\lambda = \lambda(t)$ into integrals over λ itself.

4.8 Appendix C: Earth's insolation

In order to formulate the precipitation model with insolation as input only, we need an analytic formula for Earth's top-of-atmosphere insolation profile. Here, we use the expression

$$S = \frac{S_0}{\pi}\frac{(1+e\cos(\lambda-\varpi))^2}{(1-e^2)^2}\left[H_0\sin(\phi)\sin(\delta)+\cos(\phi)\cos(\delta)\sin(H_0)\right], \tag{4.11}$$

where, $H_0 = \arccos(-\tan(\phi)\tan(\delta))$, with $\delta = \arcsin(\sin(\gamma)\sin(\lambda))$, and γ is the obliquity of Earth's axis of rotation. The expression in equation (4.11) can be

simplified by expanding the right-hand side to first order in eccentricity (for $e \ll 1$) and also assuming that $\gamma \ll 1$. This gives

$$S \approx \frac{S_0}{\pi}(1 + 2e\cos(\lambda - \varpi))\left[\frac{\pi}{2}\gamma\sin(\phi)\sin(\lambda) + \cos(\phi)\right]. \tag{4.12}$$

Using the approximation from equation (4.12) instead of equation (4.11) introduces an average error in the annual- and zonal-mean precipitation field of less than 20 %.

4.9 Appendix D: Laplace's method

We used Laplace's method to derive an approximation for the annual-mean precipitation field $\overline{P}$ in section 4.9. This is a method that can be helpful for approximating integrals of the form

$$I = \int_a^b h(x)e^{\epsilon f(x)}\,\mathrm{d}x. \tag{4.13}$$

Here, we assume that h and f are smooth functions over the interval $[a, b]$. Using Laplace's method, it can be shown that these kinds of integrals can be approximated as

$$I = \int_a^b h(x)e^{\epsilon f(x)}\,\mathrm{d}x = \sum_{x_0}\sqrt{\frac{2\pi}{\epsilon|f''(x_0)|}}h(x_0)e^{\epsilon f(x_0)} \text{ for } \epsilon \to \infty, \tag{4.14}$$

where x_0 are the (not necessarily unique but discrete) maxima of $f(x)$ within the interval (a, b), and $f''(x_0) < 0$ [135]. The idea being that as ϵ approaches large values, the integral is dominated by the maxima of the exponential within the interval (a, b).

Mean precipitation in the deep tropics ($|\phi| < \frac{1}{2}\beta S_0\gamma$)

To develop analytical approximations of precipitation variations, we first focus on the deep tropics, defined here as the latitudes for which $|\phi| < \frac{1}{2}\beta S_0\gamma$ holds. That is, we focus on the latitudes that lie withing the maximum excursions of the ITCZ in the model at zero eccentricity. This also means that within the latitude band defined by $|\phi| < \frac{1}{2}\beta S_0\gamma$, the ITCZ crosses twice per year over each latitude ϕ. For the interpretation of paleoclimatological records of tropical precipitation, we need to derive an approximation for annual-mean precipitation because rainfall proxies usually are recording precipitation throughout the year. To do so, we integrate equation (4.5) over the length of one anomalistic year $Y_a = 365.26$ d (the time difference between two consecutive perihelion passages) to get

$$\overline{P}(\phi, T) = \frac{1}{Y_a}\int_0^{Y_a} P(\phi, \lambda, T)\,dt. \tag{4.15}$$

Here, a problem arises because we are interested in the integral over time, although all quantities so far were derived using solar longitude λ as parameter. Fortunately, using Kepler's second law and equation (4.10) from the appendix, we can introduce a coordinate transformation from time t to solar longitude λ. The integral in equation (4.15) can then be rewritten as

$$\overline{P} = \frac{1}{Y_a} \int_0^{Y_a} P(\phi, \lambda(t), T)\, dt \tag{4.16a}$$

$$\approx \frac{1}{2\pi} \int_0^{2\pi} P(\phi, \lambda, T)\,(1 - 2e\cos(\lambda - \varpi))\, d\lambda, \tag{4.16b}$$

where we used $\lambda = \lambda(t)$ in the first step to make the implicit time dependence of λ clear. The expression in the second step of equation (4.16) is an approximation because we used a first-order expansion in eccentricity for the coordinate transform. Using Laplace's method for the approximation of integrals that involve exponential factors and restricting ourselves to tropical latitudes between the maximum excursions of the ITCZ (see appendix 4.9 for the details of this method), we can approximate the last integral in equation (4.18) to get

$$\overline{P} \approx \frac{1}{\sqrt{2\pi}} \sum_{\lambda_m^0} \underbrace{\left| \frac{\sigma}{\partial_\lambda \phi_m^0 |_{\lambda=\lambda_m^0}} \right| \left(1 - 2e\cos\left(\lambda_m^0 - \varpi\right)\right)}_{\tau\text{: ITCZ crossing time scale}} \underbrace{\left(P_0 + \alpha\left(S(0, \lambda_m^0, T) - S_{\text{ref}}\right)\right)}_{\wp\text{: precipitation amount}}, \tag{4.17}$$

where λ_m^0 is the solar longitude at which $\phi = \phi_m^0$. Here, the exponential factor used in Laplace's approximation is the exponential factor in equation (4.8) which has a maximum at $\phi = \phi_m^0$. Under this scenario, the ITCZ crosses over every location ϕ twice (between the latitudes of maximum ITCZ excursion), which means there are two different λ_m^0 for every ϕ; hence the summation sign in the above equation. Equation (4.17) can be interpreted as follows: The annual-mean precipitation at latitude ϕ is determined by the amount of rainfall that occurs when the ITCZ is directly overhead but weighted by the time it takes the ITCZ to cross a latitude band of width σ centered at the latitude ϕ. This is intuitive because the slower the ITCZ move across a latitude ϕ, the more rain accumulates. In what follows, we seek to simplify equation (4.17) further by expanding all relevant quantities to first order in eccentricity e. Using the expansions from equations (4.5) and (4.8) and solving for λ_m^0 using equation (4.9), we can obtain analytical expressions for τ and $\wp$. The resulting analytical expansion of the zonal- and annual-mean precipitation in terms

of eccentricity e is given by

$$\overline{P} \approx \sqrt{\frac{2}{\pi}} \frac{2\sigma}{\beta S_0 \gamma} \left(1 - \left(\frac{2\phi}{\beta S_0 \gamma}\right)^2\right)^{-\frac{1}{2}} \left(P_0 + \alpha \left(\frac{S_0}{\pi} - S_{\text{ref}}\right) - e \frac{2\phi}{\beta S_0 \gamma} \sin(\Delta\lambda - \varpi) \left[P_0 - \alpha S_{\text{ref}}\right]\right). \tag{4.18}$$

This equation is valid if σ and e are small and as long as ϕ is within the maximum excursions of the ITCZ. Equation (4.18) demonstrates that changes in the mean precipitation $\overline{P}$ due to changes in the longitude of perihelion ϖ only matter when $e > 0$. Furthermore, such changes impact $\overline{P}$ anti-symmetrically because the first-order term in eccentricity e is linear (antisymmetric) in latitude ϕ. Equation (4.18) also illustrates that in this model and to first-order in eccentricity, precipitation records from sites on the equator ($\phi = 0$) do not contain any variations due to precession.

4.10 Appendix E: Mean precipitation in the subtropics ($|\phi| > \frac{1}{2}\beta S_0 \gamma$)

Next we focus on the subtropics, defined as the latitudes for which $|\phi| > \frac{1}{2}\beta S_0 \gamma$, that is, we focus on the latitudes that lie poleward of the maximum ITCZ excursions at zero eccentricity. At such latitudes, the ITCZ is never located directly overhead. Instead, it is precipitation from the flanks of the ITCZ that is responsible for the precipitation. The integral in equation (4.16) can then be approximated using Laplace's method in the same way as before, the only difference being that $\lambda_m^0 = \Delta\lambda + \pi/2$ for $\phi > 0$ and $\lambda_m^0 = \Delta\lambda + 3\pi/2$ for $\phi < 0$. This is because the zero in the exponent of the f in the Laplace approximation occurs when $\partial\phi_m(\lambda)/\partial\lambda = 0$, the time when the ITCZ movement approximately changes direction. We arrive at the expression

$$\overline{P} \approx \sqrt{\frac{1}{2\pi}} \frac{\sigma \sqrt{\frac{2}{\beta S_0 \gamma}}}{\sqrt{\left|\phi + \chi \frac{\beta S_0 \gamma}{2}\right|}} \Bigg[P_0 + \alpha \left(\frac{S_0}{\pi} - S_{\text{ref}}\right) - \chi e \Bigg(2 \sin(\Delta\lambda - \varpi) \left[P_0 - \alpha S_{\text{ref}}\right] \tag{4.19a}$$

$$+ P_0 + \alpha \left(\frac{S_0}{\pi} - S_{\text{ref}}\right) \frac{S_0 \beta \gamma}{\sigma^2} \sin(\varpi) \left(\phi + \chi \frac{\beta S_0 \gamma}{2}\right)\Bigg)\Bigg] \exp\left(-\frac{1}{2\sigma^2}\left(\phi + \chi \frac{\beta S_0 \gamma}{2}\right)^2\right) \tag{4.19b}$$

for the mean precipitation in the subtropics. Here, the $\chi = -1$ branch corresponds to latitudes north of the equator and the $\chi = +1$ branch corresponds to latitudes south of the equator. Equation (4.19) is valid if σ and e are small. It again demonstrates

that changes in the mean precipitation $\overline{P}$ due to changes in the longitude of perihelion ϖ only matter when $e > 0$.

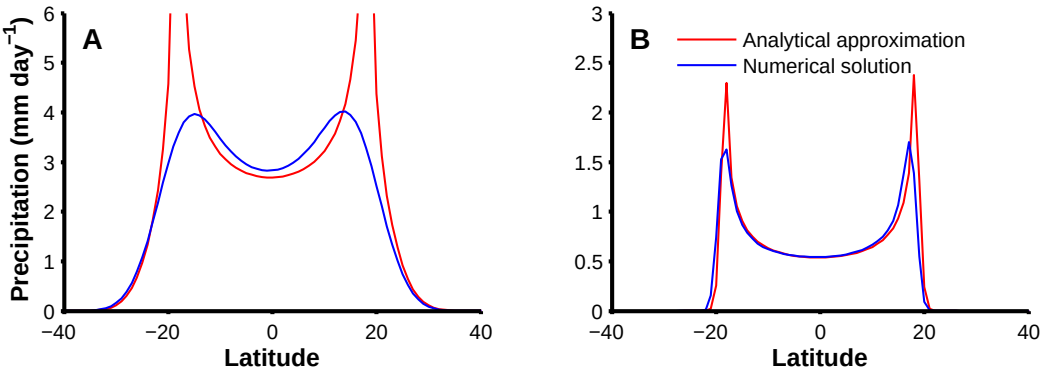

Figure 4.8: Precipitation from the numerical model (blue line) and the numerical approximations from equations (4.18) and (4.19) (red line). Panel A shows the situation for $\sigma = 5°$ and panel B shows the same case for $\sigma = 1°$. The orbital parameter values for this case are given by $e = 0.017236$, $\gamma = 23.446°$, and $\varpi = 281.37°$. The analytical solution diverges at the maximum displacement of the ITCZ away from the equator because the asymptotic expansion to first-order in σ used in Laplace's method breaks down in the vicinity of the maximum displacements. One can also see that as σ is decreased, the analytical solution approaches the numerical solution better. This is expected as Laplace's method is an approximation for small σ.

Figure 4.8 compares the numerical version of $\overline{P}$ (blue line) with the analytical approximation from equations (4.18) and (4.19) (red line) for $e = 0.017236$, $\gamma = 23.446°$, and $\varpi = 281.37°$. Except for a very narrow region around the maximum excursions of the ITCZ, the analytical solutions from equations (4.18) and (4.19) approximate the numerical solution well. Comparing equations (4.18) and (4.19) we can see that there a few differences arising from the fact that in the deep tropics, the ITCZ crosses over a latitude ϕ twice per year. Equation (4.19) retains a shape component from the model, that is, it retains the exponential from the definition of $\mathcal{S}$, causing a difference in the phase between deep tropical and subtropical latitudes.

Chapter 5

CONFIGURATION OF A SOUTHERN OCEAN STORM TRACK

1. Bischoff, T. & Thompson, A. F. Configuration of a Southern Ocean storm track. *J. Phys. Oceangr.* **44.** doi:10.1175/JPO-D-14-0062.1 (2014).

5.1 Abstract

Diagnostics of ocean variability that reflect and influence local transport properties of heat and chemical species vary by an order of magnitude along the Southern Ocean's Antarctic Circumpolar Current (ACC). Topographic "hotspots" are important regions of localized transport anomalies. This study uses a primitive equation channel model to investigate the structure of eddy kinetic energy (EKE), one measure of variability, in an oceanic regime. A storm track approach emphasizes the importance of stationary eddies, which result from flow interactions with topography, on setting EKE distributions. The influence of these interactions extends far downstream of the topography and impacts EKE patterns through localized convergence and divergence of heat. Unlike for zonal averages, local contributions to the stationary fluxes from terms that integrate to zero in a zonal average are important. The simulations show a strong sensitivity of the zonal structure as well as the distribution and amplitude of stationary eddy fluxes to the surface wind forcing. By focussing on local, time-averaged stationary eddy fluxes, insight into the dynamical structure of the ACC can be gained that is concealed in the averaging procedure associated with traditional zonal or along-stream analyses.

5.2 Introduction

The distribution of EKE impacts the complex dynamical balances of momentum, heat and tracers in the Southern Ocean. The dominant feature of the Southern Ocean EKE distribution, revealed in early altimetric data, is its enhancement around topographic "hotspots", such as Kerguelen or Campbell Plateaus [e.g., 136]. Consequently, eddy diffusivities, which reflect transport properties [e.g., 137] and are required to accurately represent the ACC in coarse numerical models, display strong zonal variability along the ACC. Similarities with zonal variations of EKE in the atmosphere have led to a consideration of ocean storm tracks and their role in maintaining the ACC's vorticity balance [138–140].

In the atmospheric literature, storm tracks have been defined as regions of locally enhanced EKE. The existence and dynamics of these atmospheric storm tracks have been linked to various forcing mechanisms that locally increase baroclinicity [e.g., 141, 142]. These forcings include zonally-varying orography or patterns of surface heat flux convergence due to the presence of boundary currents. Recent studies have shown that the structure and zonal extent of atmospheric storm tracks (enhanced EKE) can partly be explained via the excitation of stationary Rossby waves [143, 144] that locally increase baroclinicity downstream of a forcing region. The length scale of atmospheric storm tracks can be inferred from the length scale of stationary atmospheric Rossby waves [e.g., 143–146]. However, it is unclear how in an oceanic regime the presence of stationary meanders can also act to localize EKE.

Theories of residual heat, momentum and tracer transport in the Southern Ocean rely mostly on a zonally or stream-wise averaged framework [e.g., 147]. Thus, the residual overturning streamfunction of the Southern Ocean gives an average picture of the dynamics, as it is only meaningfully defined if the boundary terms in the zonal or stream-wise average of the momentum equations vanish. Observations identify significant zonal asymmetry in ACC properties [e.g., 148, 149]. The number of jets and fronts vary with bottom topography [150] and the meridional transport of heat and tracers can be strongly enhanced around major topographic features [e.g., 151, 152]. Zonally-averaged theories are naturally unable to explain these observations and conceal local aspects of the dynamics within integrated quantities and theories for zonally-varying flows need to be considered. In this context, previous work has highlighted the importance of stationary eddy fluxes on the momentum balance in the context of blocked reentrant channels that are forced by constant surface wind stress [e.g., 153, 154]. Our goal is to explore variability in the meander structure and eddy characteristics in response to changes in the wind stress forcing by analyzing a set of idealized channel simulations with a long channel and consider how flow interactions with topography shape high EKE regions in an oceanic regime.

5.3 Idealized simulations

Simulations were performed with the MITgcm [155] which is used to solve the hydrostatic Boussinesq equations on a beta-plane. Our model is similar to the one in [156]. Unlike [156], we use a channel that is 8000 km long, 2000 km wide and 3 km deep. The resolution is 5 km in the horizontal directions with 30 unevenly spaced layers in the vertical that vary from 12.5 m at the surface to 125 m at the lowest level. The Rossby radius varies between $\sim$ 10 km at the southern boundary of the domain

and $\sim$ 30 km at the northern boundary. Sub-grid processes are represented by a horizontal viscosity of 12 $\mathrm{m^2 s^{-1}}$, a vertical viscosity of $3 \cdot 10^{-4}$ $\mathrm{m^2 s^{-1}}$, and a vertical diffusivity of temperature of $5 \cdot 10^{-6}$ $\mathrm{m^2 s^{-1}}$. We neglect variations of density with salinity and use a fixed thermal expansion coefficient of $\alpha = 2 \cdot 10^{-4}$ $\mathrm{K^{-1}}$. The flow is subject to a Coriolis force with reference Coriolis parameter $f_0 = -10^{-4}$ $\mathrm{s^{-1}}$ and gradient $\beta = 10^{-11}$ $\mathrm{m^{-1} s^{-1}}$ as well as a gravitational acceleration of $g = 9.81$ $\mathrm{ms^{-2}}$. The bathymetry is given by

$$h(x, y) = h_0 \exp\left(-\frac{(x - x_\mathrm{m})^2}{2\sigma_x^2} - \frac{(y - y_\mathrm{m})^2}{2\sigma_y^2}\right). \tag{5.1}$$

Here, $\sigma_x = 283$ km, $\sigma_y = 141$ km, x denotes the along-channel coordinate, y the across-channel coordinate, $h_0 = 1.5$ km is the height of the mountain, x_m is arbitrary due to the periodicity of the channel and $y_\mathrm{m} = 1000$ km. The flow is forced via a steady, zonally-symmetric zonal surface wind stress:

$$\tau_\mathrm{s}(y) = \tau_0 \cos\left(\frac{\pi\,(y - y_\mathrm{m})}{L_\mathrm{y}}\right), \tag{5.2}$$

where τ_0 is varied between 0.05 $\mathrm{Nm^{-2}}$ and 0.4 $\mathrm{Nm^{-2}}$ and $L_\mathrm{y} = 2000$ km is the channel width. Bottom friction is parameterised as $\tau_u = \rho r_b \partial_z u$, with density $\rho = 1000$ $\mathrm{kgm^{-3}}$ and friction coefficient $r_b = 1.1 \cdot 10^{-3}$ $\mathrm{ms^{-1}}$. To maintain a realistic stratification we use a 100 km wide sponge layer at the northern boundary, where the stratification is relaxed towards an exponential profile ranging from 0° C at the bottom to 8° C at the surface with a scale height of 1 km. The relaxation time scale decreases towards the northern boundary and has a minimum value of 7 days at $y = 2000$ km [cf. 156].

Fig. 5.1a shows the vertically averaged EKE at $\tau_0 = 0.2\,\mathrm{Nm^{-2}}$. The flow field shows a single, strong jet around and immediately in the lee of the Gaussian mountain, but breaks up into many, weaker jets further downstream (Fig. 5.1b). This is similar to observations in the Southern Ocean [157, 158]. The baroclinic structure of the flow is similar to that observed in the ACC and similar to simulations in [156], although the total transport of the flow is large (between 100 Sv for $\tau_0 = 0.05\,\mathrm{Nm^{-2}}$ and 900 Sv for $\tau_0 = 0.4$ $\mathrm{Nm^{-2}}$) because the momentum dissipation is largely accomplished by bottom friction in our simulations.

5.4 Stationary meanders and heat transport

[139] link ocean storm tracks to the divergence of eddy vorticity fluxes, while [143, 144] propose that the shape of atmospheric storm tracks can be understood from

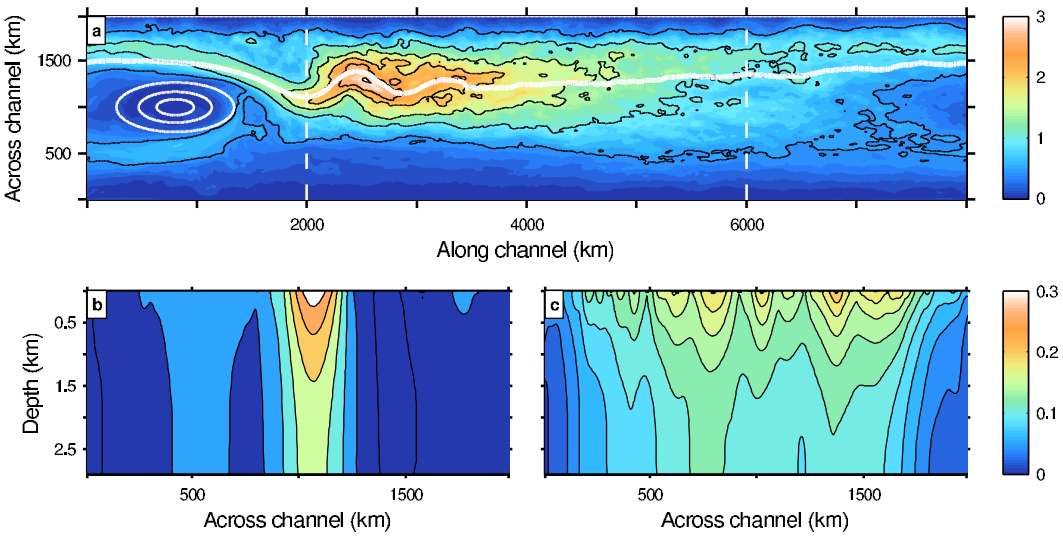

Figure 5.1: **Panel a)** Vertically-averaged transient EKE (10^{-2} m^{2}s^{-2}) for the reference simulation at $\tau_0 = 0.2$ Nm^{-2}. The white ellipses show the bathymetry at 2750 m, 2250 m and 1750 m; the white curve shows the 5.1 °C surface isotherm. **Panels b) & c)** Time-averaged zonal velocity at $x = 2000$ km and at $x = 6000$ km; velocities in panel b) are rescaled by a factor of 2.

the relationship between stationary eddy heat fluxes and the generation of transient EKE. In particular, the presence of a local external forcing causes stationary eddy heat fluxes to locally enhance baroclinicity. The time mean temperature (buoyancy) flux $\overline{\mathbf{u}T}$ can be decomposed into components due to zonal mean fluxes, stationary eddy fluxes and transient eddy fluxes. Using standard notation from [73], we have

$$\overline{\mathbf{u}T} \equiv [\overline{\mathbf{u}}][\overline{T}] + \overline{\mathbf{u}}^*[\overline{T}] + [\overline{\mathbf{u}}]\overline{T}^* + \overline{\mathbf{u}}^*\overline{T}^* + \overline{\mathbf{u}'T'}. \tag{5.3}$$

Here, the overbar $\overline{(.)}$ denotes a time average and primes $(.)'$ the associated deviations. The brackets $[.]$ denote a zonal average and stars $(.)^*$ the deviations from the zonal average. Under the assumption of steady state (or long-time mean) and a linear equation of state, the thermodynamic equation reads

$$Q \approx \nabla \cdot \left(\langle [\overline{\mathbf{u}}][\overline{T}] \rangle + \langle \overline{\mathbf{u}'T'} \rangle + \langle \overline{\mathbf{u}}^\dagger \overline{T}^\dagger \rangle \right), \tag{5.4}$$

where the divergence of the standing component is given by

$$\nabla \cdot \langle \overline{\mathbf{u}}^\dagger \overline{T}^\dagger \rangle \equiv \nabla \cdot \left(\langle \overline{\mathbf{u}}^* [\overline{T}] \rangle + \langle [\overline{\mathbf{u}}] \overline{T}^* \rangle + \langle \overline{\mathbf{u}}^* \overline{T}^* \rangle \right). \tag{5.5}$$

Here, Q denotes all possible forms of diabatic heating and $\langle . \rangle$ denotes the vertical mass-weighted integral. When averaging Eq. (5.4) zonally along the channel,

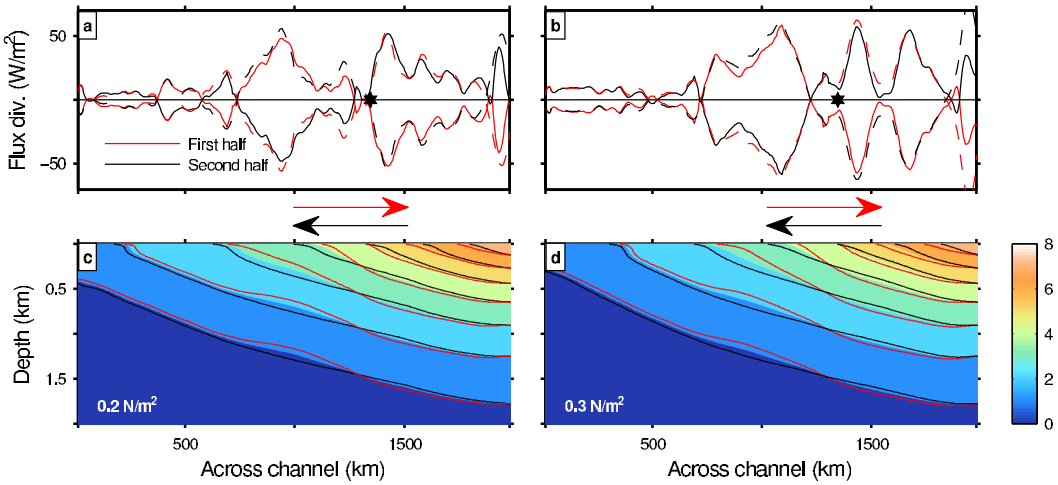

Figure 5.2: **Upper panels** Stationary (solid lines) and transient (dashed lines) flux divergence anomalies, defined in Eq. (5.6) and Eq. (5.7), over the first ($0 < x < L_x/2$, red curves) and second ($L_x/2 < x < L_x$, black curves) halves of the channel. The star indicates the zonal mean position of the 5.1 °C isotherm. Positive (negative) values indicate cooling (heating). **Lower panels** The zonal-mean temperature field (colors) and temperature contours averaged over the first (red curves) and second (black curves) halves of the domain. Panels (a, b) and (c, d) are for a simulation with $\tau_0 = 0.2$ Nm^{-2} and $\tau_0 = 0.3$ Nm^{-2} respectively. The arrows are indicating the direction of the anomalous heat flux due to the presence of stationary eddies in the two channel regions.

one recovers that in a time and zonal-mean framework the heat flux divergence is composed of the divergences of mean fluxes, stationary eddy fluxes, and transient eddy fluxes. Yet, *locally*, the transport of the zonal mean temperature field by the stationary meandering component of the flow $\overline{\mathbf{u}}^*[\overline{T}]$ and the transport of the meandering component of the temperature field by the zonal mean flow $[\overline{\mathbf{u}}]\overline{T}^*$ are significant. Locally, all three components of $\langle \overline{\mathbf{u}}^\dagger \overline{T}^\dagger \rangle$ in Eq. (5.5) can be significant, although over much of the channel, albeit not everywhere, the divergence of the stationary flux can be approximated by the sum of the two components that vanish in the zonal mean, *e.g.*, $\nabla \cdot \Big(\langle \overline{\mathbf{u}}^* [\overline{T}] \rangle + \langle [\overline{\mathbf{u}}] \overline{T}^* \rangle \Big)$. This is characteristic of a linear wave.

Fig. **??** emphasizes the local character of the stationary fluxes by considering regional anomalies of the stationary energy flux divergence $\mathcal{D} \equiv \rho c_p \nabla \cdot \langle \overline{\mathbf{u}}^\dagger \overline{T}^\dagger \rangle$ over the first and second halves of the domain:

$$\mathcal{D}_1 = [\mathcal{D}]_1 - [\mathcal{D}], \quad \mathcal{D}_2 = [\mathcal{D}]_2 - [\mathcal{D}], \tag{5.6}$$

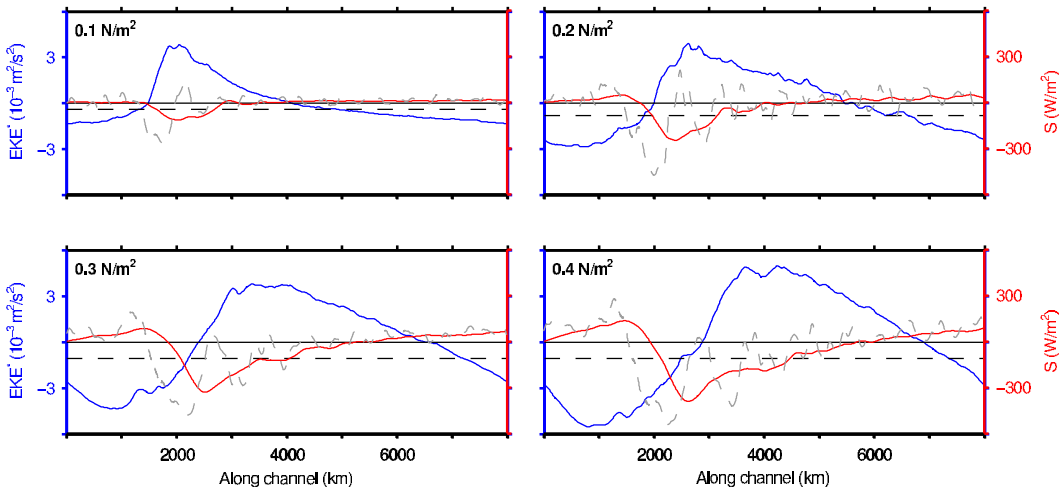

Figure 5.3: Depth- and cross-channel-averaged EKE anomaly (difference from domain average, blue line) and S, defined in Eq. (5.8), (grey dashed line with red the 1000 km running mean) for different amplitudes of the wind stress. Storm tracks are defined by positive values of the blue curve. The black dashed line shows the difference in total EKE between simulations with and without topography for comparison.

$$[\cdot]_1 \equiv \frac{1}{L_x/2}\int_0^{L_x/2} \cdot \,\mathrm{d}x, \quad [\cdot]_2 \equiv \frac{1}{L_x/2}\int_{L_x/2}^{L_x} \cdot \,\mathrm{d}x. \tag{5.7}$$

Here, ρ and c_p are the density and the heat capacity of sea water. Dividing the channel into two halves is arbitrary, but simplifies the analysis compared to a dynamically determined separation boundary and makes the comparison amongst experiments easier. Focusing on anomalies is practical, because the stationary eddy flux divergence anomalies and the transient eddy flux divergence anomalies, by definition, must approximately sum to zero over the first and second half of the channel. The anomalous stationary energy flux divergence around and in the lee of the mountain (first half of channel) acts, on average, to steepen the isopycnals compared to the channel-averaged stratification, i.e., the associated anomalous fluxes are up the mean gradient, while downstream of the mountain (second half) they act to relax isopycnals compared to the channel average. The steepening effect of stationary eddies over the first half of the channel is counteracted by a relaxation effect due to transient eddies as expected from transient eddies generated by baroclinic instability that act to relax isopycnals. This is reflected in both the flux divergences (Fig. 5.2 a & b) and the stratification (Fig. 5.2 c & d). It is the component of the stationary flux $\nabla \cdot \left(\langle \overline{\mathbf{u}}^* [\overline{T}] \rangle + \langle [\overline{\mathbf{u}}] \overline{T}^* \rangle \right)$ that integrates to zero over the entire domain that largely contributes to the local flux divergence and to changes in stratification along

the channel. However, the nonlinear term $\nabla \cdot \langle \overline{\mathbf{u}}^* \overline{T}^* \rangle$ is important and cannot be neglected.

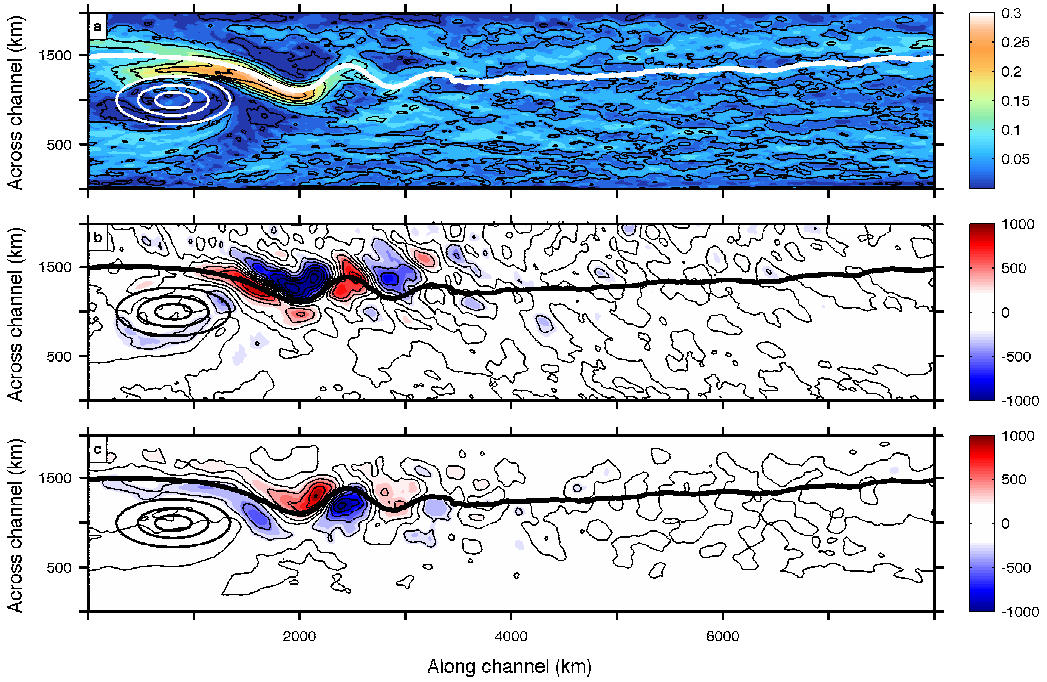

Figure 5.4: Panel (a): Above-sill average ($z < 1.5$ km) of Eady growth rate ($\sigma = 0.31 f \frac{\partial_z u}{N}$, where u is the zonal velocity field and N is the buoyancy frequency) in units of day^{-1} for wind stress amplitude $\tau = 0.2$ Nm^{-2}. Panel (b,c): Mass-weighted vertical integral of energy flux divergences in W/m^2 for the $\tau = 0.2$ Nm^{-2} simulation. (b) $\nabla \cdot \langle \rho c_p \overline{\mathbf{u}}^\dagger \overline{T}^\dagger \rangle$ and (c) $\nabla \cdot \langle \rho c_p \overline{\mathbf{u}'T'} \rangle$. All fields are smoothed with a two-dimensional box filter of size 100 km $\times$ 100 km.

The amplitude of surface westerlies over the Southern Ocean have increased during the past few decades [159]. To explore how elevated EKE regions in the ACC may respond to these changes, we consider the equilibrated response of our model to a range of wind stress amplitudes, 0.05 Nm^{-2} $\leq \tau_0 \leq$ 0.4 Nm^{-2} with a wide range of bottom flow speeds. We define the storm track as a deviation from the zonally-averaged EKE distribution. The equilibrated EKE of simulations with flat bottom topography are provided for reference (Fig. 5.3, dashed line). The ability of the stationary eddy fluxes to tilt isopycnals locally is diagnosed from the average stationary eddy temperature flux divergence found north and south of the temperature contour $T_c = 5.1$ °C and then taking the difference between the northern and the southern average:

$$S = \frac{1}{2} \rho c_p \left(\left\{ \nabla \cdot \langle \overline{\mathbf{u}}^\dagger \overline{T}^\dagger \rangle \right\}_{y(x,T_c)}^{L_y} - \left\{ \nabla \cdot \langle \overline{\mathbf{u}}^\dagger \overline{T}^\dagger \rangle \right\}_{0}^{y(x,T_c)} \right). \tag{5.8}$$

Here, braces {.} denote an area-weighted integral; $S < 0$ ($S > 0$) implies a tendency for the standing eddies to steepen (relax) isopycnals, because of the associated cross-frontal eddy heat transports.

Fig. 5.3 shows zonal variations in depth- and cross-channel-averaged EKE (blue curves) and S (red curves) as a function of τ_0. The zonal extent of the storm track increases as the wind stress increases. The region where $S < 0$ also increases but the spatial separation between the maximum amplitudes in S and EKE grows with increasing wind stress. This is likely due to growing separation between regions of eddy generation and maximum eddy mixing, similar to the atmospheric case [160, 161]. At the same time, the region where $S < 0$ is found further downstream. In addition, plots of the Eady growth rates [139, 162], a standard measure of baroclinicity (see Fig. 4a), show the separation between regions of largest baroclinicity and highest EKE are not colocated. The distance separating the two maxima is likely exaggerated in our simulation compared to the actual ACC because of the larger flow speeds advecting eddies in our simulations. Note that the Eady growth rate, as defined in [162], can be related to the isopycnal tilt through thermal wind balance. Because local Eady growth rates measure the baroclinicity of the flow locally, they provide insight into where the flow is most likely susceptible to baroclinic instability (see for example [139] for an application to storm tracks).

Fig. 5.3 shows that the dominant length scale of the meandering flow is about O(1000km) (gray dashed line). It is much larger than the energy containing length scale of transient eddies O(100km) and the Rossby radius of deformation O(10km). Similar to [143], we find that with increased wind stress amplitude, the meandering flow extends further downstream along with the region where stationary eddy fluxes act to increase the isopycnal tilt ($S < 0$) and the region of anomalously high EKE. Somewhat surprisingly, EKE values downstream of the EKE maximum are actually suppressed in comparison to simulations without topography, consistent with a region where $S > 0$.

5.5 Discussion

In our idealized setting, stationary eddy fluxes of heat (buoyancy) increase baroclinicity downstream of a simple Gaussian mountain. The location of strongest isopycnal tilting is not collocated with the maximum in EKE anomaly (Fig. **??**, Fig. 4). While the bathymetric features are more complex in the ACC, stationary meanders are known to be sites of enhanced EKE. We also find that our results agree

qualitatively with studies using ocean GCMs with more complex topography e.g. [140]. Additionally, rapid transitions in eddy characteristics found in high resolution ocean GCMs are consistent with the dynamics seen here.

Previous studies have suggested that stationary heat fluxes play an important role in shaping atmospheric storm tracks [143, 144]. Our simulations show that the vertically-averaged stationary heat fluxes are consistent with steeper isopycnals locally, and that this steepening happens at length scales that are larger than the typical size of transient eddies (Fig. 5.2, Fig. 4b,c). An intriguing result is that the dominant contribution to these anomalous upgradient heat fluxes by stationary eddies is associated with components that must integrate to zero along the entire channel. We note that an alongstream coordinate system will eliminate the stationary flux component. However, we argue that this change of coordinate system requires some *a priori* knowledge of the mean flow structure.

A key result of this study is that the structure of stationary meanders changes in response to an increased surface wind stress consistent with what is expected from eddy advection and local instability theory [139, 160]. Current views of Southern Ocean equilibration [e.g., 163] suggest that transient eddies compensate an increase in wind-driven Ekman overturning. Here, stationary fluxes respond to changes in meander size, which accompany a change in zonal mean flow. This behavior is consistent with a modification in the standing Rossby wavelength [138]. The associated change in EKE is localized in the stationary meander (Fig. **??**) and is at least partly a consequence of the increased baroclinicity, although barotropic instability may be active as well [164]. Thus, the eddy characteristics do not respond to a global change in stratification, but rather a local flux divergence. The distribution of this flux divergence and its release through baroclinic instability is also sensitive to the surface forcing and mean flow. Thus, to accurately study Southern Ocean ocean storm tracks, or the interactions between mean flow, stationary meanders and eddies of the ACC, not only is eddy-resolving temporal and spatial resolution required, but also a long domain that permits the system to adjust in a realistic manner. Since the topography of the ACC varies over a broad range of length scales, it will be important to consider the amplitude and distribution of stationary buoyancy fluxes with more realistic configurations.

The simulations presented here have an ACC transport that is too high to represent the real ACC because the channel is never fully blocked at depth at all latitudes. This leads to large bottom flow speeds. Although the barotropic component of the

flow is larger than in nature and therefore the size of the standing meander might be unrealistically large in our simulations, the general principle of stationary heat fluxes tilting isopycnals remains valid in all our simulations, which span a wide range of surface wind stress forcings and mean flow amplitudes. Future process models should address the transient response of the channel stratification to a change in wind stress in a similar domain.

Chapter 6

CONCLUSIONS

This thesis presents an overview over recent theoretical progress regarding the dynamics of the ITCZ. It shows that theories for the location of the ITCZ, at least in idealized settings, provide valuable insights into why and how, mechanistically, ITCZ shifts occur.

In Chapter 2, we show how a diagnostic energetic framework for the ITCZ location can be developed from the energy balance of the atmosphere, and how it can be applied to different climate change scenarios. We find that in our global warming experiments with an idealized moist GCM the ITCZ shifts away from the equator as the planet warms because the asymmetry in atmospheric latent energy transport increases as the climate warms. This is similar to the findings of [20] who arrive at similar results with an aqua-planet GCM, albeit in a more complex setting. In addition to this, we show that under tropical warming, the ITCZ can shift towards the equator because the sensitivity of the ITCZ to the cross-equatorial moist static energy flux decreases, a mechanism previously not recognized in the context of the atmospheric moist static energy budget. We find that this effect is important even in our global warming simulations as a decrease in the sensitivity partly offsets the effect of the strong increase in cross-equatorial moist static energy flux.

In Chapter 3, we describe how the same approach from Chapter 2 can be applied to the situation of double-ITCZs. While in Chapter 2, we used a first-order Taylor expansion for the atmospheric moist static energy flux around the equator, in Chapter 3, we go beyond first order and show how higher-order terms in the expansion impact the state of the ITCZ (single- and double-ITCZ). We find that, using the same idealized GCM as in Chapter 2, the location of the ITCZ is not always linearly related to the cross-equatorial moist static energy flux, but that when the net energy input to the atmosphere around the equator is small enough, a power law with exponent $1/3$ emerges. We also show that when the energy input to the atmosphere near the equator becomes negative, the ITCZ transitions from a single-ITCZ to a double-ITCZ state, provided that the cross-equatorial moist static energy flux remains small enough. This effect had previously not been recognized in the context of the energy balance of the atmosphere.

In Chapter 4, we apply some of the insights from Chapters 2 and 3 to develop an idealized precipitation model that only uses top-of-atmosphere insolation as input. We show that the results from this model can serve as a null hypothesis when interpreting paleoclimatological precipitation records, because the model incorporates two of the main drivers of potential precipitation changes–rainfall amount and location of the ITCZ. In an idealized scenario, both factors can impact how much rain reaches the surface at a given site. Despite the simplicity of our model, we are able to approximately capture the orbital behavior and phase relationships between some of the longest precipitation records from China, Borneo, Africa, and South America [11–16, 18].

Chapter 5 is unrelated to questions about ITCZ dynamics but instead deals with the dynamics of oceanic storm tracks, that is regions of enhanced turbulent kinetic energy in the Southern Ocean. We show that their location and EKE levels are associated with locally steeper isopycnals related to stationary meanders. We show, in an idealized setting, that increased surface wind stress likely leads to longer meanders and therefore larger regions of strongly enhanced EKE with potential importance for cross-frontal tracer transport in the Southern Ocean.

BIBLIOGRAPHY

1. Schneider, T., Bischoff, T. & Haug, G. H. Migrations and Dynamics of the Intertropical Convergence Zone. *Nature* **513,** 45–53 (2014).
2. Donohoe, A., Marshall, J., Ferreira, D. & McGee, D. The relationship between ITCZ location and cross equatorial atmospheric heat transport; from the seasonal cycle to the Last Glacial Maximum. *J. Climate* **26,** 3597–3618 (2013).
3. Chiang, J. C. H. & Bitz, C. M. Influence of high latitude ice cover on the marine Intertropical Convergence Zone. *Clim. Dynam.* **25,** 477–496 (2005).
4. Broccoli, A. J., Dahl, K. A. & Stouffer, R. J. Response of the ITCZ to northern hemisphere cooling. *Geophys. Res. Lett.* **33,** L01702 (2006).
5. Kang, S. M., Held, I. M., Frierson, D. M. W. & Zhao, M. The response of the ITCZ to extratropical thermal forcing: Idealized slab-ocean experiments with a GCM. *J. Climate* **21,** 3521–3532 (2008).
6. Kang, S. M., Frierson, D. M. W. & Held, I. M. The tropical response to extratropical thermal forcing in an idealized GCM: The importance of radiative feedbacks and convective parameterization. *J. Atmos. Sci.* **66,** 2812–2827 (2009).
7. Chiang, J. C. H. & Friedman, A. R. Extratropical cooling, interhemispheric thermal gradients, and tropical climate change. *Ann. Rev. Earth Planet. Sci.* **40,** 383–412 (2012).
8. Donohoe, A., Marshall, J., Ferreira, D., Armour, K. & McGee, D. The interannual variability of tropical precipitation and inter-hemispheric energy transport. *J. Climate,* in press (2014).
9. Lin, J.-L. The double-ITCZ problem in IPCC AR4 coupled GCMs: Ocean-atmosphere feedback analysis. *J. Climate* **20,** 4497–4525 (2007).
10. Tian, B. Spread of model climate sensitivity linked to double-Intertropical Convergence Zone bias. *Geophys. Res. Lett.* **42,** 4133–4141 (2015).
11. Wang, Y.-J. *et al.* A high-resolution absolute-dated late Pleistocene monsoon record from Hulu Cave, China. *Science* **294,** 2345–2348 (2001).
12. Cruz, F. W. *et al.* Insolation-driven changes in atmospheric circulation over the past 116,000 years in subtropical Brazil. *Nature* **434,** 63–66 (2005).
13. Partin, J. W., Cobb, K. M., Adkins, J. F., Clark, B. & Fernandez, D. P. Millennial-scale trends in west Pacific warm pool hydrology since the Last Glacial Maximum. *Nature* **449,** 452–455 (2007).
14. Wang, Y. *et al.* Millennial-and orbital-scale changes in the East Asian monsoon over the past 224,000 years. *Nature* **451,** 1090–1093 (2008).

15. Carolin, S. A. *et al.* Varied response of western Pacific hydrology to climate forcings over the last glacial period. *Science* **340,** 1564–1566 (2013).

16. Cheng, H., Sinha, A., Wang, X., Cruz, F. W. & Edwards, R. L. The Global Paleomonsoon as seen through speleothem records from Asia and the Americas. *Clim. Dyn.* **39,** 1045–1062 (2012).

17. Tachikawa, K., Timmermann, A., Vidal, L., Sonzogni, C. & Timm, O. E. CO< sub> 2</sub> radiative forcing and Intertropical Convergence Zone influences on western Pacific warm pool climate over the past 400ka. *Quaternary Sci. Rev.* **86,** 24–34 (2014).

18. Carolin, S. A. *et al.* Northern Borneo stalagmite records reveal West Pacific hydroclimate across MIS 5 and 6. *Earth Planet. Sc. Lett.* **439,** 182–193 (2016).

19. Adam, O., Bischoff, T. & Schneider, T. Seasonal and interannual variations of the energy flux equator and ITCZ. Part I: Zonally averaged ITCZ position. *J. Climate* (in press).

20. Frierson, D. M. W. & Hwang, Y.-T. Extratropical influence on ITCZ shifts in slab ocean simulations of global warming. *J. Climate* **25,** 720–733 (2012).

21. Waliser, D. E. & Gautier, C. A satellite-derived climatology of the ITCZ. *J. Climate* **11,** 2162–2174 (1993).

22. Adler, R. F. *et al.* The version-2 global precipitation climatology project (GPCP) monthly precipitation analysis (1979-present). *J. Hydrometeorol.* **4,** 1147–1167 (2003).

23. Berry, G. & Reeder, M. J. Objective identification of the Intertropical Convergence Zone: Climatology and trends from the ERA-Interim. *J. Climate* **5,** 1894–1909 (2014).

24. Haug, G. H., Hughen, K. A., Sigman, D. M., Peterson, L. C. & Röhl, U. Southward migration of the Intertropical Convergence Zone through the Holocene. *Science* **293,** 1304–1308 (2001).

25. Arbuszewski, J. A., Cléroux, C., Bradtmiller, L., Mix, A., *et al.* Meridional shifts of the Atlantic Intertropical Convergence Zone since the Last Glacial Maximum. *Nat. Geosc.* **6,** 959–962 (2013).

26. Koutavas, A. & Lynch-Stieglitz, J. in *The Hadley Circulation: Present, Past, and Future* (eds Diaz, H. F. & Bradley, R. S.) 347–369 (Springer, Heidelberg, 2004).

27. Vellinga, M. & Wood, R. A. Global climatic impacts of a collapse of the Atlantic thermohaline circulation. *Climatic Change* **54,** 251–267 (2002).

28. Chiang, J. C. H., Biasutti, M. & Battisti, D. S. Sensitivity of the Atlantic Intertropical Convergence Zone to Last Glacial Maximum boundary conditions. *Paleoceanography* **18,** 1094 (2003).

29. Yoshimori, M. & Broccoli, A. J. Contribution of ocean overturning circulation to tropical rainfall peak in the northern hemisphere. *J. Climate.* **17,** 4399–4423 (2008).

30. Cvijanovic, I. & Chiang, J. C. H. Global energy budget changes to high latitude North Atlantic cooling and the tropical ITCZ response. *Clim. Dynam.* **40,** 1435–1452 (2013).

31. Dai, A. & Wigley, T. M. L. Global patterns of ENSO-induced precipitation. *Geophys. Res. Lett.* **27,** 1283–1286 (2000).

32. Rotstayn, L. D. & Lohmann, U. Tropical rainfall trends and the indirect aerosol effect. *J. Climate* **15,** 2103–2116 (2002).

33. Hwang, Y.-T., Frierson, D. M. & Kang, S. M. Anthropogenic sulfate aerosol and the southward shift of tropical precipitation in the late 20th century. *Geophys. Res. Lett.* **40,** 2845–2850 (2013).

34. Neelin, J. D. & Held, I. M. Modeling tropical convergence based on the moist static energy budget. *Mon. Wea. Rev.* **115,** 3–12 (1987).

35. Fasullo, J. T. & Trenberth, K. E. The annual cycle of the energy budget. Part II: Meridional structures and poleward transports. *J. Climate* **21,** 2313–2325 (2008).

36. Frierson, D. M. W. *et al. Nat. Geosc.* **6,** 940–944 (2013).

37. Fučkar, N. S., Xie, S.-P., Farneti, R., Maroon, E. A. & Frierson, D. M. W. Influence of the extratropical ocean circulation on the Intertropical Convergence Zone in an idealized coupled general circulation model. *J. Climate* **26,** 4612–4629 (2013).

38. Marshall, J., Donohoe, A., Ferreira, D. & McGee, D. The ocean's role in setting the mean position of the Inter-Tropical Convergence Zone. *Clim. Dynam.* 1–13 (2013).

39. Ganachaud, A. & Wunsch, C. Improved estimates of global ocean circulation, heat transport and mixing from hydrographic data. *Nature* **408,** 453–457 (2000).

40. Mayer, M. & Haimberger, L. Poleward atmospheric energy transports and their variability as evaluated from ECMWF reanalysis data. *J. Climate* **25,** 734–752 (2012).

41. O'Gorman, P. A. & Schneider, T. The hydrological cycle over a wide range of climates simulated with an idealized GCM. *J. Climate* **21,** 3815–3832 (2008).

42. Frierson, D. M. W., Held, I. M. & Zurita-Gotor, P. A gray-radiation aquaplanet moist GCM. Part I: Static stability and eddy scale. *J. Atmos. Sci.* **63,** 2548–2566 (2006).

43. Frierson, D. M. W. The dynamics of idealized convection schemes and their effect on the zonally averaged tropical circulation. *J. Atmos. Sci.* **64,** 1959–1976 (2007).

44. Schneider, T., O'Gorman, P. A. & Levine, X. J. Water vapor and the dynamics of climate changes. *Rev. Geophys.* **48,** RG3001 (2010).

45. O'Gorman, P. A., Lamquin, N., Schneider, T. & Singh, M. S. The relative humidity in an isentropic advection-condensation model: Limited poleward influence and properties of subtropical minima. *J. Atmos. Sci.* **68,** 3079–3093 (2011).

46. Levine, X. J. & Schneider, T. Response of the Hadley circulation to climate change in an aquaplanet GCM coupled to a simple representation of ocean heat transport. *J. Atmos. Sci.* **68,** 769–783 (2011).

47. Hwang, Y.-T. & Frierson, D. M. W. Increasing atmospheric poleward energy transport with global warming. *Geophys. Res. Lett.* **37,** L24807 (2010).

48. Pierrehumbert, R. T. The hydrologic cycle in deep-time climate problems. *Nature* **419,** 191–198 (2002).

49. Caballero, R. & Langen, P. L. The dynamic range of poleward energy transport in an atmospheric general circulation model. *Geophys. Res. Lett.* **32,** L02705 (2005).

50. Caballero, R. & Hanley, J. Midlatitude eddies, storm-track diffusivity, and poleward moisture transport in warm climates. *J. Atmos. Sci.* **69,** 3237–3250 (2012).

51. Held, I. M. & Soden, B. J. Robust responses of the hydrological cycle to global warming. *J. Climate* **19,** 5686–5699 (2006).

52. Seager, R., Harnik, N., Kushnir, Y., Robinson, W. & Miller, J. Mechanisms of hemispherically symmetric climate variability. *J. Climate* **16,** 2960–2978 (2003).

53. O'Gorman, P. A. & Schneider, T. Stochastic models for the kinematics of moisture transport and condensation in homogeneous turbulent flows. *J. Atmos. Sci.* **63,** 2992–3005 (2006).

54. Pierrehumbert, R. T., Brogniez, H. & Roca, R. in *The Global Circulation of the Atmosphere* (eds Schneider, T. & Sobel, A. H.) 143–185 (Princeton University Press, Princeton, NJ, 2007).

55. Uppala, S. M. *et al.* The ERA-40 re-analysis. *Quart. J. Roy. Meteor. Soc.* **131,** 2961–3012 (2005).

56. Galewsky, J., Sobel, A. & Held, I. Diagnosis of subtropical humidity dynamics using tracers of last saturation. *J. Atmos. Sci.* **62,** 3353–3367 (2005).

57. Voigt, A., Stevens, B., Bader, J. & Mauritsen, T. The observed hemispheric symmetry in reflected shortwave irradiance. *J. Climate* **26,** 468–477 (2013).

58. Klinger, B. A. & Marotzke, J. Meridional heat transport by the subtropical cell. *J. Phys. Oceanogr.* **30,** 696–705 (2000).

59. Held, I. M. The partitioning of the poleward energy transport between the tropical ocean and atmosphere. *J. Atmos. Sci.* **58,** 943–948 (2001).

60. Friedman, A. R., Hwang, Y.-T., Chiang, J. C. & Frierson, D. M. W. Interhemispheric temperature asymmetry over the 20th century and in future projections. *J. Climate* **26,** 5419–5433 (2013).

61. Sachs, J. P. *et al.* Southward movement of the Pacific Intertropical Convergence Zone AD 1400–1850. *Nat. Geosci.* **2,** 519–525 (2009).

62. Walker, C. C. & Schneider, T. Eddy influences on Hadley circulations: Simulations with an idealized GCM. *J. Atmos. Sci.* **63,** 3333–3350 (2006).

63. Schneider, T. The general circulation of the atmosphere. *Annu. Rev. Earth Planet. Sci.* **34,** 655–688 (2006).

64. Zhang, C. Double ITCZs. *J. Geophys. Res-Atmos. (1984–2012)* **106,** 11785–11792 (2001).

65. Xie, R. & Yang, Y. Revisiting the latitude fluctuations of the eastern Pacific ITCZ during the central Pacific El Niño. *Geophys. Res. Lett.* **41,** 7770–7776 (2014).

66. Hwang, Y.-T. & Frierson, D. M. W. Link between the double-Intertropical Convergence Zone problem and cloud biases over the Southern Ocean. *Proc. Natl. Acad. Sci.* **110,** 4935–4940 (2013).

67. Bischoff, T. & Schneider, T. Energetic constraints on the position of the intertropical convergence zone. *J. Climate* **27.** doi:10.1175/JCLI-D-13-00650.1 (2014).

68. Liu, Z., Ostrenga, D., Teng, W. & Kempler, S. Tropical Rainfall Measuring Mission (TRMM) Precipitation Data and Services for Research and Applications. *Bull. Amer. Meteor. Soc.* **93,** 1317–1325 (2012).

69. Merlis, T. M., Schneider, T., Bordoni, S. & Eisenman, I. Hadley circulation response to orbital precession. Part I: Aquaplanets. *J. Climate* **26,** 740–753 (2013).

70. Trenberth, K. E. & Caron, J. M. Estimates of meridional atmosphere and ocean heat transports. *J. Climate* **14,** 3433–3443 (2001).

71. Trenberth, K. E. & Fasullo, J. T. An observational estimate of inferred ocean energy divergence. *J. Phys. Oceanogr.* **38,** 984–999 (2008).

72. Marshall, J., Donohoe, A., Ferreira, D. & McGee, D. The ocean's role in setting the mean position of the Inter-Tropical Convergence Zone. *Clim. Dyn.* **42,** 1967–1979 (2014).

73. Peixoto, J. P. & Oort, A. H. *Physics of Climate* 1st ed. (American Institute of Physics, 1992).

74. Trenberth, K. E. & Stepaniak, D. P. Covariability of Components of Poleward Atmospheric Energy Transports on Seasonal and Interannual Timescales. *J. Climate* **16,** 3691–3705 (2003).

75. Schneider, T., Smith, K. L., O'Gorman, P. A. & Walker, C. C. A Climatology of Tropospheric Zonal-Mean Water Vapor Fields and Fluxes in Isentropic Coordinates. *J. Climate* **19,** 5918–5933 (2006).

76. Raymond, D. J., Sessions, S., Sobel, A. H. & Fuchs, Z. The mechanics of gross moist stability. *J. Adv. Model. Earth Sys.* **1,** Art. #9 (2009).

77. Privé, N. C. & Plumb, R. A. Monsoon dynamics with interactive forcing. Part I: Axisymmetric studies. *J. Atmos. Sci.* **64,** 1417–1430 (2007).

78. Emanuel, K. A. On Thermally Direct Circulations in Moist Atmospheres. *J. Atmos. Sci.* **52,** 1529–1534 (1995).

79. Sobel, A. H. in *The Global Circulation of the Atmosphere* (eds Schneider, T. & Sobel, A. H.) 219–251 (Princeton University Press, Princeton, NJ, 2007).

80. Stephens, G. L. *et al.* The albedo of Earth. *Rev. Geophys.* **53,** 141–163 (2015).

81. Lindzen, R. S. & Hou, A. Y. Hadley Circulations for Zonally Averaged Heating Centered off the Equator. *J. Atmos. Sci.* **45,** 2416–2427 (1988).

82. Harrison, E. F. *et al.* Seasonal Variation of Cloud Radiative Forcing Derived from the Earth Radiation Budget Experiment. *J. Geophys. Res.* **95,** 18687–18703 (1990).

83. Loeb, N. G. *et al.* Toward optimal closure of the Earth's top-of-atmosphere radiation budget. *J. Climate* **22,** 748–766 (2009).

84. Folland, C. K., Palmer, T. N. & Parker, D. E. Sahel rainfall and worldwide sea temperatures, 1901–85. *Nature* **320,** 602–607 (1986).

85. Rotstayn, L. D. & Lohmann, U. Tropical Rainfall Trends and the Indirect Aerosol Effect. *J. Climate* **15,** 2103–2116 (2002).

86. Giannini, A., Saravanan, R. & Chang, P. Oceanic Forcing of Sahel Rainfall on Interannual to Interdecadal Time Scales. *Science* **302,** 1027–1030 (2003).

87. Held, I. M., Delworth, T. L., Lu, J., Findell, K. L. & Knutson, T. R. Simulation of Sahel drought in the 20th and 21st centuries. *Proc. Natl. Acad. Sci.* **102,** 17891–17896 (2005).

88. McGee, D., Donohoe, A., Marshall, J. & Ferreira, D. Changes in ITCZ location and cross-equatorial heat transport at the Last Glacial Maximum, Heinrich Stadial 1, and the mid-Holocene. *Earth Planet. Sci. Lett.* **390,** 69–79 (2014).

89. Cai, W. *et al.* More extreme swings of the South Pacific convergence zone due to greenhouse warming. *Nature* **488,** 365–369 (2012).

90. Borlace, S., Santoso, A., Cai, W. & Collins, M. Extreme swings of the South Pacific Convergence Zone and the different types of El Niño events. *J. Geophys. Res.* **41,** 4695–4703 (2014).

91. Zhang, G. J. & Wang, H. Toward mitigating the double ITCZ problem in NCAR CCSM3. *Geophys. Res. Lett.* **33,** L06709 (2006).

92. Voigt, A. & Shaw, T. A. Circulation response to warming shaped by radiative changes of clouds and water vapour. *Nature Geosci.* **8,** 102–106 (2015).

93. Ashfaq, M., Skinner, C. B. & Diffenbaugh, N. S. Influence of SST biases on future climate change projections. *Climate Dyn.* **36,** 1303–1319 (2010).

94. Vannière, B., Guilyardi, E., Toniazzo, T., Madec, G. & Woolnough, S. A systematic approach to identify the sources of tropical SST errors in coupled models using the adjustment of initialized experiments. *Climate Dyn.* **43,** 2261–2282 (2014).

95. Chou, C. & Neelin, J. D. Mechanisms limiting the southward extent of the South American summer monsoon. *Geophys. Res. Lett.* **28,** 2433–2436 (2001).

96. Chou, C. & Neelin, J. D. Mechanisms limiting the northward extent of the northern summer monsoons over North America, Asia, and Africa. *J. Climate* **16,** 406–425 (2003).

97. Sobel, A. H. & Neelin, J. D. The boundary layer contribution to Intertropical Convergence Zones in the quasi-equilibrium tropical circulation model framework. *Theor. Comput. Fluid Dyn.* **20,** 323–350 (2006).

98. Neelin, J. D. in *The Global Circulation of the Atmosphere* (eds Schneider, T. & Sobel, A. H.) 267–301 (Princeton University Press, Princeton, NJ, 2007).

99. Schneider, T. & Bordoni, S. Eddy-mediated regime transitions in the seasonal cycle of a Hadley circulation and implications for monsoon dynamics. *J. Atmos. Sci.* **65,** 915–934 (2008).

100. Bordoni, S. & Schneider, T. Monsoons as eddy-mediated regime transitions of the tropical overturning circulation. *Nat. Geosc.* **1,** 515–519 (2008).

101. Lindzen, R. S. & Nigam, S. On the role of sea surface temperature gradients in forcing low-level winds and convergence in the tropics. *J. Atmos. Sci.* **44,** 2418–2436 (1987).

102. Waliser, D. E. & Somerville, R. C. J. Preferred Latitudes of the Intertropical Convergence Zone. *J. Atmos. Sci.* **51,** 1619–1639 (1994).

103. Hill, S. A., Ming, Y. & Held, I. M. Mechanisms of forced tropical meridional energy flux change. *J. Climate* **28,** 1725–1742 (2015).

104. Clement, A. C., Hall, A. & Broccoli, A. J. The importance of precessional signals in the tropical climate. *Clim. Dyn.* **22,** 327–341 (2004).

105. Hsu, Y.-H., Chou, C. & Wei, K.-Y. Land–ocean asymmetry of tropical precipitation changes in the mid-Holocene. *J. Climate* **23,** 4133–4151 (2010).

106. Kutzbach, J. E. Monsoon climate of the early Holocene: climate experiment with the earth's orbital parameters for 9000 years ago. *Science* **214,** 59–61 (1981).

107. Kutzbach, J. E. & Guetter, P. J. The influence of changing orbital parameters and surface boundary conditions on climate simulations for the past 18000 years. *J. Atmos. Sci.* **43,** 1726–1759 (1986).

108. Joussaume, S. *et al.* Monsoon changes for 6000 years ago: results of 18 simulations from the Paleoclimate Modeling Intercomparison Project (PMIP). *Geophys. Res. Lett.* **26,** 859–862 (1999).

109. Kutzbach, J., Liu, X., Liu, Z. & Chen, G. Simulation of the evolutionary response of global summer monsoons to orbital forcing over the past 280,000 years. *Clim. Dynam.* **30,** 567–579 (2008).

110. Khon, V., Park, W., Latif, M., Mokhov, I. & Schneider, B. Response of the hydrological cycle to orbital and greenhouse gas forcing. *Geophys. Res. Lett.* **37** (2010).

111. Pausata, F. S. R., Battisti, D. S., Nisancioglu, K. H. & Bitz, C. M. Chinese stalagmite δ^{18}O controlled by changes in the Indian monsoon during a simulated Heinrich event. *Nature Geosci.* **4,** 474–480 (2011).

112. Tigchelaar, M. & Timmermann, A. Mechanisms rectifying the annual mean response of tropical Atlantic rainfall to precessional forcing. *Climate Dyn.* (2015).

113. Cheng, H. *et al.* Ice age terminations. *Science* **326,** 248–252 (2009).

114. Byrne, M. P. & Schneider, T. Energetic Constraints on the Width of the Intertropical Convergence Zone. *J. Climate* **29,** 4709–4721 (2016).

115. Bischoff, T. & Schneider, T. The equatorial energy balance, ITCZ position, and double ITCZ bifurcations. *J. Climate* **29.** doi:10.1175/JCLI-D-15-0328.1 (2016).

116. Boer, G. Climate change and the regulation of the surface moisture and energy budgets. *Clim. Dynam.* **8,** 225–239 (1993).

117. Held, I. M. & Soden, B. J. Water vapor feedback and global warming 1. *Annu. Rev. Energ. Env.* **25,** 441–475 (2000).

118. Huybers, P. & Denton, G. Antarctic temperature at orbital timescales controlled by local summer duration. *Nature Geosc.* **1,** 787–792 (2008).

119. Sobel, A. H., Nilsson, J. & Polvani, L. M. The weak temperature gradient approximation and balanced tropical moisture waves*. *J. Atmos. Sci.* **58,** 3650–3665 (2001).

120. Marshall, J., Donohoe, A., Ferreira, D. & McGee, D. The ocean's role in setting the mean position of the Inter-Tropical Convergence Zone. *Clim. Dynam.* **42,** 1967–1979 (2014).

121. Liu, J. & Schneider, T. Contrasting responses to orbital precession on Titan and Earth. *Geophys. Res. Lett.* **43.** doi:10.1002/2016GL070065 (2016).

122. Lomb, N. R. Least-squares frequency analysis of unequally spaced data. *Astrophys. Space Sci.* **39,** 447–462 (1976).

123. Scargle, J. D. Studies in astronomical time series analysis. II-Statistical aspects of spectral analysis of unevenly spaced data. *Astrophys. J.* **263,** 835–853 (1982).

124. Huybers, P. & Eisenman, I. *Integrated Summer Insolation Calculations* (NOAA/NCDC Paleoclimatology Program, Boulder CO, USA., 2006).

125. Berger, A. Long-term variations of daily insolation and Quaternary climatic changes. *J. Atmos. Sci.* **35,** 2362–2367 (1978).

126. Berger, A. & Loutre, M.-F. Insolation values for the climate of the last 10 million years. *Quaternary Sci. Rev.* **10,** 297–317 (1991).

127. Meckler, A., Clarkson, M., Cobb, K., Sodemann, H. & Adkins, J. Interglacial hydroclimate in the tropical West Pacific through the Late Pleistocene. *Science* **336,** 1301–1304 (2012).

128. Meckler, A. *et al.* Deglacial pulses of deep-ocean silicate into the subtropical North Atlantic Ocean. *Nature* **495,** 495–498 (2013).

129. Liu, Z. *et al.* Chinese cave records and the East Asia summer monsoon. *Quaternary Sci. Rev.* **83,** 115–128 (2014).

130. Lisiecki, L. E. & Raymo, M. E. A Pliocene-Pleistocene stack of 57 globally distributed benthic δ18O records. *Paleoceanography* **20** (2005).

131. Horne, J. H. & Baliunas, S. L. A prescription for period analysis of unevenly sampled time series. *Astrophys. J.* **302,** 757–763 (1986).

132. Press, W. H. & Rybicki, G. B. Fast algorithm for spectral analysis of unevenly sampled data. *Astrophys. J.* **338,** 277–280 (1989).

133. Politis, D. N. & Romano, J. P. The stationary bootstrap. *J. Am. Stat. Assoc.* **89,** 1303–1313 (1994).

134. Politis, D. N. & White, H. Automatic block-length selection for the dependent bootstrap. *Economet. Rev.* **23,** 53–70 (2004).

135. Moore, C. & Mertens, S. *The nature of computation* (OUP Oxford, 2011).

136. Le Traon, P. Y. & Morrow, R. in (eds Fu, L. L. & Cazenave, A.) 171–210 (Academic Press; 1st edition, 2001).

137. Ferrari, R. & Nikurashin, M. Suppression of eddy diffusivity across Jets in the Southern Ocean. *J. Phys. Oceanogr.* **40,** 1501–1519 (2010).

138. Hughes, C. Nonlinear vorticity balance of the Antarctic Circumpolar Current. *J. of Geophys. Res.: Oceans* **110,** C11008 (2005).

139. Williams, R., Wilson, C. & Hughes, C. Ocean and atmosphere storm tracks: The role of eddy vorticity forcing. *J. Phys. Oceanogr.* **37,** 2267–2289 (2007).

140. Thompson, A. F. & Naveira Garabato, A. C. Equilibration of the Antarctic Circumpolar Current by standing meanders. *J. Phys. Oceanogr.* **44,** 1811–1828 (2014).

141. Hoskins, B. & Valdes, P. On the existence of storm-tracks. *J. Atmos. Sci.* **47,** 1854–1864 (1990).

142. Chang, E. K. & Orlanski, I. On the dynamics of a storm track. *J. Atmos. Sci.* **50,** 999–1015 (1993).

143. Kaspi, Y. & Schneider, T. Downstream self-destruction of storm tracks. *J. Atmos. Sci.* **68,** 2459–2464 (2011).

144. Kaspi, Y. & Schneider, T. Winter cold of eastern continental boundaries induced by warm ocean waters. *Nature* **471,** 621–624 (2011).

145. Lee, S. Localized storm tracks in the absence of local instability. *J. Atmos. Sci.* **52,** 977–989 (1995).

146. Swanson, K. L., Kushner, P. J. & Held, I. M. Dynamics of barotropic storm tracks. *J. Atmos. Sci.* **54,** 791–810 (1997).

147. Marshall, J. & Radko, T. A model of the upper branch of the meridional overturning of the Southern Ocean. *Prog. Oceanogr.* **70,** 331–345 (2006).

148. Naveira Garabato, A. C., Ferrari, R. & Polzin, K. L. Eddy stirring in the Southern Ocean. *J. Geophys. Res.: Oceans* **116,** 1978–2012 (2011).

149. Thompson, A. F. & Sallée, J. B. Jets and topography: Jet transitions and the impact on transport in the Antarctic Circumpolar Current. *J. Phys. Oceanogr.* **42,** 956–972 (2012).

150. Thompson, A. F., Haynes, P., Wilson, C. & Richards, K. Rapid Southern Ocean front transitions in an eddy-resolving ocean GCM. *Geophys. Res. Lett.* **37,** L23602 (2010).

151. MacCready, P. & Rhines, P. B. Meridional transport across a zonal channel: Topographic localization. *J. Phys. Oceanogr.* **31,** 1427–1439 (2001).

152. Naveira Garabato, A., Stevens, D., Watson, A. & W, R. Short-circuiting of the overturning circulation in the Antarctic Circumpolar Current. *Nature* **447,** 194–197 (2007).

153. Hallberg, R. & Gnanadesikan, A. An exploration of the role of transient eddies in determining the transport of a zonally reentrant current. *J. Phys. Oceanogr.* **31,** 3312–3330 (2001).

154. Tansley, C. E. & Marshall, D. P. On the dynamics of wind-driven circumpolar currents. *J. Phys. Oceanogr.* **31,** 3258–3273 (2001).

155. Marshall, J., Adcroft, A., Hill, C., Perelman, L. & Heisey, C. A finite-volume, incompressible Navier Stokes model for studies of the ocean on parallel computers. *J. Geophys. Res.* **102,** 5753–5766 (1997).

156. Abernathey, R., Marshall, J. & Ferreira, D. The dependence of Southern Ocean meridional overturning on wind stress. *J. Phys. Oceanogr.* **41,** 2261–2278 (2011).

157. Hughes, C. W. & Ash, E. R. Eddy forcing of the mean flow in the Southern Ocean. *J. Geophys. Res.: Oceans* **106,** 1978–2012 (2001).

158. Sokolov, S. & Rintoul, S. R. Circumpolar structure and distribution of the Antarctic Circumpolar Current fronts: 1. Mean circumpolar paths. *J. Geophys. Res.: Oceans* **114,** 1978–2012 (2009).

159. Thompson, D. W. & Solomon, S. Interpretation of recent southern hemisphere climate change. *Science* **296,** 859–899 (2002).

160. Pierrehumbert, R. Local and global baroclinic instability of zonally varying flow. *J. Atmos. Sci.* **41,** 2141–2162 (1984).

161. Cai, M., Yang, S., Van den Dool, H. & Kousky, V. Dynamical implications of the orientation of atmospheric eddies: a local energetics perspective. *Tellus A* **59,** 127–140 (2007).

162. Lindzen, R. S. & Farrell, B. A simple approximate result for the maximum growth rate of baroclinic instabilities. *J. Atmos. Sci.* **37,** 1648–1654 (1980).

163. Hogg, A. M., Meredith, M. P., Blundell, J. R. & Wilson, C. Eddy heat flux in the Southern Ocean: Response to variable wind forcing. *J. Climate* **21,** 608–620 (2008).

164. Tréguier, A.-M. *et al.* Southern Ocean overturning across streamlines in an eddying simulation of the Antarctic Circumpolar Current. *Ocean Sci. Discuss.* **4,** 653–698 (2007).